Investigating the effect of the Dynamic Response of Lattice Structures on Wind Loads using Computational Fluid Dynamics and Wind Tunnel Testing

By

YOMNA GOBRAN

Department of Civil Engineering and Applied Mechanics

McGill University

Montreal, Quebec, Canada

November 2024

A thesis submitted to McGill University in partial fulfillment of the requirements of the degree of Doctor of Philosophy

TABLE OF CONTENTS

ABSTRACT

This study investigates the effect of the flexibility of structural members and lattice structures on wind loading through Computational Fluid Dynamics (CFD) simulations and wind tunnel experiments. In order to carry out such an investigation, it was required to evaluate Wind Structure Interaction (i.e., WSI) forces, which was done through determining the Aerodynamic Derivatives (i.e., AD) of the structural bodies under investigation. First, the applicability of using CFD simulations to evaluate the AD from the response of free vibrating bluff bodies was examined, by studying three-dimensional simulations of a rigid cylinder with a square cross-section that is elastically supported and constrained to move only in one (the transverse) direction under wind loading. Primarily, to validate the method, the square cylinder was tested in a stationary state and the force coefficients were calculated at different wind angles of attack. Following that, to determine the ADs, the free vibrations method was used, where the rigid square cylinder was first pushed a fixed distance and then left to freely vibrate. The total damping ratio was calculated from the measured displacement time history and hence the AD. It was concluded that the approach used is valid for sharp-edged bluff bodies and could be used in the future to estimate the flutter derivatives.

Secondly, wind tunnel experiments were done to determine ADs for three models that are elements/parts of lattice structures: a cylinder with square cross-sections, a cylinder with equal-leg angled cross-sections, and a lattice structure. The models were rigid and supported on springs allowing the motion in the transverse direction only. The springs were connected to load cells to measure the fluid structure interaction forces from where the displacements and subsequently, the total damping and hence the AD (H_1^*) were calculated at each velocity tested. The results provide the AD (H_1^*) for models that were not studied before in the literature (angle shape and 4-panel W truss). The aerodynamic derivative is then used to determine the wind loads acting on the structures taking the fluid-structure interaction into consideration.

Thirdly, to assess whether taking the structural flexibility into account would affect the wind loading and structural response or not, a dynamic numerical analysis was performed, and the responses with and without the effect of aerodynamic damping were compared. This was first done for the square cylinder, modelling it as a single-degree-of-freedom system. It was shown that the forces are amplified at vortex-induced vibrations range of velocities and at high velocities as well, while there was only minor effect over the other velocities tested. Then, a structural dynamics model for a lattice structure composed of the studied W-truss model was created, where an equivalent overall aerodynamic damping was calculated for the whole structure for different mode shapes with the knowledge of the aerodynamic derivative of structural parts of the whole structure. The findings highlight the significance of accounting for structural flexibility when assessing wind loads, as the interaction between the fluid and structure noticeably impacts the loads. Specifically, the square cylinder exhibited an amplification effect on the response, whereas the lattice structure showed a significant reduction.

RÉSUMÉ

Cette étude examine l'effet de la flexibilité des éléments structuraux et des structures en treillis sur la charge éolienne à l'aide de simulations de dynamique des fluides numérique (CFD) et d'expériences en soufflerie. Pour mener une telle investigation, il a été nécessaire d'évaluer les forces d'interaction entre le vent et la structure (Wind Structure Interaction - WSI), ce qui a été réalisé en déterminant les dérivées aérodynamiques (Aerodynamic Derivatives - AD) des éléments structuraux étudiés. Tout d'abord, l'applicabilité de l'utilisation de simulations CFD pour évaluer les AD à partir de la réponse de corps rigides en vibration libre a été examinée, en étudiant des simulations tridimensionnelles d'un cylindre rigide de section carrée, élastiquement soutenu et contraint de se déplacer uniquement dans une direction transversale sous l'effet du vent. Pour valider la méthode, le cylindre carré a été testé dans un état stationnaire, et les coefficients de forces ont été calculés pour différentes incidences du vent. Ensuite, pour déterminer les AD, la méthode des vibrations libres a été utilisée, où le cylindre carré rigide a d'abord été poussé sur une distance fixe, puis laissé vibrer librement. Le rapport total d'amortissement a été calculé à partir de l'historique des déplacements mesurés, et donc l'AD a été déterminé. Enfin, il a été conclu que l'approche utilisée est valable pour les corps rigides à arêtes vives et pourrait être utilisée à l'avenir pour estimer les dérivées d'instabilité aéroélastique.

Ensuite, des expériences en soufflerie ont été réalisées pour déterminer les AD pour trois modèles qui sont des éléments/parties de structures en treillis: un cylindre à section carrée, un cylindre à section d'angles égaux (cornière à ailes égales) et une structure en treillis. Les modèles étaient considérés rigides et soutenus sur ressorts élastiques, permettant le mouvement dans la direction transversale uniquement. Les ressorts étaient connectés à des cellules de charge pour mesurer les forces d'interaction fluide-structure, à partir desquelles les déplacements et, par conséquent, l'amortissement total et donc l'AD (H_1^*) ont été calculés à

chaque vitesse de vent testée. Les résultats fournissent les AD (H_1^*) pour des modèles qui n'avaient pas été étudiés auparavant dans la littérature (angle et treillis W à 4 panneaux). La dérivée aérodynamique est ensuite utilisée pour déterminer les charges éoliennes agissant sur les structures en tenant compte de l'interaction fluide-structure.

Troisièmement, pour évaluer si la prise en compte de la flexibilité structurale affecterait ou non la charge éolienne et la réponse structurelle, une analyse numérique dynamique a été effectuée, comparant la réponse avec et sans l'effet de l'amortissement aérodynamique. Cette analyse a d'abord été réalisée pour le cylindre carré en le modélisant comme un système à un degré de liberté. Il a été démontré que les forces sont augmentées dans la plage des vitesses de vibrations induites par les vortex et à des vitesses élevées également, tandis qu'il y a peu de changement aux autres vitesses testées. Ensuite, un modèle d'analyse dynamique pour une structure en treillis composée du modèle de treillis étudié a été créé, où un amortissement aérodynamique global équivalent a été calculé pour l'ensemble de la structure pour différents modes naturels en utilisant la dérivée aérodynamique des parties structurales de l'ensemble de la structure. Les résultats montrent que la prise en compte de la flexibilité de la structure lors de la détermination des charges éoliennes est importante car l'interaction fluide-structure a un effet notable sur les charges. Plus précisément, le cylindre carré a montré un effet d'amplification sur la réponse, tandis que la structure en treillis a montré une réduction de son impact.

ACKNOWLEDGEMENT

I would like to express my deepest appreciation to Professor Ghyslaine McClure and Associate Professor Haitham Aboshosha for their support, guidance, motivation, and confidence in me. Also special thanks to them for their support during the experimental portion of my thesis. It has been a privilege working under their supervision.

I could not have undertaken this journey without the financial support of the Natural Sciences and Engineering Research Council of Canada. I would also like to acknowledge Toronto Metropolitan University for allowing us to use their wind tunnel facility to conduct the experimental aspect of this research.

I also had the pleasure of working with Tarek Ghazal and Daniel Gemayel, special thanks to them for helping me during the wind tunnel testing.

Last, but not least, I would like to express my deepest gratitude to my father Atef and my mother Gehan for their constant support. I am extremely grateful to my Husband Khairy for his support, encouragement and understanding, without which I would not have been able to complete my Ph.D.

CONTRIBUTIONS TO ORIGINAL KNOWLEDGE

The original scholarship and distinct contributions of this thesis are:

1. Adapted methodology used for streamlined bodies (i.e., bridges) to flexible bluff bodies (i.e., square cylinder and lattice structure). The methodology was used to study the effect of aeroelasticity of exposed structures and applied to a square cylinder and a lattice structure on flexible supports.

2. Carried out free vibration tests in the wind tunnel which proved to be a reliable tool in the derivation of the aerodynamic derivative H_1^* for the single-degree-of-freedom strongly bluff bodies and system tested.

3. Conducted wind tunnel free vibration tests to determine the aerodynamic derivative H_1^* for equal-leg angle section at two angles of attack 45^o and 135^o.

4. Conducted wind tunnel free vibration tests to determine the aerodynamic derivative H_1^* for a four-panel W-truss for two different solidity ratios. Built a library for H_1^* derivative for the W-shaped truss. This will facilitate the initial design for the W-shaped truss by estimating the response using the H_1^* derivative.

5. Proved the reliability of using numerical 3D Large Eddy Simulations (LES) turbulent models to estimate the aerodynamic derivatives for single-degree-of-freedom bluff bodies.

CONTRIBUTIONS OF AUTHORS

In accordance with the "Guidelines for Thesis Preparation", this thesis is presented in a manuscript-based format. Authorships of the three articles are explained below.

Chapter 3

Yomna Gobran, Ghyslaine McClure and Haitham Aboshosha. Determination of aerodynamic derivative for one degree of freedom square cylinder using large eddy simulation. Published in Results in Engineering Journal in December 2022 [1].

- Literature research, Numerical study as well as writing of the manuscript were conducted by Yomna Gobran.
- Ghyslaine McClure and Haitham Aboshosha provided supervision of the research and editing of the manuscript.

Chapter 4

Yomna Gobran, Ghyslaine McClure, Haitham Aboshosha and Tarek Ghazal. Determining aerodynamic derivatives for members of lattice structures through wind tunnel testing. Prepared for submission.

- Literature research, Experiment design, analysis of the results as well as writing of the manuscript were conducted by Yomna Gobran.
- Tarek Ghazal helped with the Experimental work and editing of the manuscript.
- Ghyslaine McClure and Haitham Aboshosha provided supervision of the research, assistance for the experimental work and editing of the manuscript.

Chapter 5

Yomna Gobran, Ghyslaine McClure and Haitham Aboshosha. Exploring wind-structure interactions on flexibly supported truss members and lattice panels using wind tunnel experiments. Prepared for submission.

- Literature research, Dynamic analysis as well as writing of the manuscript were conducted by Yomna Gobran.
- Ghyslaine McClure and Haitham Aboshosha provided supervision of the research and editing of the manuscript.

LIST OF FIGURES

LIST OF TABLES

CHAPTER 1 INTRODUCTION

1.1 Research Problem and Motivation

Slender exposed structures such as signage cantilevered structures, lighting poles, telecommunications structures, to name a few, can undergo significant motions under wind loads, which may jeopardize their fatigue life and structural integrity or make them unserviceable or unsafe. The vibrations are mostly due to separation and reattachment of the unsteady boundary layer. These motions can be along-wind translations, resulting from the direct effect of wind velocity pressures, across-wind translations resulting from vortex-shedding effects, and in torsional direction resulting from strong separated flows around more bluff sections subjecting it to single-degree-of-freedom torsional instability named torsional flutter [2]. The coupling between these three motions depends on the aeroelastic interaction with the structure and the natural frequency of the structure in the three corresponding directions, and as frequencies come closer to each other, the likelihood of such dynamic interactions get higher.

Consequently, flexible structures exposed to wind will experience different aerodynamic forces than rigid structures of comparable cross-sectional properties. In practice, some exposed flexible structures under wind action may undergo important vibrations, which can lead to boosting or diminishing the aerodynamic forces acting on them. This happens because as the structure moves, an extra damping is generated which is the aerodynamic damping. When the aerodynamic damping is negative motion is amplified and when it exceeds the structural damping the structure becomes unstable. Consequently, relatively slender structures and exposed structures may be vulnerable to the effects of winds in ways that are difficult to predict using standard structural analysis procedures. In this research we want to investigate the effect of flexibility of exposed slender structures on wind loads, that is whether this flexibility could

lead to boosting or diminishing the aerodynamic forces acting on them, in comparison with the rigid assumption. The study is pertained to strongly bluff bodies that have sharp edges, where the flow separates at the front (windward) edges and does not reattach along the sides. This is in contrast with the moderately bluff bodies where the flow reattaches again over the body width, and the streamlined structures where the flow stays adjacent to the body without separation.

The aerodynamic response of exposed structural members depends on their cross-sectional shape, aspect ratio (if not circular or with a complex shape), wind direction and wind velocity profile. For example rectangular cylinders of width over depth ratio, b/d of about 2.5 to 5.5 typically exhibit soft torsional flutter (i.e. they easily go into instability without initial disruption) as indicated by Washizu et al. [3]. While for b/d < 2.5, rectangular cylinders are less prone to flutter instabilities than less bluff shapes [4]. Square sections (b/d=1) normally are not prone to flutter instability but can experience one-dimensional instability such as galloping at high reduced wind speeds U_{red} = V/F_nB, where V is the mean wind velocity, F_n is the structure natural frequency and B is the along-wind dimension of the cross section. Since the reduced wind speed is a function of the structure's natural frequency and considering two structures with the same cross section and mass but different frequencies, the one with lower frequency (more flexible) will experience a larger reduced wind speed than the one with higher frequency (stiffer). However, the value of U_{red} on its own is insufficient to predict the vibrational response of exposed structures particularly in instances when instability may occur and when there is a possibility of wind-structure interaction involving relatively large motions in comparison to the structure dimensions.

There are different methods to assess the wind-induced response of flexible structures [5]. One of the methods to evaluate the motion-induced forces on flexible structures is to identify their aerodynamic derivatives. The aerodynamic derivatives are determined through forced or free

vibration wind tunnel tests or numerical simulations, by finding the aerodynamic damping from the vibrations time history, with the knowledge of mass, stiffness and structural damping. Following that, for a certain structure with the knowledge of its mass, stiffness, and measured vibrations one can determine the motion-induced forces from equations developed by Scanlan et al. 1971 [6].

The main query is intended to determine whether wind-structure interactions with flexible exposed structures may have a significant influence on the forces/responses. Therefore, first the AD H_1^* for a square, equal-legged angle cross-section cylinder and a four-truss panel were determined. Secondly, a CFD simulation was done for all the structural models, to find the aerodynamic forces. At last, a finite element model of a whole structure comprised of the tested structural models was created. Dynamic analysis was performed using aerodynamic forces from CFD simulations. Simulations were repeated twice, once using the structural damping only and another time adding the aerodynamic damping to the structural damping. Comparison of forces and response of the structural model from both cases showed that for the square cylinder the response was amplified on the contrary it was decreased in the case of the lattice structure.

1.2 Methodology

In this study the determination of wind forces on vibrating bodies was done through Fluid Structure Interaction (FSI) simulations and wind tunnel experiments. Since three-dimensional FSI simulations are computationally expensive for bodies of complex geometry such as truss panels, wind tunnel tests were used to determine the aerodynamic damping for vibrating bodies, while CFD simulations were used to determine aerodynamic forces on stationary bodies. Following that ADs were determined. Eventually the aerodynamic forces along with the ADs

were used to find the structural response and forces acting on the body due to wind load through finite element dynamic analysis.

The work presented here is applicable to aerodynamic single-degree-of-freedom (SDOF) systems in the transverse direction (cross-stream). This assumption, adopted to simplify numerical treatment, is deemed valid since the structures under investigation are symmetric and therefore their oscillations occur in non-coupled modes and mostly in flexure [7]. Additionally, in a study on the isolated angle shape it was found that the amplitude and frequency results from transverse-torsional vibrations are comparable to SDOF measurements [8].

The use of AD has been efficient and valuable in numerous bridge design studies. In the current study we will identify the aerodynamic derivatives (ADs) for different structural cross sections (i.e., at the member level) that are rarely covered in the open literature (square) or have not been studied and reported before (angle shape). The research will establish whether these ADs can help in determining the aero-elastic forces/response on structures (such as three-dimensional truss panels) made of bluff elements. There are two main experimental approaches to determine the AD on a given body, namely the free and forced vibrations tests. In the forced vibration approach, the motion of the body is prescribed, and ADs are extracted from the recorded wind forces acting on the body. On the other hand, in the free vibration approach, the body is supported on springs where it is given a push then released to vibrate freely under the incoming wind condition, and then aerodynamic derivatives are extracted from the recorded body motion.

Gao et al. 2016 found that the peak forces obtained in the forced vibration test were significantly lower than those obtained in the free vibration test, although the displacement spectra obtained via the two tests were in reasonable agreement [9]. This suggests that the

forced vibration test tends to underestimate the aerodynamic force. As such, it is questionable whether forced vibration tests can reflect the inherent complexity of the wind-structure interactions for the bluff section, and therefore they may not be applicable to investigate the aeroelastic response of bluff bodies. Accordingly, the free vibrations technique will be employed here because it is deemed more adequate for the ensuing work.

1.3 Thesis Outline

A comprehensive review of past studies related to the change in aerodynamic forces due to wind load when considering the structure flexibility is presented in Chapter 2.

Chapter 3 focuses on investigating the applicability of using CFD simulations to evaluate the AD of a square cylinder (as a representative of strongly bluff bodies) using the free vibration method. It also discusses the choice of the parameters affecting the CFD simulation. Additionally, the importance of finding the aerodynamic derivative H_1^* with respect to instability is discussed, and the steps followed to find the AD. Moreover, it explores whether with the aid of the AD, the amplitude of vibration can be estimated for strongly bluff bodies.

Chapter 4 provides a description of the single-degree-of-freedom test setup used for the wind tunnel testing of three strongly bluff models: a cylinder with square cross-section, a cylinder with equal-leg angled cross-section, and a four-panel three-dimensional lattice structure. In addition, the chapter describes the testing procedures and equipment used, as well as the extraction of the aerodynamic derivative H_1^* from the time histories of the forces.

Chapter 5 summarizes the results of the experimental wind tunnel tests and focuses on the development and validation of the structural dynamic analysis of the finite element model of the three-dimensional truss panel. This case study is described in detail to demonstrate the proposed methodology to find the dynamic response of strongly bluff bodies exposed to wind taking their structural flexibility into account.

Chapter 6 is a comprehensive scholarly discussion of all findings. Chapter 7 provides a summary of the main findings of this research. The same chapter highlights some limitations of the research and provides suggestions for future work.

CHAPTER 2 LITERATURE REVIEW

2.1 Background and Scope

The excitation of a structure exposed to wind is affected by different mechanisms: buffeting by gusts, vortex shedding, galloping and flutter. Gusts are the fluctuations in the wind velocity and generate fluctuating forces on the structure forcing it to move in the wind direction. Flow around a sharp-edged bluff body is characterized by separation at the front corners, which creates a large wake (after body is the part of the body downstream the separation point) that increases the possibilities of buffeting, galloping and vortex-induced vibrations [10]. Figure 2-1 shows the possible vibration mechanisms with respect to the aspect ratio B/D of bluff bodies.

Vortex shedding is a well-known phenomenon that exists due to adverse pressure gradients and the separation of the wind flow from the structure. Vortex shedding exerts forces on the structure forcing it to vibrate in the crosswind direction (for the sharp-edged bodies under study). Such vibrations happen over a limited range of flow velocities containing the velocity at resonance, where the structure's natural frequency and the vortex shedding frequency coincide. The resulting vibration amplitudes are self-limiting. On the other hand, galloping is a self-excited vibration characterized by its high amplitude and low frequency vibrations. In general, it is considered to be an aerodynamic instability as the amplitude of the motion increases continuously when the flow velocity is above a critical value. One of the reasons galloping happens is when the incident flow is not aligned with the principal directions of the body, which leads to asymmetric vortex shedding where one shear layer lies closer to the section than the other. The near shear layer creates higher suction on the adjacent side than is occurring on the other side, and this difference in pressure creates the exciting force. When the destabilizing effect of the fluid force is larger than the stabilizing effect of structural damping,

a small displacement of the body perpendicular to the flow creates a fluid force in the direction of the motion that tends to increase the amplitude of vibration. Eventually this means if the shear layer attaches to the section before its trailing edge, it will no longer have an afterbody, and transverse galloping will not occur.

Classical flutter is a motion that relies on the coupling between two degrees of freedom, flexural and torsional modes [11]. Civil engineering structures commonly affected are suspension bridges and tall exposed non-circular towers and stacks where substantial bending and torsion occur.

This research focuses on analysing fluid-structure interactions in exposed flexible structures and determining how they translate into effective wind loads and whether these forces are affected by the structure flexibility. Many studies (e.g. [12], [13], [14]) have shown potential change in the wind forces acting on exposed members due to dynamic instability. The research combines computational fluid dynamic (CFD) and fluid structure interaction (FSI) simulations and wind tunnel experiments to characterize the dynamic behaviour at the member and the structure level.

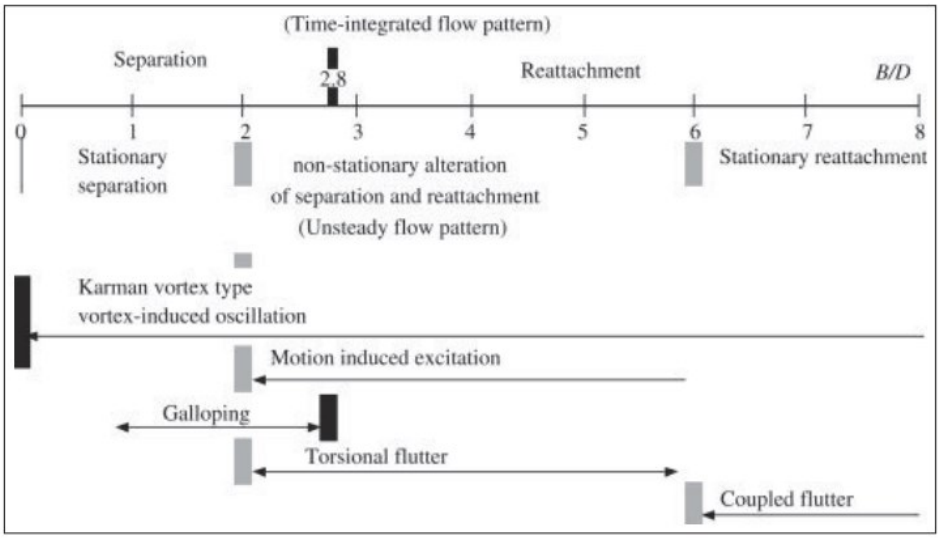

Figure 2-1 Sharp-edged bluff-bodies aerodynamic characteristics. [Takeuchi and Matsumoto 1992]

2.2 CFD as a Research Tool in Structural Engineering

Studying the wind flow around a bluff body requires first knowing the nature of the fluid dynamics. The flow in the atmospheric boundary layer is inherently turbulent. The flow-field around a bluff body is complicated and difficult to analyze since it is defined by impingement, separation, free shear layers, reattachment, circulation, vortices, etc. Therefore very fine grid discretization is required to analyze such flow fields with high accuracy in numerical simulations [15].

Computational Fluid Dynamics (CFD) is used in several engineering applications in environmental engineering, hydraulics and aeronautics, and the availability of advanced analysis software and high power computing platforms has made it even more accessible to study various wind engineering problems such as flow-fields around pedestrians in urban settings, dispersion around buildings, and in particular in structural engineering for the study of flow-fields around bluff bodies such as buildings, bridges, etc. CFD is a computational method where the fluid flow around a body is analysed using the fluid dynamics governing equations of mass, momentum and energy; the equation of state (temperature) is neglected here as the Mach number (ratio of flow velocity to speed of sound) is below 0.3 therefore the flow is incompressible.

CFD as a numerical simulation tool is an evolving field that often works best in complement with experiments, depending on the phenomena being studied. There are mutual benefits for the two approaches, especially in structural engineering applications: wind-tunnel testing can provide the indispensable high-quality validation data needed for CFD models, and CFD can supplement wind-tunnel testing by providing whole-flow field data for all relevant parameters and on all boundaries. Computational wind engineering (CWE), which is the application of CFD to wind flow over structures, can help to design and set up wind tunnel experiments and hence reduce the time required to optimize a physical model and expensive pre-attempts in a

wind tunnel. In addition, recent increase in high power computing has made it possible to use CFD in studying the aerodynamic behaviour of structures in the early stage of design [16].

CWE also allows full control over the boundary conditions of the model in addition to easily and efficiently allowing for parametric studies to evaluate alternative design configurations. Also, although on-site physical measurements can capture the complexity of the problem under study, such experiments are not fully controllable due to the inherently variable meteorological conditions, and they are not possible at the design stage. Another important advantage of CWE is that it can provide detailed information on the relevant flow variables in the whole calculation domain (whole-flow field data), under well-controlled conditions. On the contrary the on-site measurements and wind tunnel tests (WTTs) provide information at certain points only, so the detailed information determined by CWE has a valuable place in the preliminary design process. [17].

The accuracy and reliability of CWE simulations are of concern and solution verification and validation studies are imperative. This validation requires high-quality full-scale or reduced-scale measurements, which in turn should satisfy important quality criteria. Therefore, experiments remain indispensable for CWE [17]. It is also recognised that CWE results can be sensitive to the wide range of computational parameters that have to be set by the user. For a typical simulation, the user has to select the target variables, the computational domain, the turbulence model, the computational grid, the boundary conditions, the discretisation schemes and the convergence criteria. Parameter setting requires a good knowledge of basic fluid dynamics concepts and CFD best practice modelling guidelines [17].

The most important factors that affect the accuracy of CFD models will be discussed next. These factors include the turbulence model, the inflow boundary conditions and the numerical accuracy, mesh size, domain size, choice of discretization scheme, and step size.

2.2.1 Turbulence Models

Turbulence intensity (I) is the ratio of the R.M.S. average of the velocity fluctuations in the stream direction to the mean velocity. There are different types of turbulence models but the most commonly used and proved effective in simulating wind flows around bluff bodies is the large eddy simulation (LES) model. In LES, the three-dimensional (3D) time-dependent Navier-Stokes (N-S) equations are solved for the large-scale eddies while small-scale eddies are modelled using eddy viscosity models, as illustrated schematically in Figure 2-2. This approach eliminates the need for fine grid and small time step compared to direct numerical simulation, which solves the N-S equations on all scales [18]. LES becomes more advantageous and accurate for higher Re as the small-scale turbulent motion becomes smaller and harder to resolve (such a solution would not be currently feasible given the computational power available). Consequently, the small-scale motion is filtered out and only motions larger than the filter width, which is in general effectively the mesh size, are resolved. The unresolved small-scale fluctuations are simulated with a sub-grid scale model (SGS) [19]. There are many sub-grid scale models and four of them are offered in ANSYS fluent (the platform used in this research); the Smagorinsky-Lilly model, the dynamic Smagorinsky-Lilly model, the Wall-Adapting Local Eddy-Viscosity **(**WALE) model, and the dynamic kinetic energy subgrid-scale model. The Smagorinsky-Lilly model is the simple model first proposed by Smagorinsky [20], which requires assigning a value for the constant C_s (Smagorinsky constant) depending on the flow-field under investigation. This is considered a shortcoming since the flow field around sharp-edged bluff bodies includes several types of flow properties such as separation, vortex shedding, etc. which makes it hard to select a single suitable value for C_s [21]. This issue is overcome by the dynamic Smagorinsky-Lilly model, proposed by Germano [22] and modified by Lilly [23], where C_s is dynamically computed and varies in time and space. The concept of the dynamic procedure is to apply a second filter (called the test filter) to the equations of

motion. The new filter width $\hat{\Delta}$ is equal to twice the grid filter width Δ. Both filters produce a resolved flow field. The difference between the two resolved fields is the contribution of the small scales whose size is in between the grid filter and the test filter. The information related to these scales is used to compute the model constant [24]. The WALE model has a default value of the WALE constant, $C_w = 0.325$, and has been found to yield satisfactory results for a wide range of flows. In the Dynamic Kinetic Energy Subgrid-Scale Model, the subgrid-scale turbulence is modelled by accounting for the transport of the subgrid-scale turbulence kinetic energy where two model constants (C_k and C_ε) are determined dynamically [25]. In this study, the SGS model used is the dynamic Smagorinsky–Lilly model [26].

In the Smagorinsky–Lilly model, SGS σ_{ij}^s is modelled by:

$$\sigma_{ij}^s - \frac{1}{3}\delta_{ij}\sigma_{kk}^s = 2(C_s\Delta)^2|S|S_{ij} \qquad 2\text{-}1$$

where $|S| = \sqrt{2S_{ij}S_{ij}}$ and $S_{ij} = \frac{1}{2}(\frac{\partial \overline{v_\iota}}{\partial x_j} + \frac{\partial \overline{v_\jmath}}{\partial x_i})$ with $\overline{v_\iota}$ being the filtered flow velocity; C_S is Smagorinsky constant and Δ is the grid-filler length computed by $\Delta = V^{1/3}$ with V being the volume of the computational cell in FLUENT. In this study, C_S is calculated by the dynamic model suggested by Lilly [23]. The governing flow equations with LES representation of the turbulence (with added SGS viscosity) are:

$$\frac{\partial \overline{u_\iota}}{\partial x_i} = 0 \qquad 2\text{-}2$$

$$\frac{\partial \overline{u_\iota}}{\partial \mathrm{t}} + \left(\overline{u_\jmath}\right)\frac{\partial \overline{u_\iota}}{\partial x_j} = -\frac{1}{\rho}\frac{\partial \bar{P}}{\partial x_i} + \frac{\partial}{\partial x_j}\left(-\tau_{ij} + 2\nu\overline{S_{\iota\jmath}}\right) + f_i \qquad 2\text{-}3$$

$$\tau_{ij} = \overline{u_\iota u_\jmath} - \overline{u_\iota}\,\overline{u_\jmath} \qquad 2\text{-}4$$

$$\overline{S_{ij}} = \frac{1}{2}\left(\frac{\partial \overline{u_i}}{\partial x_j} + \frac{\partial \overline{u_j}}{\partial x_i}\right) \quad 2\text{-}5$$

$$\tau_{ij} - \frac{1}{3}\delta_{ij}\tau_{kk} = 2\nu_e\overline{S_{ij}} \quad 2\text{-}6$$

$$\nu_e = (C_s.\Delta)^2.(2\overline{S_{ij}}.\overline{S_{ij}})^2 \quad 2\text{-}7$$

Where i = 1, 2, 3 correspond to the *x*, *y* and *z* directions, respectively. The over-bar denotes the filtered quantities and u_i, ρ, P, t, τ_{ij} and ν are the fluid velocity, density, pressure, time, the SGS Reynolds stress and molecular viscosity coefficient, respectively. S_{ij}, ν_e, Δ and C_s represent the strain rate tensor, eddy viscosity, grid size and the Smagorinsky constant, respectively. δ_{ij} represents the Kronecker delta, and f_i represents the friction force for cells close to the body walls.

There are other turbulence models such as the direct numerical simulation (DNS) and Reynolds averaged Navier-Stokes (RANS) models, but we chose to use the LES for several reasons. First, 3D computations are best done with LES, while RANS should be limited to estimating time-averaged wind forces on structures [27]. Also, LES perform in general better than RANS and unsteady RANS methods because a large part of the unsteady turbulent motion is resolved and only the small scales are modelled, while in URANS and RANS all the turbulent motion scales are modelled. Although, as mentioned earlier, DNS performs much better as it resolves all the turbulent motion scales, it requires very large computations which are not feasible with the currently available computing resources. As indicated by most studies [10, 21, 28-31], the LES approach provides more detailed and accurate predictions of flow-fields (R.M.S.) around bluff bodies, which could be important for understanding the flow mechanism in fluid-structure interaction problems. However, LES needs substantially greater computing effort than RANS.

Currently, there is no turbulence model that is globally agreed on, but choosing the best fit model depends on the required accuracy and available computing resources. It is worth pointing out that two-equations RANS turbulence models can suffer from significant limitations in simulating strongly separated flows in comparison with LES (Large Eddy Simulation) approaches [32].

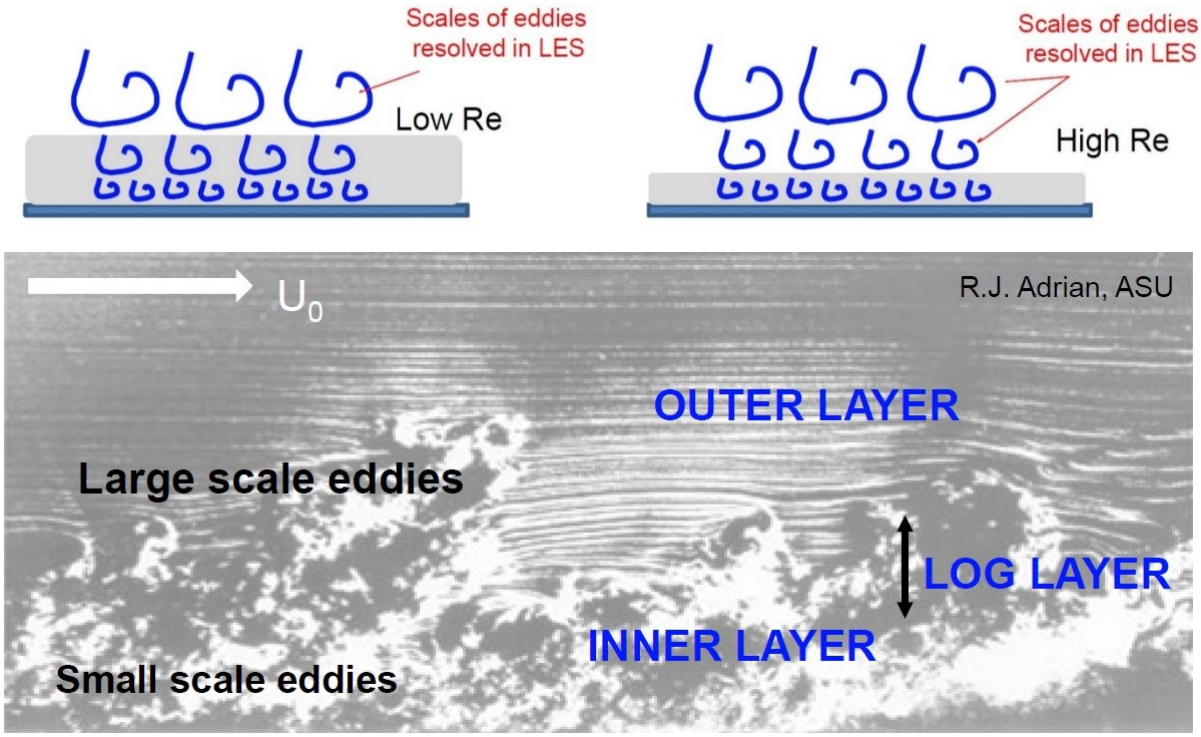

Figure 2-2 Large and small eddies [R.J. Adrian, ASU]

2.2.2 Boundary Conditions

Model boundary conditions (BC) depend on the problem under study, so their proper setting requires user experience and good physical knowledge of the problem at hand. They include inflow BC, outflow BC, transverse BC, top and bottom BC, as well as solid/fluid BC. Since, the inflow is always turbulent in wind engineering applications, techniques for generating velocity fluctuations are required.

- Inflow boundary

A fixed inlet condition is adopted here following the assumption that turbulent structures are generated in some shear-free regions of the domain, such as jets or separation regions (the latter is our case) [33]. For bluff bodies, the small-scale unsteady structures in the attached upstream flow may have a minimal effect on the downstream wakes and shear layers. This is because once separation occurs, the subsequent inherently unstable flow has a natural tendency to break down and form small fluid structures [34]. Therefore, the only quantities that are imposed on the inlet, in the present work, are the mean velocity, turbulence intensity and turbulence length scale.

- Outflow boundary condition

A suitable outflow boundary should permit the flow to exit the domain without affecting the flow in the domain near the outlet or near the body. The best practice guideline for the CFD simulation of flows in the urban environment [35] suggests that a constant static pressure should be applied at the outlet. In addition, the outlet should be far enough from the exposed object/structure.

- Transverse boundary conditions

Based on the COST 732 guidelines [35], these conditions depend on the distance between the solid and the lateral boundary. If they are close then it is recommended to use an open boundary, if they are far then enforcing a symmetry boundary condition is better. A no-slip boundary condition is used when simulating a wind tunnel experiment.

- Top and bottom boundary conditions

This boundary is encountered in 3D simulations and it is most commonly zero shear or symmetry [35].

- Solid/Fluid boundary condition

The near-wall boundary is the most important, and the no-slip boundary is the most commonly used. Noting that as the Reynolds number increases the resolution in this area should be sufficient to capture proper turbulence in the response.

2.2.3 Solution Errors

At the modeling level there are two types of solution errors: numerical modeling errors and computational errors. Computational errors arise from the residuals or truncation error in the approximations of the fundamental governing equations i.e., discretization method used. Those can be minimized by using higher order approximations (second order or higher).

Numerical modeling errors arise from the modeling choices such as turbulence, boundary conditions, grid size, etc. Numerical errors in the solution can be diminished through several methods. One of these is a grid independence study, refining the grid until converged grid-independent solutions are obtained [36]. Murakami showed that the numerical modelling error is dominant, and reducing it is most effective in reducing the total solution error. More details concerning procedures for the grid independence to ensure numerical accuracy are discussed in [36-40].

2.2.4 Validation and Verification

Computational models should be verified and validated against wind tunnel tests and numerical simulations available in the literature.

2.3 National Building Code of Canada NBC 2020 and Canadian Standards Association CSA S37-18 Review

The NBC 2015 [41] has three approaches to determine the wind loads on a building structure depending on its sensitivity to dynamic excitation. The first approach is a simplified equivalent static method that is suitable for rigid structures, where no dynamic effects are expected such as in low-rise and mid-rise buildings. The second approach (dynamic method) is for dynamically sensitive structures (0.25 Hz < f <1 Hz, h > 60m, and aspect ratio h/w > 4, where f is the fundamental frequency, h is the height and w is the width). The method is based on the Gust Factor approach, in which a factor amplifies the mean load to lead to a response similar to that resulting from the real dynamic excitation that includes fluctuating wind components. The third approach is the wind tunnel procedure for very dynamically sensitive structures (frequency < 0.25Hz, h/w > 6).

The NBC [41] and the CSA S37-18 [42], *Antennas, towers, and antenna-supporting structures* standard [43], provide two methods to determine the equivalent static wind loads on stand-alone structural members, frames, and trusses or other lattice structures. One method applicable to lattice structures uses the solidity ratio to find the resulting equivalent drag and lift forces, neglecting the properties of the actual cross-sections of individual structural elements. The other method, applicable to various individual members or complex shapes, uses the force coefficients tables provided in the Commentary I part 4 of division B table 1 and A-2, (see Appendix A), to calculate the equivalent static forces on each shape or an assembly of these shapes.

As stated in the User's guide of NBC 2015 commentary I [44], these coefficients are based on wind-tunnel (WT) experiments in which the correct velocity profile and wind turbulence were not simulated. Additionally, the shapes tested in the WT were rigid with various slenderness

ratios but fixed-end conditions, which are simplified conditions that were deemed to be conservative.

CSA S37-18 [42] for telecommunications and antenna-supporting structures does not have mandatory requirements for dynamic analysis under wind forces, but it does provide a static equivalent procedure. It is a simplified approach, provided to estimate the along-wind pressure that occurs due to wind gust and turbulence, as well as the wind velocity at which galloping, or flutter may occur.

In conclusion, the common approach prescribed in building codes is to use force coefficients in various directions for various wind conditions in which empirical constants have been determined by physical model testing (small-scale models and some on full scale) in wind tunnels. Considering the evolution of CFD, it is now becoming an efficient tool in determining these coefficients.

2.4 Studies Related to the Ensuing Work

Most published studies focusing on determining aerodynamic forces on bluff bodies are limited to objects with simple cross sections (i.e., square, circular, and rectangular cylinders). Nonetheless, few studies have focused on cross sections of lattice members such as angle and T cross-sections, and various built-up shapes of more complex geometries used in steel bridges [8, 45-49]. Similarly, most studies focusing on aero-elastic behaviour (i.e. FSI) have so far investigated typical sections of simple geometry (i.e. square and rectangular cylinders) [9, 50-52], with limited studies on the shapes used in lattice structures (i.e. single angle and 2 angles back to back). Furthermore, turbulence effects have been rarely addressed except in few experiments as in [53-55]. That is partially because it is thought that turbulence reduces the amplitude of oscillations.

In the literature there are few conclusions on the effect of the flexibility of the structure on the drag and lift coefficients especially in turbulent flows around sharp-edged bluff bodies. For instance, in a forced oscillation experiment in laminar flow, Bearman [12] performed a forced vibrations wind tunnel test in 1 DOF on a square cylinder. He found that the base pressure coefficient for the oscillating square cylinder was always larger than that of the stationary one, where it could be reduced up to 60% of its stationary value at reduced velocities below 7 and then it increased to a peak at resonance (see Figure 2-3). Since Bearman also found that oscillations had a very small effect on the front-face pressures, therefore any changes in drag coefficient will be reflected by changes in base pressure, which in return means that the drag coefficient for the oscillating cylinder was always smaller than in the static case at a similar Re. This finding is in contrast with aerodynamically smooth circular and D-shaped sections. Bearman and Luo [56] carried on a forced vibrations in 1 DOF wind tunnel test for a square cylinder and showed that at very low reduced velocities (in laminar flow) the R.M.S. fluctuating lift coefficient (C_L') is very high and then with increasing reduced velocity it drops to a minimum value, equal to about half its stationary cylinder value, see Figure 2-4. At reduced velocities above this minimum the C_L' recovers towards its stationary cylinder value as stronger vortex shedding re-establishes itself, while the drag coefficient behaves in the same way. The same results for the drag coefficient were obtained through free vibrations wind tunnel tests by Obasaju [13] in low turbulent flow (I = 0.5%) where the square cylinder was free to move in the stream-wise direction. The mean drag was amplified until it reached a maximum value close to that of the stationary force and then attenuated with increasing velocity until it settled at half the value of the stationary cylinder. Through a forced oscillatory numerical simulation Okajima [57] observed that for in-line or cross-stream oscillations, the mean drag and R.M.S. fluctuating lift increased slightly to a maximum in the lock-in range and then continuously decreased (up to Re=1000). Naudascher [14] concluded that in laminar flow, an increase in the

after-body length leads to a reduction in shear-layer curvature and forces the vortex formation to take place further downstream. This raises the base pressure and diminishes C_D, for the range of 0.6 < B/D < 2.5 whereas, for B/D > 2.5, C_D will not be greatly affected and for B/D < 0.6, C_D will increase. Bearman et al. [55] found that for the square section in laminar flow (I = 0.05%), the R.M.S. amplitude of the lift force decreased when the model was allowed to move in the cross-stream direction, C_y'(stationary) = 1.4, C_y'(rigid-flexibly supported) = 0.85-1.25. In a forced cross-stream vibrations wind tunnel test, Carassale [52] measured the drag and lift coefficients of a square prism. He found that at zero angle of attack, C_D increases to its static value as the reduced velocity increases and then suddenly drops at a reduced velocity value of around 8-10 corresponding to the lock-in region, and subsequently increases slowly to its static value. As the amplitude of forced vibration (Y) was raised the drag reduction was boosted for instance at Y/B=30% (Y is the amplitude of vibration and B is the square cylinder characteristic length), drag was reduced by 35%. The lift coefficient remained close to zero in the whole reduced velocity range.

Haan 2009 [58] implied that bodies which experience separation over smaller portions of their surface may exhibit less significant differences between stationary and oscillating model buffeting levels. If we apply this finding to the strongly bluff cross-sections under investigation, we will find that the flow is separated over the whole cross-section which means that the forces should increase in case of oscillating cylinders. Sen 2015 and He 2012 [59, 60] performed numerical investigations of the flow around flexibly supported square cylinder at low Reynolds numbers. It was concluded that the drag and lift coefficients exceed those of a stationary cylinder at reduced velocities higher than 13 Figure 2-5, and it remains to be seen whether the trend is maintained at Reynolds numbers that are more representative of turbulent wind flow conditions in exposed civil engineering structures.

There are very few studies on the angle cross-section; among them, Slater 1969 found that the unsteady aerodynamic coefficient magnitude during plunging resonance is significantly higher than that of the stationary results [8]. He also added that turbulence suppresses resonant vibrations and consequently the unsteady aerodynamic coefficient decreases. Furthermore, the unsteady forces are at a maximum for orientations in the ranges 0° < a < 45° and 95° < a < 145° (orientations based on NBC 2015 [44]). The results also indicated that galloping would happen at very low damping or only extremely high wind speeds, which is outside the range of practical interest in structural engineering [8].

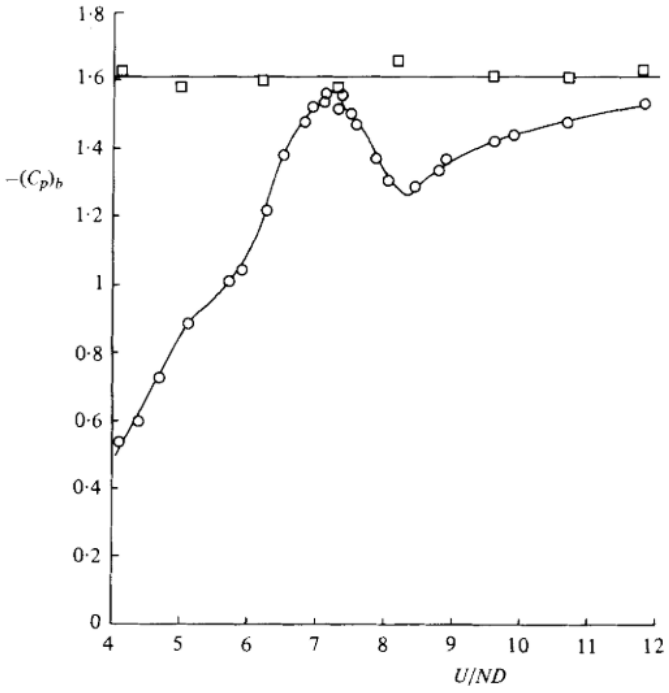

Figure 2-3 Base-pressure coefficient versus reduced velocity A/D = 0 (□), A/D= 0.1 (○)

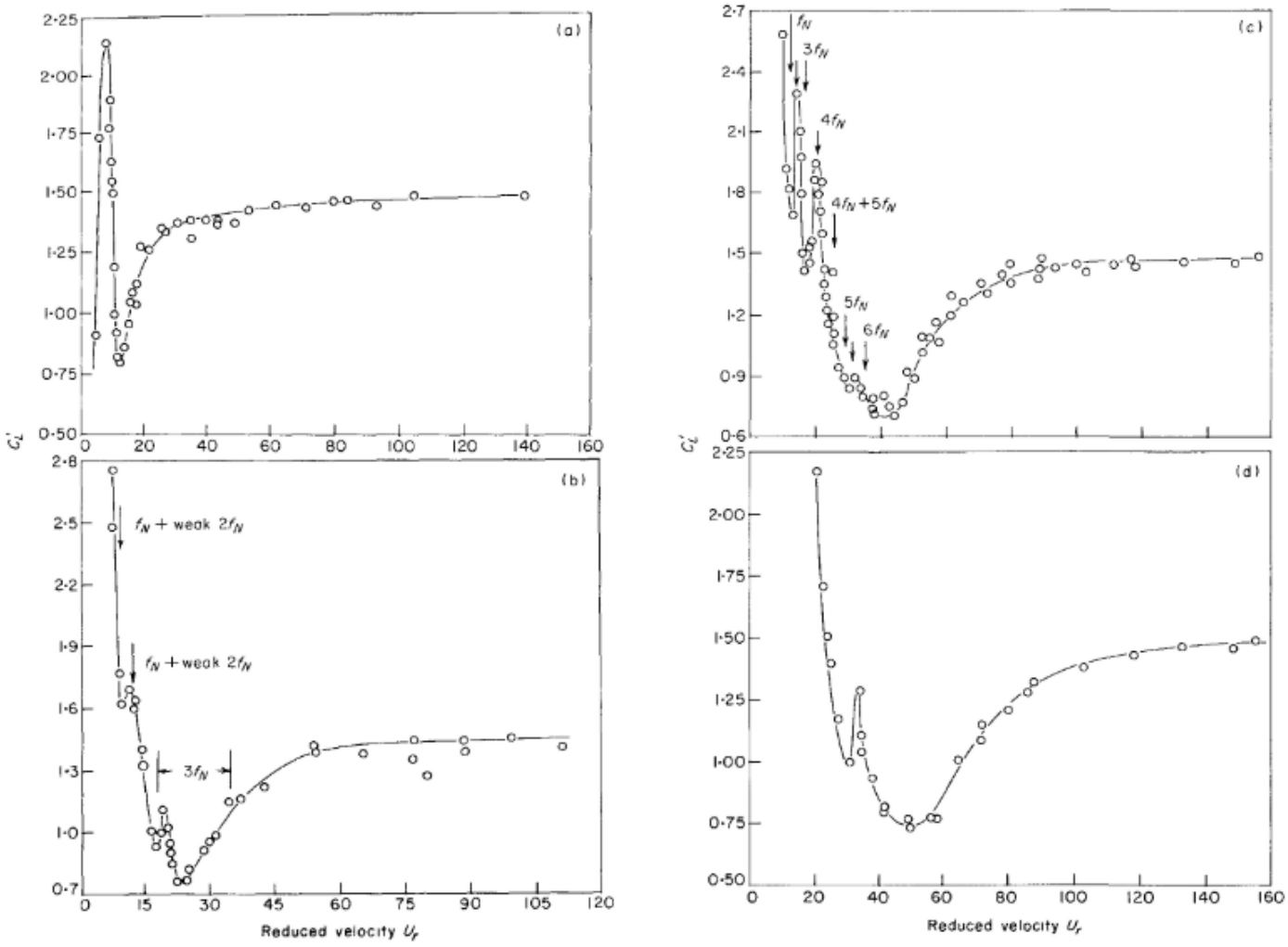

Figure 2-4 C_L' versus reduced velocity for (a) A/D = 0.25; (b) A/D = 0.675; (c) A/D = 1.5, (d) A/D = 2.0

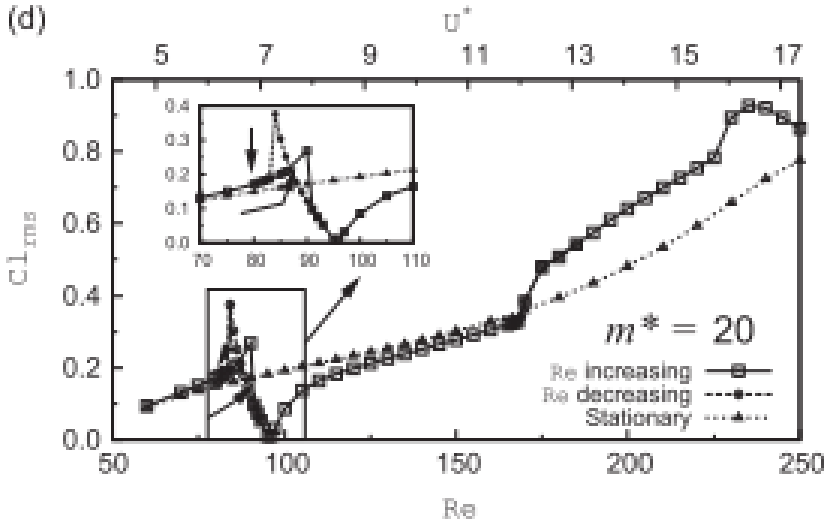

Figure 2-5 the variation of r.m.s. lift coefficient with Re and U^* for m^*

CHAPTER 3 DETERMINATION OF AERODYNAMIC DERIVATIVE FOR ONE-DEGREE-OF-FREEDOM SQUARE CYLINDER USING LARGE EDDY SIMULATION

3.1 Abstract

This study investigates the applicability of using Computational Fluid Dynamics (i.e., CFD) simulations to evaluate the aerodynamic derivatives (i.e., AD) and Wind Structure Interaction (i.e., WSI) response of free vibrating bluff bodies. The study majorly focuses on three-dimensional simulations of a rigid cylinder with a square cross-section that is elastically supported and constrained to move only in the transverse direction under wind loading. Primarily, to validate the method, the square cylinder was kept stationary, and the force coefficients were calculated at different wind angles of attack. Following that, to determine the AD, the free vibrations method or more precisely named the impulse response [61, 62] was used, where the rigid square cylinder was first pushed a fixed distance and then left to freely vibrate. The model was assigned a definite mass and damping ratio, while supported on springs with discrete stiffness in the transverse direction. Finally, the amplitude of vibration was determined through a MATLAB code employing the Newmark Beta Method. This approach was widely applied in the literature for streamlined bodies and, up to the knowledge of the authors, was not validated for the sharp-edged bluff bodies. Eventually, it was concluded that the approach used is valid and could be used in the future to estimate the flutter derivatives as well as the amplitude of vibrations for square cross-section bodies.

3.2 Introduction

The forces on bluff bodies and structures exposed to wind are complex to determine and depend on many variables, including the shape of the object, its properties, the wind direction, and the wind velocity profile. For instance, slender exposed structures such as signage structures, lighting poles, tall telecommunications structures (monopoles) and masts, can undergo significant motions under wind loads, which may induce fluid-structure interactions and consequently affect the wind flowing around them. There are different methods to assess the wind induced response [5]. One of the methods to assess the motion-induced forces on flexible structures is to identify their aerodynamic derivatives.

Scanlan et al. 1971 developed a mathematical model for the motion-induced forces as functions of the body vibration (in the along-wind, across-wind, and torsional directions), assuming a sinusoidal motion, as indicated in equations 3-1, 3-2, and 3-3 [6]. Forced or free vibration wind tunnel tests were conducted to identify the aerodynamic derivatives (AD - starred coefficients in the equations) [63-65]. More recently, researchers started using numerical simulations to calculate the AD [66, 67]. The use of AD has been effective and valued in several bridge design studies [64, 68]. Later, some studies have adopted the same concept for more rectangular shapes for turbulent and smooth flows, through numerical simulations or wind tunnel tests either by free or forced vibrations techniques [69-77].

$$L = \frac{1}{2}\,\rho\,U^2 D\left[\frac{KH_1^*\dot{y}}{U} + \frac{KH_2^* D\dot{\alpha}}{U} + K^2 H_3^*\alpha + \frac{K^2 H_4^* y}{D} + \frac{KH_5^* D\dot{p}}{U} + \frac{K^2 H_6^* p}{D}\right] \quad 3\text{-}1$$

$$M = \frac{1}{2}\,\rho\,U^2 D^2\left[\frac{KA_1^*\dot{y}}{U} + \frac{KA_2^* D\dot{\alpha}}{U} + K^2 A_3^*\alpha + \frac{K^2 A_4^* y}{D} + \frac{KA_5^* D\dot{p}}{U} + \frac{K^2 A_6^* p}{D}\right] \quad 3\text{-}2$$

$$Dr = \frac{1}{2}\,\rho\,U^2 D\left[\frac{KP_1^*\dot{y}}{U} + \frac{KP_2^* D\dot{\alpha}}{U} + K^2 P_3^*\alpha + \frac{K^2 P_4^* y}{D} + \frac{KP_5^* D\dot{p}}{U} + \frac{K^2 P_6^* p}{D}\right] \quad 3\text{-}3$$

Where, *L, M* and *Dr*: are the Lift (N/m), Moment (N.m/m) and Drag (N/m) forces, respectively, produced by the moving section

ρ: density of air (kg/m^3)

D: characteristic width of the section (m)

K: reduced frequency, ωB/U

U: wind speed at the section height (m/s)

ω: circular frequency of the object (rad/sec)

H_{1-6}^{*}, A_{1-6}^{*} and P_{1-6}^{*} are the Lift, Torsion, and Drag Aerodynamic Derivatives, respectively[1].

y: vertical motion (across-wind) (m)

p: horizontal motion (along-wind) (m)

α: rotational motion (radians)

There are two main approaches to determine the AD on a given body, namely the free and forced vibrations tests. In the forced vibration, the motion of the body is prescribed, and ADs are extracted from the recorded wind forces acting on the body. On the other hand, in the free vibration approach, the body is supported using springs and given a push and release to vibrate freely under the incoming wind condition. Aerodynamic derivatives are extracted from the recorded body motion.

Studies showed that the free and forced vibration test methods lead to acceptable AD for streamlined bodies, but there are not enough studies to confirm the same for sharp edged extremely bluff bodies [69]. For instance, Gao et al. 2016 showed that important differences

[1] They are all a function of K.

exist between the force spectra obtained in the two types of tests for a bluff body (B/D = 2); they found that the peak force values obtained in the forced vibration test were significantly lower than those obtained in the free vibration test, although the displacement spectra obtained via the two tests were in reasonable agreement [9]. This suggests that the forced vibration test tends to underestimate the aerodynamic force. As such, it is questionable whether forced vibration tests can reflect the inherent complexity of the wind-structure interactions for the bluff section, and therefore they may not be applicable to investigate the aeroelastic response of bluff bodies. Accordingly, the free vibrations technique will be employed here because it is more adequate for the ensuing work.

Most of the earlier studies utilizing CFD used the forced vibration method to extract the AD, where discrepancies occur for sharp edged extremely bluff bodies [69]. Regarding the strongly bluff bodies, the main focus of the study, there are few experiments that identified the flutter derivatives of the square cross-section through forced vibration tests while almost none through free vibration tests. For example, Matsumoto et al. 2006 and Yagi et al. 2013 calculated the flutter derivative H_1^* through the forced vibration method by pushing the model in a harmonic motion in the cross-stream direction [72, 78]. Though Matsumoto 1996 adopted the same technique, forced vibrations, there were some qualitative & quantitative discrepancies between their results [75]. In regards to numerical simulations, estimation of AD has proved to be in good agreement with experimental ones for streamlined and mildly bluff bodies [32]. Nevertheless, it is not well established for strongly bluff bodies incurring flow separation with no reattachment. It is worth mentioning that there are some mathematical models to predict the aeroelastic forces where, along with the predefined displacement, one can calculate the AD [79]. These mathematical models were derived based on a square cylinder under forced vibration, and their applicability to predict free vibration forces and amplitudes is not

extensively proven yet. Besides, wind tunnel experiments are inevitable for the prediction of certain parameters that are utilized in these mathematical models.

The current study focuses on the applicability of employing Computational Fluid Dynamics simulations to evaluate the AD of a square cylinder (as a representative of bluff bodies) using the free vibration method. In this study, the focus will be on the determination of aerodynamic derivative for the square cylinder that is rarely covered in the literature. Single degree of freedom (in the cross-stream direction) free vibration method will be utilized to identify the H_1^* aerodynamic derivative. The importance of finding the aerodynamic derivative H_1^* is that it determines the onset of instability, where if $H_1^* > 0$ this means that the aerodynamic damping is negative, and this could result in an instability. The study will investigate whether the AD will also help in estimating the amplitude of vibration for strongly bluff bodies. This is achieved by explicitly addressing the aerodynamic damping, calculated from AD to represent the aeroelastic effects.

The paper is arranged as follows. First, a 3D CFD model of a square cylinder was created and verified against wind tunnel (WT) test results. Then a free vibrations model was created to simulate the fluid-structure interaction effects on the square cylinder. The manuscript is divided into four sections. Section 1 (this section) provides an introduction about AD on bluff bodies, while section 2 provides details about the CFD model and its validation for stationary simulations. Section 3 explains the FSI free vibration model and provides the resulting AD and responses. Conclusions of the study are provided in section 4.

3.3 CFD Model

This section provides details about the employed CFD model. Studying the wind flow around a bluff body requires first knowing the nature of the fluid dynamics. The flow field around a bluff body is complicated and difficult to analyze since it is defined by impingement,

separation, free shear layers, reattachment, circulation, vortices, etc. Additionally, the flow in the atmospheric boundary layer is inherently turbulent. Therefore, fine enough grid discretization is required to analyze such flow fields with high accuracy [15].

3.3.1 Model Construction

A 3D square cylinder model was created using ANSYS FUENT V18.1 using Large Eddy Simulations described by Equations 3-4 to 3-9. Bounded central differencing scheme was used for convective terms (momentum) as it performs good for structured and unstructured mesh. Additionally, the second-order implicit scheme for unsteady terms was chosen. The SIMPLE method was used to solve the discretized equations (pressure-velocity coupling) [80]. Important factors affecting the accuracy of CFD models (e.g., flow boundary conditions, mesh, domain size, and step size) are briefly discussed next.

There are different types of turbulence models, and the most commonly used and proved effective in simulating wind flows around bluff bodies is the large eddy simulation (LES) model, which we used in the CFD model. The governing flow equations with LES representation of the turbulence (with added SGS viscosity) are given below:

$$\frac{\partial \overline{u_\iota}}{\partial x_i} = 0 \tag{3-4}$$

$$\frac{\partial \overline{u_\iota}}{\partial \mathrm{t}} + \left(\overline{u_\jmath}\right)\frac{\partial \overline{u_\iota}}{\partial x_j} = -\frac{1}{\rho}\frac{\partial \bar{P}}{\partial x_i} + \frac{\partial}{\partial x_j}\left(-\tau_{ij} + 2\nu\overline{S_{\iota\jmath}}\right) + f_i \tag{3-5}$$

$$\tau_{ij} = \overline{u_\iota u_\jmath} - \overline{u_\iota}\,\overline{u_\jmath} \tag{3-6}$$

$$\overline{S_{\iota\jmath}} = \frac{1}{2}\left(\frac{\partial \overline{u_\iota}}{\partial x_j} + \frac{\partial \overline{u_\jmath}}{\partial x_i}\right) \tag{3-7}$$

$$\tau_{ij} - \frac{1}{3}\delta_{ij}\tau_{kk} = 2\nu_e\overline{S_{ij}} \quad 3\text{-}8$$

$$\nu_e = (C_s.\Delta)^2.(2\overline{S_{ij}}.\overline{S_{ij}})^2 \quad 3\text{-}9$$

Where i = 1, 2, 3 correspond to the *x*, *y,* and *z* directions, respectively. The over-bar represents the filtered quantities and u_i, ρ, P, t, τ_{ij} and ν represent fluid velocity, density, pressure, time, the SGS Reynolds stress and molecular viscosity coefficient, respectively. S_{ij}, ν_e, Δ, and C_s represent the strain rate tensor, eddy viscosity, grid size, and the Smagorinsky constant. δ_{ij} represents the Kronecker delta, and f_i represents the friction force for cells close to the body walls.

3.3.1.1 Domain Size

The domain size was determined based on the best practice guidelines *[35, 81]*. The recommendation stated a minimum inlet and transverse distance of 5D, outlet distance of 15D, and 4D as a minimum model length to simulate the 3D effects. The grid near boundaries is set to 1/10 of the characteristic length of the model. Three simulations were held for 0.1D, 4D, and 10D: 4D gave good results, in a reasonable computational time, in comparison with the experiments as seen in Table 3-1. The same was done for the other dimensions. Therefore, the inlet was set at 10D, outlet at 22D, and side walls at 8D transverse distance from the square model center. The domain was extended 4D in the span-wise direction, with a resolution of a constant discretization step of Δz/D=0.27, see Figure 3-1. A structured mesh was used as shown in Figure 3-2.

Table 3-1 Domain length study

	0.1D	4D [35, 81]	10D
C_{Dmean}	2.2	2.1	2.118
% of error	3.7%	0.9%	0.1%
Calculation time*	0.5	1	2.5

*Normalized by the 4D case

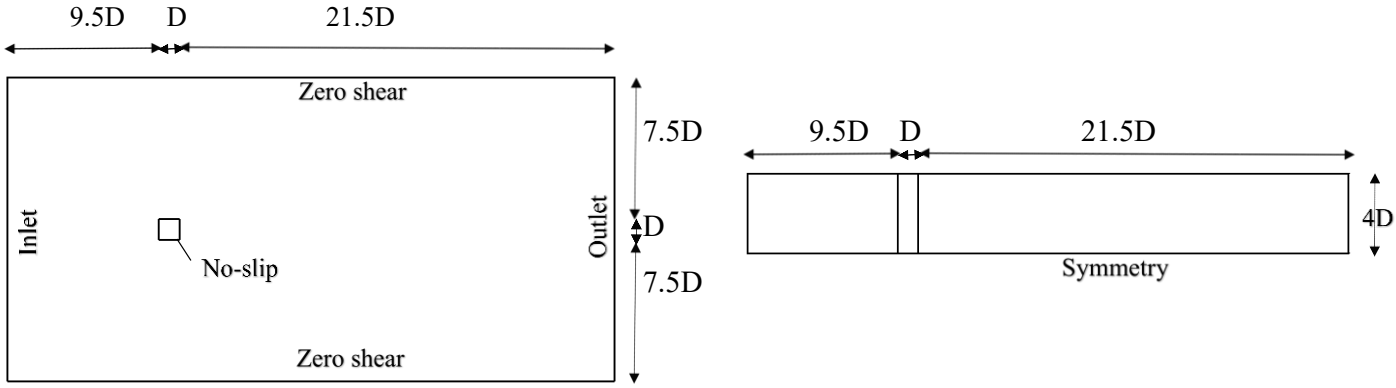

Figure 3-1 Dimensions of the CFD model

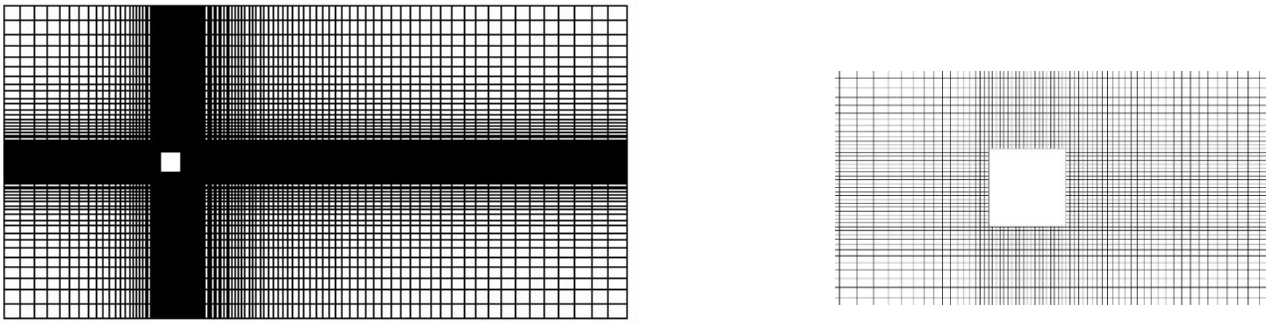

Figure 3-2 Meshing chosen and a close-up

3.3.1.2 Boundary Conditions

Model boundary conditions (BC) depend on the problem under study, so their proper setting requires user experience and good physical knowledge of the problem at hand. They include

inflow BC, outflow BC, transverse BC, top and bottom BC as well as solid/fluid BC. Since the inflow is always turbulent in wind engineering, techniques for generating velocity fluctuations are required.

In the present work, the initial conditions are imposed on the inlet which are the mean velocity, turbulence intensity, and turbulence length scale using the spectral synthesizer method. An outflow boundary was used, where flow characteristics are extrapolated from the interior [82]. As for transverse walls, a no shear boundary was chosen while symmetry was used in the span-wise direction. The fluid/solid interface was a no-slip, i.e., zero velocity at the interface.

3.3.1.3 Grid Study

The large eddy simulation model used here is a wall-modeled one, where the sub-grid scale model used is the dynamic Smagorinsky-Lilly [83]. For this type of LES, a grid study is recommended, though such grid convergence is usually not practical in LES. As a finer grid is used, a greater fraction of the turbulence spectrum is directly calculated as opposed to being modeled by a sub-grid model. The study is to show if the coarse mesh is so inadequate that it does not even correctly capture main flow phenomena. In such cases, it means that the finer solution is unacceptable to be considered [34, 84, 85]. Two meshes were tested, labeled as mesh 1 and mesh 2. Mesh 2 (Table 3-2) showed the best results with respect to running time and percent of error.

Table 3-2: Grid study with comparison to wind tunnel (exp.) and numerical results, C_{Dmean}: mean drag coefficient, C_{Lrms}: R.M.S. of lift coefficient, Δx, Δy: grid spacing near the structure in the flow and crossflow directions respectively.

	No. of elements	No. of nodes	Δt time step	Δy	Re x10^3	Blockage	C_{Dmean}	C_{Lrms}
Mesh 1	137200	148596	0.00009	0.05D	34	6.25%	2.15	1.02
Mesh 2	250320	272032	0.00009	0.05D	34	6.25%	2.1	1.1
Sarioglu exp.2005	----	----	----	----	34	6.13%	2.12	---
Huang exp. 2011	----	----	----	----	49-63	10%	2.07	----
Minguez exp. 2011	----	----	----	----	21.4	5%	2.1	----
Minguez LES 2011	n/a	n/a	n/a	n/a	21.4	7%	2.2	----
Trias DNS 2015	n/a	n/a	$9.7x10^{-4}$	n/a	22	1.8-7%	2.18	----
Bearman exp. 1982	----	----	----	----	22	5.50%	2.1	1.2

3.3.1.4 Model Parameters

The simulations were run at a Reynolds number ($R_e = \frac{\rho U \, D}{\mu}$) of 34000, where ρ (kg/m^3) is the air density and μ (kg/m.s) is the air viscosity. Each simulation was run for 45 vortex shedding cycles for approximately 350 non-dimensional time step = TU/D. The first 5 cycles were not taken into consideration on calculating the mean drag coefficient and the R.M.S lift coefficient. The non-dimensional time step (∇t U/D) was = 0.0175, to ascertain the Courant–Friedrichs–Lewy (CFL) condition (to stay below 1) for large-eddy simulations to perform well [86, 87].

$$CFL = \frac{U \, \nabla t}{\Delta} \leq 1 \qquad 3\text{-}10$$

Where, U is the inlet velocity, ∇t is the time step, T is the total time and Δ = 0.05D.

3.3.2 Validation and Verification

The model was validated at the level of the aerodynamic forces, where the square section was simulated using ANSYS FLUENT V18.1 software to calculate the forces [24]. Statistics were calculated to quantify the force and moment coefficients and compare those with the coefficients from the experiments and numerical studies [88-92].

The drag, lift, and moment coefficients (equations 3-11, 3-12 and 3-13 respectively) showed very good agreement, at different angles of attack, against experimental results, as shown in Figure 3-3 [89-91]. There are few data for the moment and lift coefficients in the literature, and we could only compare the results up to an angle of attack of 10^0. Mesh2 showed better fitting along all the angles of attack. The Strouhal number at zero angle of attack was found to be around 0.126, comparing it to the experimental value of 0.12-0.124, proves that the computations held are accurate enough. Figure 3-4 indicates that there is good agreement between experimental and numerical Strouhal number values (i.e. vortex shedding frequency) for all the angles of attack under study. Figure 3-5a shows time history of velocity magnitude at three different positions (10D, 2D and 3D) measured from inlet to the square centre. Figure 3-5b and 5c shows the velocity streamlines at the mid span of the cylinder and the velocity distribution respectively.

$$C_D = \frac{F_D}{0.5\rho U^2 DL} \qquad 3\text{-}11$$

$$C_L = \frac{F_L}{0.5\rho U^2 BL} \qquad 3\text{-}12$$

$$C_m = \frac{F_m}{0.5\rho U^2 B^2 L} \qquad 3\text{-}13$$

Where, F_D, F_L and F_m are the time averaged drag force, lift force and pitching moment respectively. ρ, U, D, B and L are the density, wind velocity, cross-stream dimension, stream-wise dimension, and span length of the model respectively.

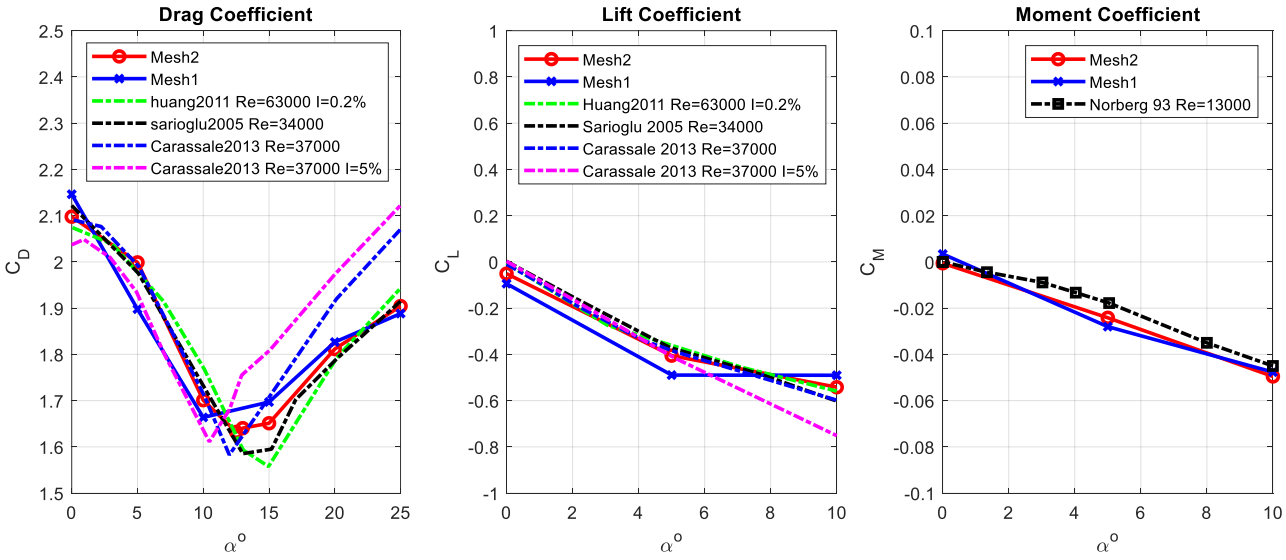

Figure 3-3 Drag, Lift and Moment coefficients

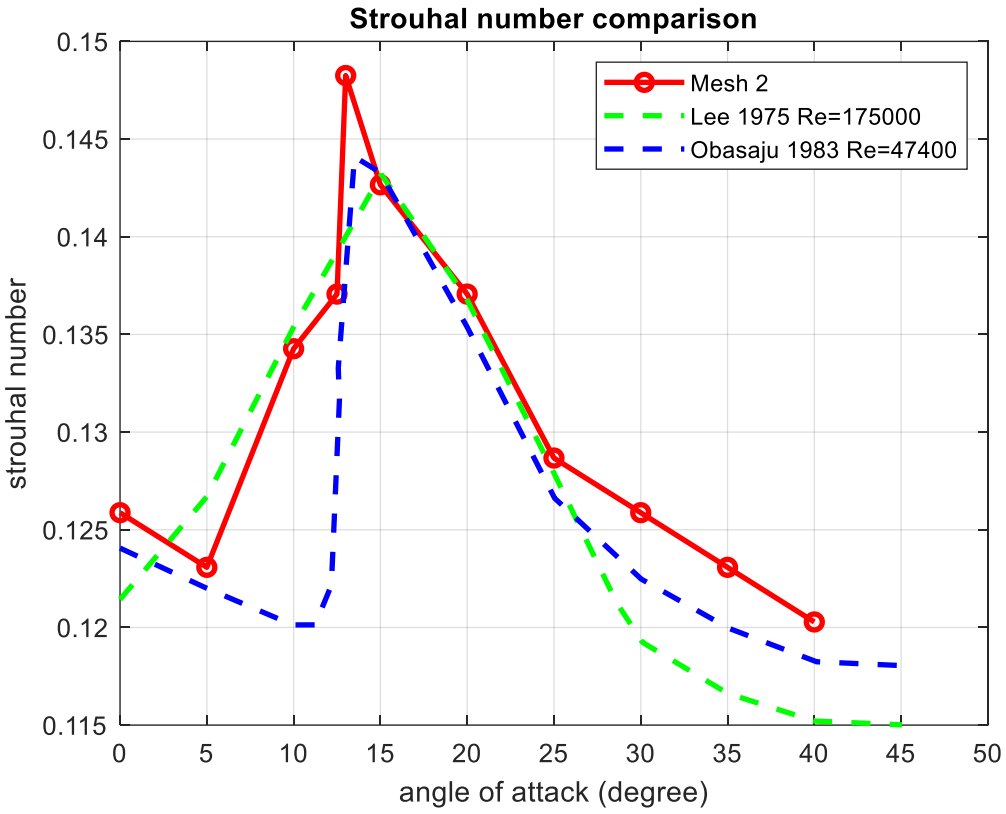

Figure 3-4 Strouhal number versus angle of attack

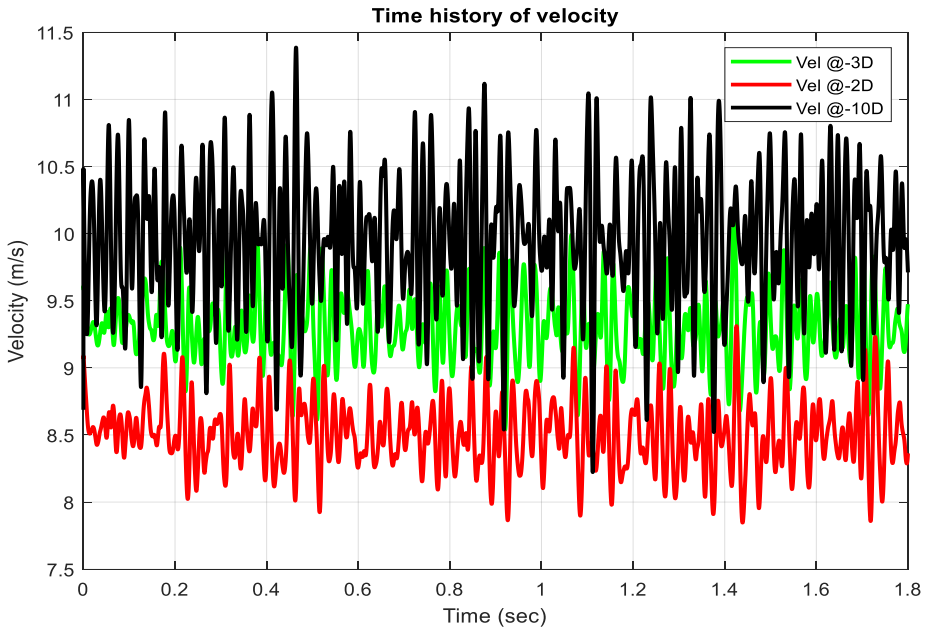

(a)

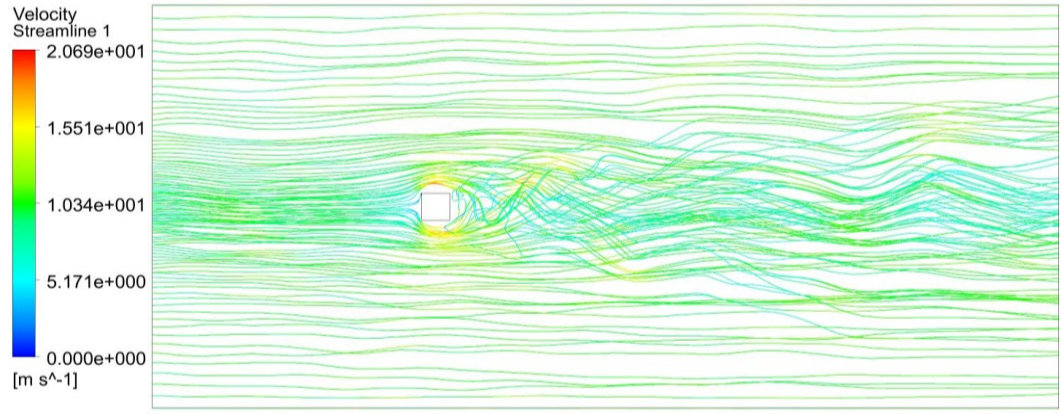

(b)

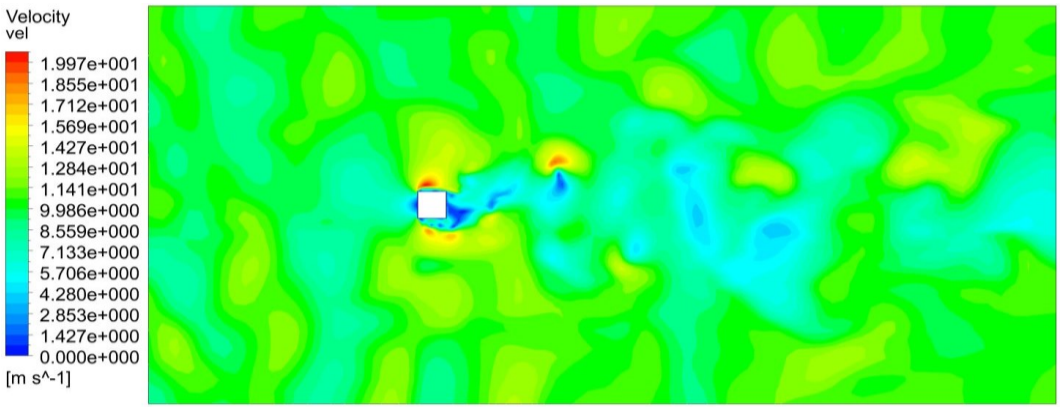

(c)

Figure 3-5 a) Velocity time history, b) Velocity streamlines, and c) Velocity contours

A very important step in the verification for the further use of this model in fluid-structure interaction models is to confirm that the transverse force coefficients is correctly calculated. In Figure 3-6, the good agreement between the numerical and experimental transverse force coefficient C_y proves that the model is capable of predicting correct forces at different angles of attack.

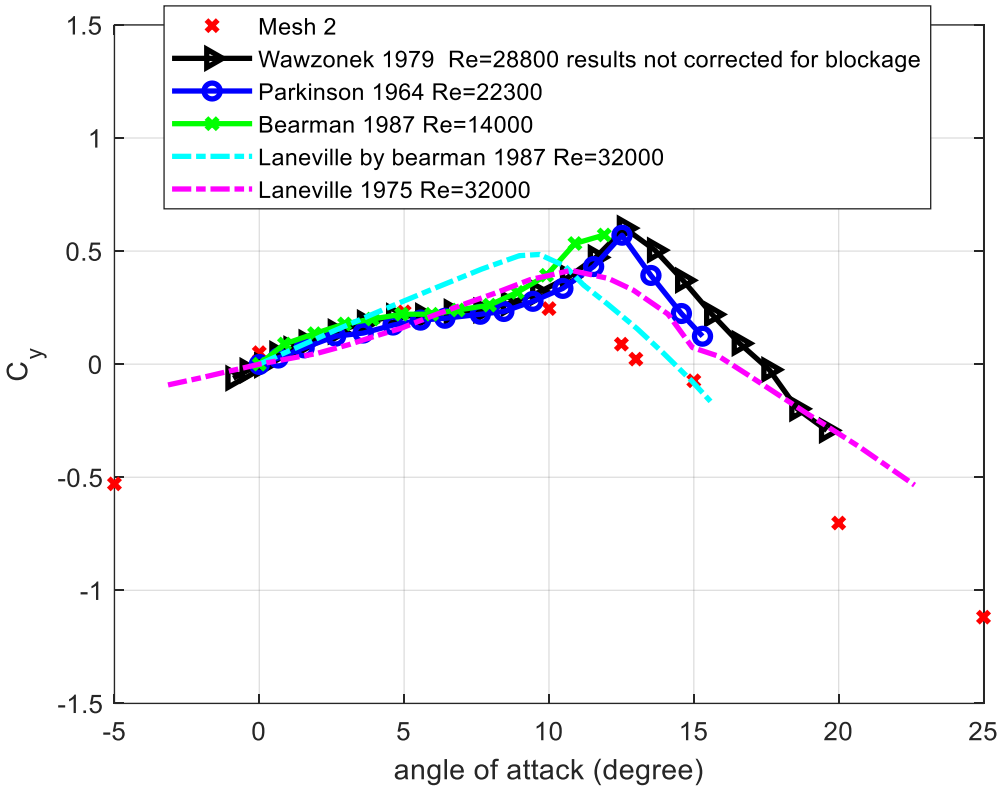

Figure 3-6 Transverse force coefficient versus the angle of attack

3.3.3 Free Vibrations Model

In this section, the bluff body (square cylinder) was allowed to freely vibrate in the cross-stream direction in an attempt to estimate the flutter derivative H_1^*. This was done by simulating the fluid-structure interaction between wind and the square cross-section using computational fluid dynamics. The square model was allowed to move only in the cross-stream direction, while the motion was restricted in the stream-wise and rotational directions, see Figure 3-7. The motion was restricted through maintaining a zero velocity in the stream-wise direction and a zero rotational velocity in the rotational direction, only the stream-wise direction was assigned a variable velocity calculated from Newmark equations 3-14 to 3-18. There are three methods to simulate this interaction known as non-coupling, weak coupling, and strong coupling methods. In the non-coupling method, it is assumed that the structure motion will not affect the fluid motion greatly (i.e., very high modal mass); therefore, the structural and fluid flow equations are independently solved. In the weak coupling method, the fluid flow is solved at a time step

then using the fluid forces, the structural equations are solved, following that the structural displacement is transferred to the fluid model. This process is repeated at each time step until reaching a statistically converged case. As for the strong coupling, the two equations are solved simultaneously. This is more realistic and theoretically rational, but it is computationally unfeasible given the available computing technology [69]. In this study, the weak coupling method was used, where the CFD model and the structural dynamics model are interchangeably solved at each time step. This method was chosen because it is computationally more efficient in comparison with the strong coupling one.

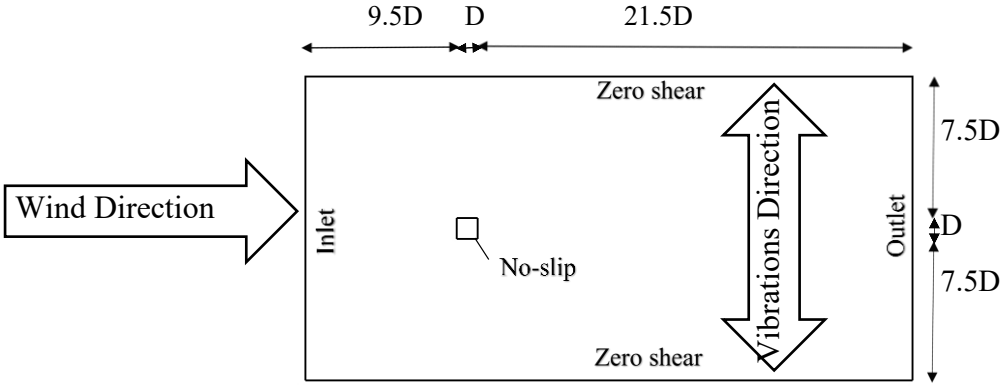

Figure 3-7 Direction of motion

3.3.4 Structural Dynamics Model

The structural dynamics model utilized is the Newmark one. The NEWMARK method was used as the direct time-step integration scheme to calculate the motion of the section in response to the wind effects. It was selected because of its accuracy and unconditional stability for single-degree-of-freedom systems. The response of the system (u, $\dot{u}, \ddot{u}$) is obtained using equations 3-14 to 3-18 [93]. The parameters applied where those of the average acceleration method with γ= 0.5 and β= 0.25. The unconditionally stable condition of 2β>= γ>= 0.5 is achieved in our case [94].

$$\hat{k} = k + \frac{\gamma}{\beta \Delta t} c + \frac{1}{\beta (\Delta t)^2} m \tag{3-14}$$

$$\hat{p}_{i+1} = p_{i+1} + \left[\frac{1}{\beta (\Delta t)^2} m + \frac{\gamma}{\beta \Delta t} c \right] u_i + \left[\frac{1}{\beta \Delta t} m + \left(\frac{\gamma}{\beta} - 1 \right) c \right] \dot{u}_i + \left[\left(\frac{1}{2\beta} - 1 \right) m + \Delta t \left(\frac{\gamma}{2\beta} - 1 \right) c \right] \ddot{u}_i \tag{3-15}$$

$$u_{i+1} = \frac{\hat{p}_{i+1}}{\hat{k}} \tag{3-16}$$

$$\ddot{u}_{i+1} = \frac{1}{\beta (\Delta t)^2} (u_{i+1} - u_i) - \frac{1}{\beta \Delta t} \dot{u}_i - \left(\frac{1}{2\beta} - 1 \right) \ddot{u}_i \tag{3-17}$$

$$\dot{u}_{i+1} = \frac{\gamma}{\beta \Delta t} (u_{i+1} - u_i) + \left(1 - \frac{\gamma}{\beta} \right) \dot{u}_i + \Delta t \left(1 - \frac{\gamma}{2\beta} \right) \ddot{u}_i \tag{3-18}$$

Where, p_{i+1} : Force at time step = t + Δt (N), u_{i+1}: Displacement at time step = t + Δt (m), $\dot{u}_{i+1}$: Velocity at time step = t + Δt (m), $\ddot{u}_{i+1}$: Acceleration at time step = t + Δt (m/s^2), m: mass (kg), K: stiffness (N/m^2), c: damping coefficient =$2m\omega_n$, where ω_n is the natural circular frequency = $\sqrt{K/m}$.

3.3.5 Fluid Structure Interaction (FSI) Governing Equations

The mesh motion was simulated using Arbitrary Lagrangian Eulerian (ALE) fluid approximation implemented in ANSYS software. The displacement-based Lagrangian approach is selected to model the interaction; in this method the mesh deforms to accommodate for the cylinder deformation by implementing the momentum equations 3-19 and 3-20 (Navier–Stokes equations) in ALE form [95, 96]:

$$\nabla . U = 0 \tag{3-19}$$

$$\rho \frac{\partial U}{\partial t} + \rho(U - \hat{v}).\nabla U = -\nabla p + \mu \nabla 2U \tag{3-20}$$

Where t, U, p, ρ and μ are time, fluid velocity, pressure, density and viscosity respectively; $\hat{v}$ refers to mesh node velocity. Re-meshing is done at each time step by spring analogy, in which the fluid mesh nodes are considered as being connected by fictitious springs whose stiffness are dependent of the locations of nodes [82, 97].

3.3.6 Fluid Structure Interaction (FSI) Weak Coupling Method

A C plus code was created to solve the equation of motion using the Newmark approach (see Appendix 1). This user-defined (UDF) code is compiled in ANSYS Fluent under user-defined functions. Rigid body motion was assigned to the square cylinder, while fluid was assigned a deforming motion. At the first-time step, lift force was calculated in the CFD solver and transferred to the UDF function where the equation of motion was solved, resulting in body displacement, velocity and acceleration. Displacement in the form of equivalent velocity is transferred back to the CFD solver and a new lift force is calculated. This process is repeated at each time step over the whole calculation time.

3.3.7 Determining the Flutter Derivative

In the Scanlan's flutter derivatives equations, the unsteady lift (L) is expressed in terms of the aerodynamic derivatives H_{1-6}^{*} assuming a three degree of freedom model (equation 1). In view of the transverse oscillation of a square cylinder, it is considered a single DOF system. Therefore, the flutter derivatives model can take the form in equation 3-21 after excluding longitudinal and torsional-freedom related terms in the model.

$$L = \frac{1}{2}\,\rho\, U^2 D\,\left[\frac{K H_1^* \dot{y}}{U} + \frac{K^2 H_4^* y}{D}\right] \qquad 3\text{-}21$$

As mentioned earlier, the free vibration method was adopted to extract the aerodynamic flutter derivatives. The numerical simulation is done in two steps. At first, the square cylinder is pushed a 0.05D displacement. After that, the fluid simulations are run with the square cylinder kept stationary at a time step of ΔtU/D = 0.016 for 20 vortex shedding cycles, approximately for dimensionless time TU/D= 160, which is enough for the wake to be fully developed. The second step is to release the cylinder and leave it to vibrate freely for 30 cycles of body vibrations, approximately for dimensionless time TU/D= 200-1000 according to the reduced velocity. Where, the reduced velocity = U/F_nD, F_n is the natural frequency = $\omega_n/2\pi$. The simulations were carried out at reduced velocity range = 0-30.

For each reduced velocity the total damping (ζ_t) is calculated using the logarithmic decrement (δ) method equation 3-22[2i]. With the knowledge of the structural damping (ζ_s), the aerodynamic damping (ζ_a) is the difference between the total and structural damping. Using the calculated aerodynamic damping we found the aerodynamic derivative H_1^* from equation 3-23[98-101].

$$\delta = \frac{2\pi\zeta_t}{\sqrt{1-\zeta_t^2}} = \frac{1}{j}\ln\left(\frac{y_i}{y_{i+1}}\right) \qquad 3\text{-}22$$

$$H_1^* = \frac{-4\,\zeta_a\, m}{\rho\, D^2} \qquad 3\text{-}23$$

[2] An example of the fit was added in Appendix B

Where, j: number of oscillations (number of peaks between y_i and y_{i+1}. m : mass of the body per unit length. ρ: density of air. D: stream-wise dimension.

The aerodynamic derivative H_1^* was compared against wind tunnel test results as shown in Figure 3-8[72, 78]. The experiments were conducted for a square cylinder forced to vibrate in the cross-stream direction with different prescribed vibration amplitudes, Y/2D = 0.025, 0.1, 0.2 and 0.3, where Y is the forced displacement amplitude and D is the square dimension. Figure 3-8 shows a good agreement between the numerical approach and the experiments. In order to further validate the approach, the aerodynamic derivative was determined at different Scruton numbers, mass ratios and Reynolds numbers. In Figure 3-9, A and B indicate different ranges of Reynolds numbers, while I, II and III indicate different Scruton numbers (Sc, equation 24) and mass ratios (m^*, equation 25) shown in Table 3-3, these were chosen to match experiments by Bearman et al. 1987, Amandolèse et al. 2010 and Hemon 2012 [55, 102, 103]. It is apparent from Figure 3-9 that the aerodynamic derivative H_1^* numerical estimation across the range of reduced velocities investigated, agree well with the experimental ones.

$$Sc = \frac{4\pi m\zeta_s}{\rho BD} \qquad 3\text{-}24$$

$$m^* = \frac{\rho BD}{2m} \qquad 3\text{-}25$$

Table 3-3 Mass ratio and Scruton number tested

Case	IA	IIA	IIIA
Mass Ratio	0.0000766	0.00055	0.0005
Scruton Number	146	9.4	74.8

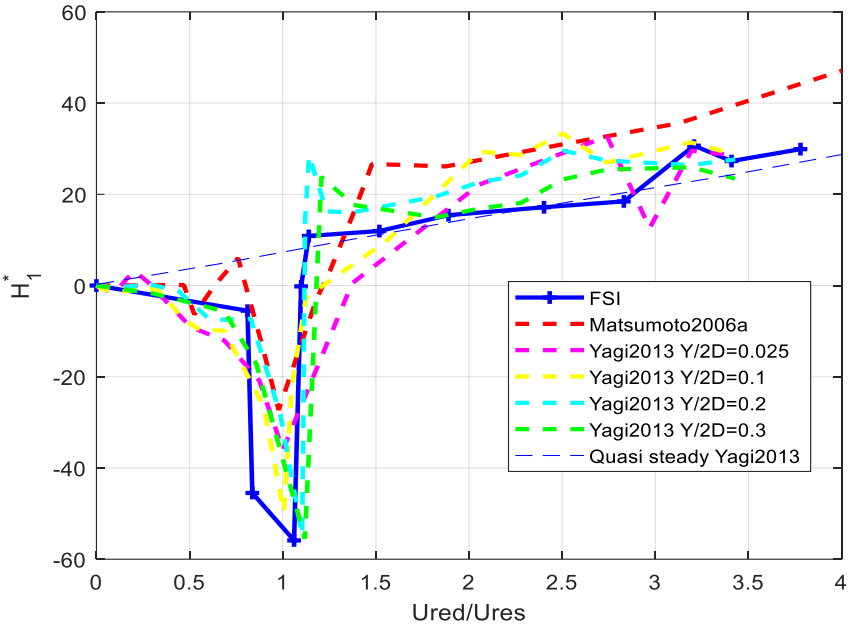

Figure 3-8 H_1^* aerodynamic derivative versus reduced velocities (U_{red})

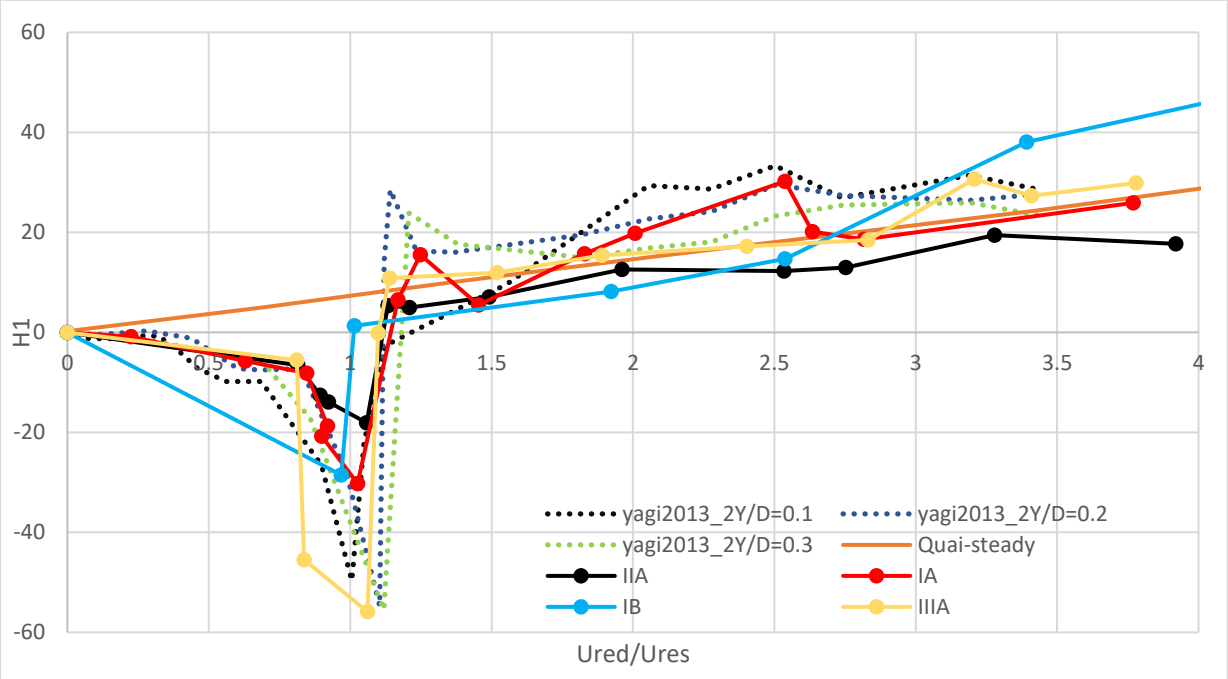

Figure 3-9 H_1^* aerodynamic derivative against reduced velocities normalized by the resonance velocity U_{res}= 1/St

3.3.7.1 Wind Structure Interaction (WSI)

The purpose of this subsection is to explore the possibility of using the ADs in determining the response of freely vibrating bluff bodies. For a square cylinder with a specific mass (m) and dimension (D), we used the aerodynamic derivative H_1^* obtained from Figure 3-8 to calculate the aerodynamic damping from Equation 23. This calculated aerodynamic damping was used to determine the amplitude of vibration for an elastically supported rigid square cylinder using the Newmark method (Equations 14-18) [104]. Using the forces (p) from CFD simulations and initial conditions of zero for displacement and velocity (from rest). The parameters chosen to match the square cylinder experiment studied by Amandolèse et al. 2010 and Shehryar 2010, were a Scruton number of 9.4, mass ratio of $5.53*10^{-4}$ and 0.0828% structural damping ratio were utilized [103, 105].

The R.M.S of displacement was calculated after the vibrations reached a steady state (limit cycle oscillations), an example of time history of vibrations reaching a steady oscillation state is apparent in Figure 3-10a and Figure 3-10b[3], the figure is at the lock in. The previous procedures were done at different wind velocities, Figure 3-10c[4] shows the amplitude of vibration normalized by the square characteristic dimension (D) versus the reduced velocity normalized by the resonance velocity. The results show relatively good agreement at the vortex induced vibration (VIV) region, where the frequency of the vortex shedding locks into the frequency of the body oscillation. A conclusion was drawn that it is only possible to predict the displacement, using the aerodynamic derivative method, at the same Scruton number at which the aerodynamic derivative was initially extracted. This was also confirmed through

[3] The beating in the signal in Figure 3-10 b) is because of the vortex shedding interaction with the body frequency of vibration.

[4] An extra point at U_{red} = 11 was added upon the request of one of the thesis examiners after the manuscript publication, and the new figure was added in Appendix C.

wind tunnel tests where the Scanlan model was unable to predict the vortex induced vibrations response of bridge decks for Scruton numbers different from the ones at which the derivatives were identified [106].

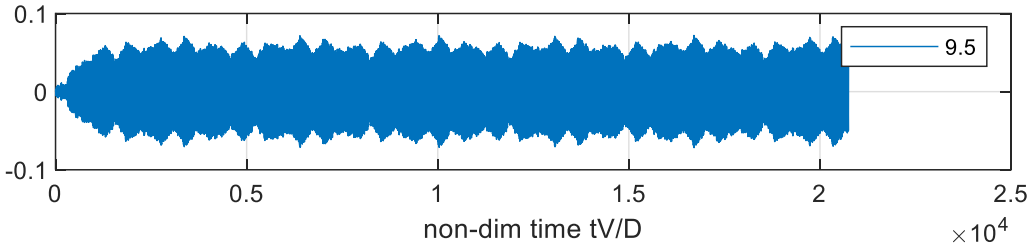

a) $U_{red} = 9.5$

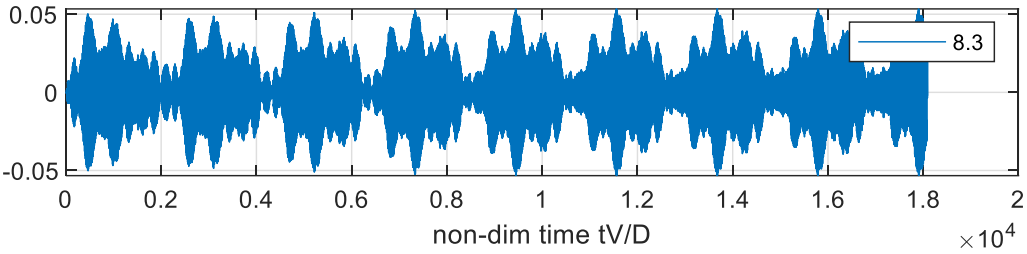

b) $U_{red} = 8.3$

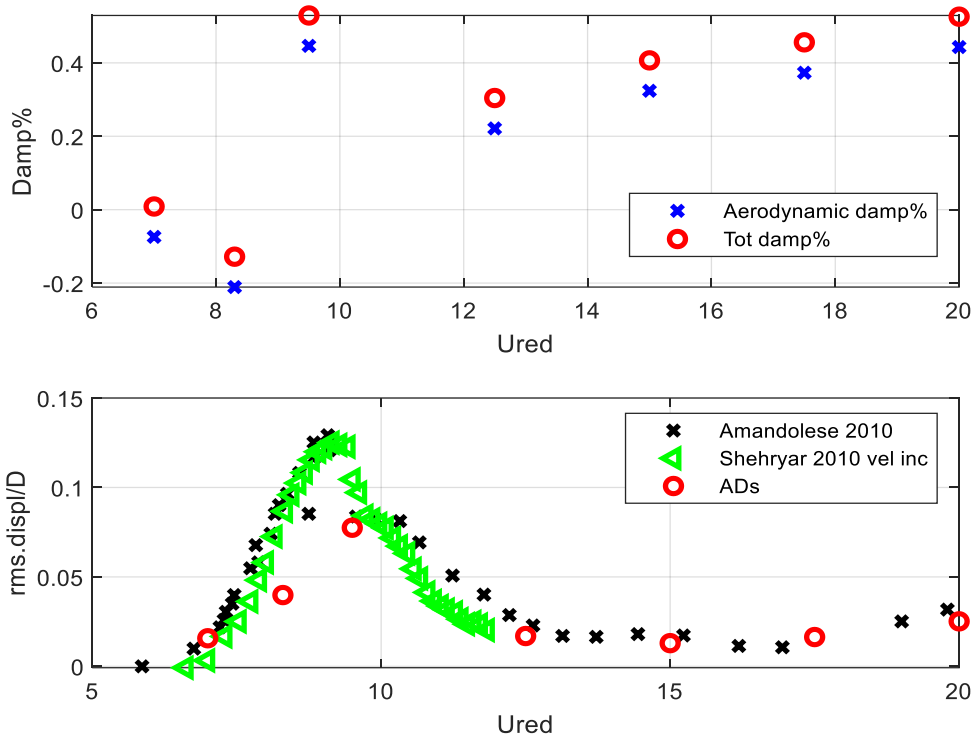

c)

Figure 3-10 a) displacement time history for U_{red} = 9.5 b) displacement time history for U_{red} = 8.3 c) Aerodynamic and total damping vs U_{red} and the lower graph is the RMS y/D vs U_{red}

3.4 Conclusion

In this study, first the flow around a square cylinder was simulated using large eddy simulation at different angles of attack. Then, fluid-structure interaction simulations were conducted assuming the square cylinder of a predefined mass is supported on springs with certain damping. From these simulations, the aerodynamic derivative H_1^* was calculated, which was used to predict the response of the freely vibrating square to wind flow.

The following conclusions can be deduced from analyzing the results obtained from the developed simulations.

- Numerical 3D simulations using LES turbulent model proved to be a reliable tool in the estimation of aerodynamic derivatives for single degree of freedom systems.
- The free vibration method for the identification of the aerodynamic derivatives for strongly bluff bodies is possible, and it yields comparable results. This allows for incorporating this method in the early design stages.
- The method applied using the Scanlan model aerodynamic derivatives could be used to predict the amplitude of vibration at the same Scruton number at which the derivatives were initially identified.

3.5 Acknowledgement

The authors would like to acknowledge the support of the National Science and Engineering Research Council of Canada for its financial support.

REFERENCES

1. Sundaram, P., T.K. Sengupta, and S. Sengupta, *Is Tollmien-Schlichting wave necessary for transition of zero pressure gradient boundary layer flow?* Physics of Fluids, 2019. **31**(3): p. 031701.
2. Sengupta, T.K., *Instabilities of Flows and Transition to Turbulence*. 2012, CRC Press: Hoboken.
3. Su, N., S. Peng, and N. Hong, *Universal simplified spectral models and closed form solutions to the wind-induced responses for high-rise structures*. Results in Engineering, 2021. **10**: p. 100230.
4. Scanlan, R.H. and J. Tomo, *Air foil and bridge deck flutter derivatives.* Journal of Soil Mechanics & Foundations Div, 1971.
5. Šarkić, A., et al., *Bridge flutter derivatives based on computed, validated pressure fields.* Journal of Wind Engineering and Industrial Aerodynamics, 2012. **104-106**: p. 141-151.
6. Sarkar, P.P., N.P. Jones, and R.H. Scanlan, *Identification of aeroelastic parameters of flexible bridges.* Journal of Engineering Mechanics, 1994. **120**(8): p. 1718-1742.
7. Nayak, S., *Uncertain quantification of field variables involved in transient convection diffusion problems for imprecisely defined parameters*. International Communications in Heat and Mass Transfer, 2020. **119**: p. 104894.
8. Larsen, A. and J.H. Walther, *Discrete vortex simulation of flow around five generic bridge deck sections.* Journal of Wind Engineering and Industrial Aerodynamics, 1998. **77-78**: p. 591-602.
9. Tamura, K.S.T.I.a.Y., *Prediction of aeroelastic aharacteristics of rectangular cross-sections by k-w model.* Structures 2004: Building on the Past, Securing the Future, 2004.

10. Scanlan, R., *Motion-related body-force functions in two-dimensional low-speed flow.* Journal of Fluids and Structures, 2000. **14**(1): p. 49-63.

11. Xu, F. and Z. Zhang, *Free vibration numerical simulation technique for extracting flutter derivatives of bridge decks.* Journal of Wind Engineering and Industrial Aerodynamics, 2017. **170**: p. 226-237.

12. Bouris, D. and G. Bergeles, *2D LES of vortex shedding from a square cylinder.* Journal of Wind Engineering and Industrial Aerodynamics, 1999. **80**(1): p. 31-46.

13. Cao, B. and P.P. Sarkar, *Identification of rational functions using two-degree-of-freedom model by forced vibration method*. Engineering Structures, 2012. **43**: p. 21-30.

14. M. Matsumoto, T.Y., J. H. Lee, K. Hori, Y. Kawashima, *Karman vortex effect on the aerodynamic forces to rectangular cylinders*. Vol. 9. 2006.

15. Matsumoto, M., Y. Kobayashi, and H. Shirato, *The influence of aerodynamic derivatives on flutter.* Journal of Wind Engineering and Industrial Aerodynamics, 1996. **60**: p. 227-239.

16. Brar, P.S., R. Raul, and R.H. Scanlan, *Numerical calculation of flutter derivatives via indicial functions.* Journal of Fluids and Structures, 1996. **10**(4): p. 337-351.

17. Matsumoto, M., *Aerodynamic damping of prisms.* Journal of Wind Engineering and Industrial Aerodynamics, 1996. **59**(2): p. 159-175.

18. Mannini, C., *Applicability of URANS and DES simulations of flow past rectangular cylinders and bridge sections*. Computation, 2015. **3**(3): p. 479.

19. Nayak, S. and S. Chakraverty, *Non-probabilistic approach to investigate uncertain conjugate heat transfer in an imprecisely defined plate*. International Journal of Heat and Mass Transfer, 2013. **67**: p. 445-454.

20. Gao, G. and L. Zhu, *Measurement and verification of unsteady galloping force on a rectangular 2:1 cylinder.* Journal of Wind Engineering and Industrial Aerodynamics, 2016. **157**(Supplement C): p. 76-94.

21. Yagi, T., et al., *Interferences of vortex sheddings in galloping instability of rectangular cylinders.* Kozo Kogaku Ronbunshu. A (Journal of Structural Engineering. A), 2013. **59A**: p. 552-561.

22. de Miranda, S., et al., *On the identification of flutter derivatives of bridge decks via RANS turbulence models: Benchmarking on rectangular prisms*. Engineering Structures, 2014. **76**: p. 359-370.

23. Liu, Y.Z., et al., *A new modeling approach for forced transversely oscillating square-section cylinders*. Journal of Fluids and Structures, 2018. **81**: p. 492-513.

24. Murakami, S., *Current status and future trends in computational wind engineering.* Journal of Wind Engineering and Industrial Aerodynamics, 1997. **67**: p. 3-34.

25. Sarwar, M.W., et al., *Prediction of aerodynamic characteristics of a box girder bridge section using the LES turbulence model.* Journal of Wind Engineering and Industrial Aerodynamics, 2008. **96**(10): p. 1895-1911.

26. Jörg Franke, A.H., HA Schlunzen, Bertrand Carissimo. *The best practise guideline for the CFD simulation of flows in the urban environment: an outcome of COST 732*. in The Fifth International Symposium on Computational Wind Engineering. Chapel Hill, North Carolina, USA. 2010.

27. Franke, J., *Best practice guideline for the CFD simulation of flows in the urban environment*. 2007: Meteorological Inst.

28. Fluent, A., *15.0 Documentation.* Ansys Inc, 2009.

29. Meneveau, C., T.S. Lund, and W.H. Cabot, *A Lagrangian dynamic subgrid-scale model of turbulence.* Journal of fluid mechanics, 1996. **319**: p. 353-385.

30. Georgiadis, N.J., D.P. Rizzetta, and C. Fureby, *Large-eddy simulation: current capabilities, recommended practices, and future research.* AIAA journal, 2010. **48**(8): p. 1772-1784.

31. Ricci, M., L. Patruno, and S. de Miranda, *Wind loads and structural response: Benchmarking LES on a low-rise building.* Engineering Structures, 2017. **144**: p. 26-42.

32. Kawai, S. and J. Larsson, Wall-modeling in large eddy simulation: Length scales, grid resolution, and accuracy. Physics of Fluids, 2012. **24**(1): p. 015105.

33. Courant, R., *On the partial difference equations of mathematical physics.* Mathematische Annalen, 1928. **100**: p. 32-74.

34. Courant, R., K. Friedrichs, and H. Lewy, *On the partial difference equations of mathematical physics.* IBM journal of Research and Development, 1967. **11**(2): p. 215-234.

35. ANSYS Fluent V18.1. ANSYS, Inc.

36. M. Minguez, C.B., R. Pasquetti, E. Serre, *Experimental and high-order LES analysis of the flow in near-wall region of a square cylinder.* International Journal of Heat and Fluid Flow, 2011. **32**(3): p. 558-566.

37. Carassale, L., A. Freda, and M. Marrè-Brunenghi, *Effects of free-stream turbulence and corner shape on the galloping instability of square cylinders.* Journal of Wind Engineering and Industrial Aerodynamics, 2013. **123**: p. 274-280.

38. Sarioglu, M., Y.E. Akansu, and T. Yavuz, *Control of the flow around square cylinders at incidence by using a rod.* AIAA journal, 2005. **43**(7): p. 1419-1426.

39. Huang, R.F. and B.H. Lin, Effects of Flow Patterns on Aerodynamic Forces of a Square Cylinder at Incidence. Journal of Mechanics, 2011. **27**(3): p. 347-355.

40. Trias, F.X., A. Gorobets, and A. Oliva, *Turbulent flow around a square cylinder at Reynolds number 22,000: A DNS study.* Computers & Fluids, 2015. **123**: p. 87-98.

41. Chopra, A.K., *Dynamics of Structures: Theory and applications to earthquake engineering 4th edition*. 2012, University of California at Berkeley.

42. Soltys, R., M. Tomko, and S. Kmet, *Analysis of wind-induced vibrations of an anchor cable using a simplified fluid–structure interaction method*. Applied Mathematics and Computation, 2015. **267**: p. 223-236.

43. Wang, X.S., *Fundamentals of fluid-solid interactions: analytical and computational approaches*. Vol. 8. 2008: Elsevier.

44. Donea, J., et al., *Arbitrary lagrangian-eulerian methods, volume 1 of Encyclopedia of Computational Mechanics, chapter 14*. John Wiley & Sons Ltd, 2004. **3**: p. 1-25.

45. Blom, F.J., *Considerations on the spring analogy.* International journal for numerical methods in fluids, 2000. **32**(6): p. 647-668.

46. Hemon, P., *Large galloping oscillations of a square section cylinder in wind tunnel.* Flow-Induced Vibrations, FIV2012, Dublin, Ireland, July, 2012: p. 3-6.

47. P. W. Bearman, I.S.G., D. J. Maull, G. V. Parkinson, *Experiments on flow-induced vibration of a square-section cylinder.* Journal of Fluids and Structures, 1987. **1**(1): p. 19-34.

48. Amandolese, X. and P. Hémon, *Vortex induced vibration of a square cylinder in wind tunnel.* Comptes Rendus Mécanique, 2010. **338**(1): p. 12-17.

49. Nayak, S. and S. Chakraverty, *Interval finite element method with MATLAB*. 2018: Academic Press.

50. Shehryar, M., *Transient instability mechanisms by frequency coalescence in fluid structure systems.* 2010, École Polytechnique.

51. Marra, A.M., C. Mannini, and G. Bartoli, *Measurements and improved model of vortex-induced vibration for an elongated rectangular cylinder.* Journal of Wind Engineering and Industrial Aerodynamics, 2015. **147**(Supplement C): p. 358-367.

APPENDIX 1

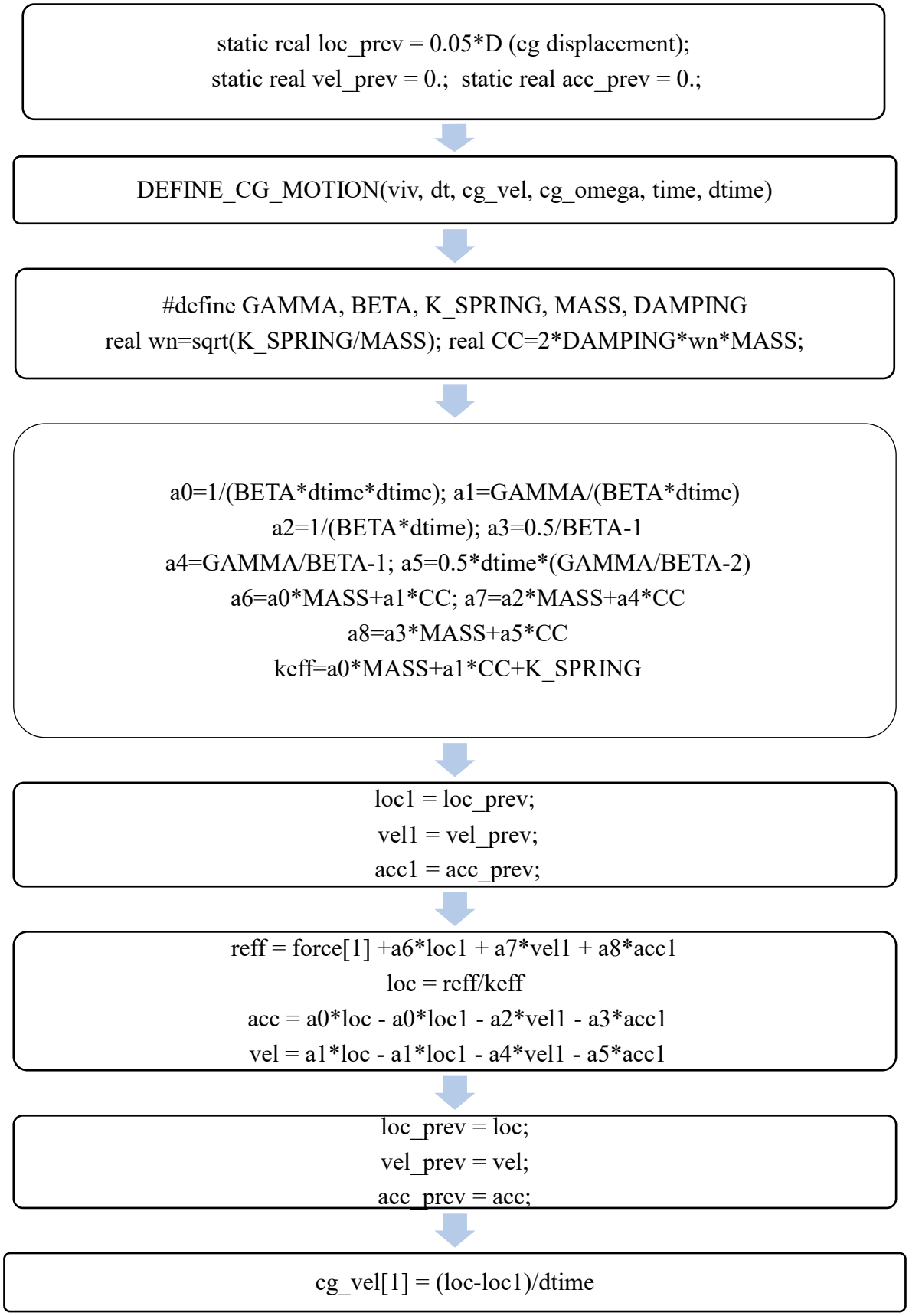
static real loc_prev = 0.05*D (cg displacement);
static real vel_prev = 0.; static real acc_prev = 0.;
DEFINE_CG_MOTION(viv, dt, cg_vel, cg_omega, time, dtime)
#define GAMMA, BETA, K_SPRING, MASS, DAMPING
real wn=sqrt(K_SPRING/MASS); real CC=2*DAMPING*wn*MASS;
a0=1/(BETA*dtime*dtime); a1=GAMMA/(BETA*dtime)
a2=1/(BETA*dtime); a3=0.5/BETA-1
a4=GAMMA/BETA-1; a5=0.5*dtime*(GAMMA/BETA-2)
a6=a0*MASS+a1*CC; a7=a2*MASS+a4*CC
a8=a3*MASS+a5*CC
keff=a0*MASS+a1*CC+K_SPRING
loc1 = loc_prev;
vel1 = vel_prev;
acc1 = acc_prev;
reff = force[1] +a6*loc1 + a7*vel1 + a8*acc1
loc = reff/keff
acc = a0*loc - a0*loc1 - a2*vel1 - a3*acc1
vel = a1*loc - a1*loc1 - a4*vel1 - a5*acc1
loc_prev = loc;
vel_prev = vel;
acc_prev = acc;
cg_vel[1] = (loc-loc1)/dtime

BRIDGING BETWEEN CHAPTERS THREE AND FOUR

In chapter three, flutter derivatives were determined using numerical fluid-structure interaction (FSI) simulations for strongly bluff bodies. The approach of utilizing these flutter derivatives to assess the response and forces on similar bodies proved to be effective, as the results aligned well with existing literature. Consequently, the identification of flutter derivatives through FSI was deemed valid and produced favorable results.

The subsequent objective involved finding flutter derivatives for more complex bodies, specifically members and parts of lattice structures. While FSI simulations remained feasible, the main challenge was the computational time required. Additionally, the lack of wind tunnel experiments and available published results for these specific structural models posed a hurdle in the validation and verification process.

To overcome these issues, new wind tunnel tests were conducted for the angle cross-section member and truss under investigation. Notably, this type of free vibrations wind tunnel test was conducted for the first time by this thesis research group at Toronto Metropolitan University (formerly Ryerson University). Chapter four provides comprehensive details on the design of the testing system, equipment selection, and calibration procedures.

Chapter 4 primarily focuses on the system developed to measure free vibrations, outlines the equipment utilized, and elaborates on the calibration process. Subsequently, the system is employed to measure the forces acting on the vibrating model. Additionally, the displacements and aerodynamic damping were calculated and utilized to find the flutter derivatives for the tested structures.

CHAPTER 4 DETERMINING AERODYNAMIC DERIVATIVES FOR MEMBERS OF LATTICE STRUCTURES THROUGH WIND TUNNEL TESTING

4.1 Abstract

This paper presents wind tunnel experiments to determine aerodynamic derivatives for three models through the free vibration technique. The three models are elements and parts of lattice structures: a cylinder with square cross-section, a member with equal-leg angled cross-section, and a lattice structure. The models were assumed to be rigid objects with measured mass and damping ratio, while supported on springs with predetermined stiffness in the transverse direction to observe possible fluid-structure interactions: This is to mimic a part of the structure where the springs represent the flexibility at that part as it moves in the flow. Each model was tested using the free vibration method, where the model was given an initial displacement and then left to freely vibrate while monitoring the forces in the supporting springs. Afterwards, the displacements were measured, and the total damping was extracted from the time histories of the displacements. Consequently, the aerodynamic derivative (H_1^*) is calculated from the total damping with the knowledge of the structural damping measured. The first model (cylinder with square cross-section) has been experimentally studied in the literature but with a different identification technique which is the forced vibration [72, 78]. The results provide the aerodynamic derivative (H_1^*) for models that were not studied before in the literature. The aerodynamic derivative is then used to determine wind loads taking the fluid-structure interaction into consideration.

4.2 Introduction

The aerodynamic derivatives are one of the methods to assess the motion-induced forces on flexible structures. Scanlan et al. 1971 developed a mathematical model for the motion-induced

forces as functions of the body vibration (in the along-wind, across-wind, and torsional directions), assuming a sinusoidal motion, as indicated in equations 4-1, 4-2, and 4-3 [6]. The motion-induced forces are determined from equations 1-3 for a certain object with the knowledge of the predetermined aerodynamic derivatives (AD - starred coefficients in the equations) while measuring the motion amplitudes. The aerodynamic derivatives are predetermined for the same shape through forced or free vibration wind tunnel tests [63, 64]. More recently, researchers started using numerical simulations to calculate the AD [66, 67]. The use of AD has been effective and valued in several bridge design studies [64, 68]. Later, some studies have adopted the same concept for more rectangular shapes (not streamlined) for turbulent and smooth flows, through numerical simulations or wind tunnel tests either by free or forced vibrations techniques [69-76].

$$L = \frac{1}{2}\,\rho\,U^2 D\,[\frac{KH_1^*\dot{y}}{U} + \frac{KH_2^*D\dot{\alpha}}{U} + K^2H_3^*\alpha + \frac{K^2H_4^*y}{D} + \frac{KH_5^*D\dot{p}}{U} + \frac{K^2H_6^*p}{D}] \quad 4\text{-}1$$

$$M = \frac{1}{2}\,\rho\,U^2 D^2\,[\frac{KA_1^*\dot{y}}{U} + \frac{KA_2^*D\dot{\alpha}}{U} + K^2A_3^*\alpha + \frac{K^2A_4^*y}{D} + \frac{KA_5^*D\dot{p}}{U} + \frac{K^2A_6^*p}{D}] \quad 4\text{-}2$$

$$Dr = \frac{1}{2}\,\rho\,U^2 D\,[\frac{KP_1^*\dot{y}}{U} + \frac{KP_2^*D\dot{\alpha}}{U} + K^2P_3^*\alpha + \frac{K^2P_4^*y}{D} + \frac{KP_5^*D\dot{p}}{U} + \frac{K^2P_6^*p}{D}] \quad 4\text{-}3$$

Where, *L, M* and *Dr* are the Lift (N/m), Moment (N.m/m) and Drag (N/m) forces, respectively, produced by the moving section

ρ: density of air (kg/m^3)

D: characteristic width of the section (m)

K: reduced frequency, ωB/U

U: wind speed at the section height (m/s)

ω: circular frequency of the object (rad/sec)

H_{1-6}^*, A_{1-6}^* and P_{1-6}^* are the Lift, Torsion, and Drag Aerodynamic Derivatives, respectively

y: vertical motion (across-wind) (m)

p: horizontal motion (along-wind) (m)

α: rotational motion (radians)

The ADs of a given body could be determined through either free or forced vibrations tests. In the forced vibration, a sinusoidal motion of the body is prescribed, and ADs are extracted from the recorded wind forces acting on the body and the forced motion amplitude. Alternatively, in the free vibration approach, the body is given a push and then left to move freely under the incoming wind condition. The body is supported on springs and its aerodynamic characteristics (mass, stiffness and damping) are assessed before testing. The time histories of the recorded body forces and motion are used to find aerodynamic derivatives. Several studies showed that both methods lead to acceptable ADs for streamlined bodies, but there are not enough studies to confirm the same for bluff bodies. For instance, Gao et al. 2016 showed that important differences exist between the force spectra obtained in the two types of tests for a bluff body (B/D = 2); they found that the peak force values obtained in the forced vibration test were significantly lower than those obtained in the free vibration test, although the displacement spectra obtained via the two tests were in reasonable agreement [9]. These observations made it questionable whether forced vibration tests can reflect the inherent complexity of the wind-structure interactions for the bluff section, and therefore they may not be applicable to investigate the aero-elastic response of bluff bodies. Accordingly, the free vibrations technique is used here because it is more adequate for the cross-sections under investigation.

The current study focuses on the evaluation of the AD for three sections as representatives of bluff bodies through wind tunnel experiments using the free vibration method. Regarding the square cross-section there are few experiments that identified its flutter derivatives through forced vibration tests while almost none through free vibration tests. For example, Matsumoto et al. 2006 and Yagi et al. 2013 calculated the flutter derivative H_1^* through the forced vibration

method by pushing the model in a harmonic motion in the cross-stream direction [72, 78]. Though Matsumoto 1996 adopted the same technique of forced vibrations, there were some qualitative and quantitative discrepancies between their results, which adds to the claims of the unsuitability of the method for strongly bluff bodies [75].

The other two models are rarely covered in the literature [8]. Single-degree-of-freedom (in the cross-stream direction) free vibration method will be utilized to identify the H_1^* aerodynamic derivative. The importance of finding the aerodynamic derivative H_1^* is that it determines the onset of instability; $H_1^* > 0$ this means that the aerodynamic damping is negative, and this could result in motion instability if structural damping is insufficient.

This chapter is divided into four sections. The first section (this section) provides an introduction on ADs on bluff bodies. The second section describes the wind tunnel (WT) test facility along with the test setting and measuring equipment. The third section explains the test procedures followed by the validation of the wind tunnel setting and procedures for the square cross-section test. The fourth section is dedicated to providing details about the angle cross-section and the lattice structure as well as their measured ADs. Conclusions of the study are provided in section five.

4.3 Wind Tunnel

The current experimental work took place in the wind tunnel test facility located at Toronto Metropolitan University (TMU, formerly Ryerson University). This section provides details about the dimensions and operating system of the wind tunnel followed by an illustration of the system that was installed to accommodate the testing requirements in free vibrations.

4.3.1 Wind Tunnel Facility

The TMU wind tunnel is a closed-loop one that operates on a huge fan that has a range of speeds from 4 m/s up to 30 m/s. The tunnel allows for smooth flow. The test section is the

narrowest part of the tunnel as shown in Figure 4-1, the cross-section is a 91x91 cm, see Figure 4-2. Refer to [107] for more details about the wind tunnel facility.

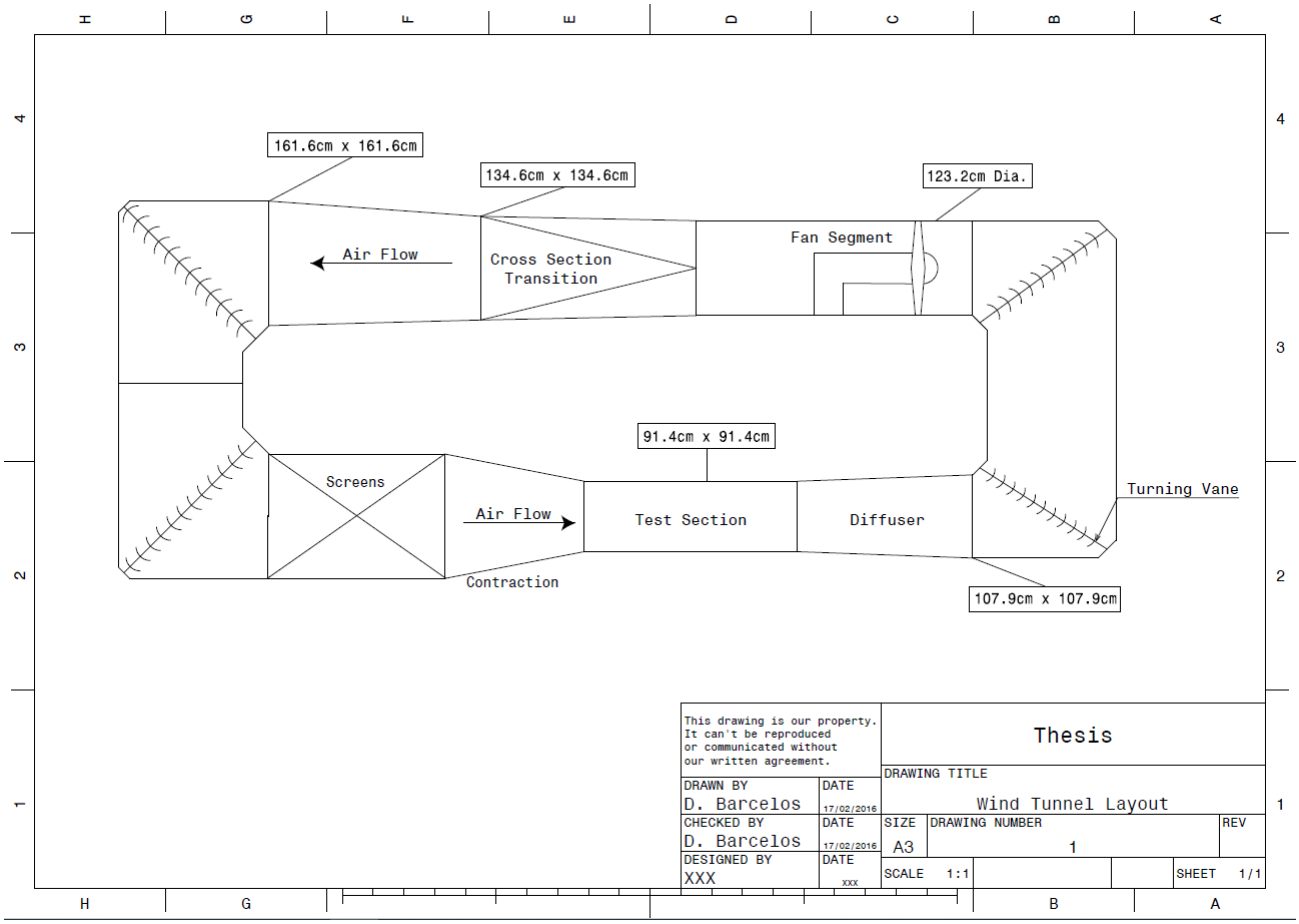

Figure 4-1: Wind tunnel Layout

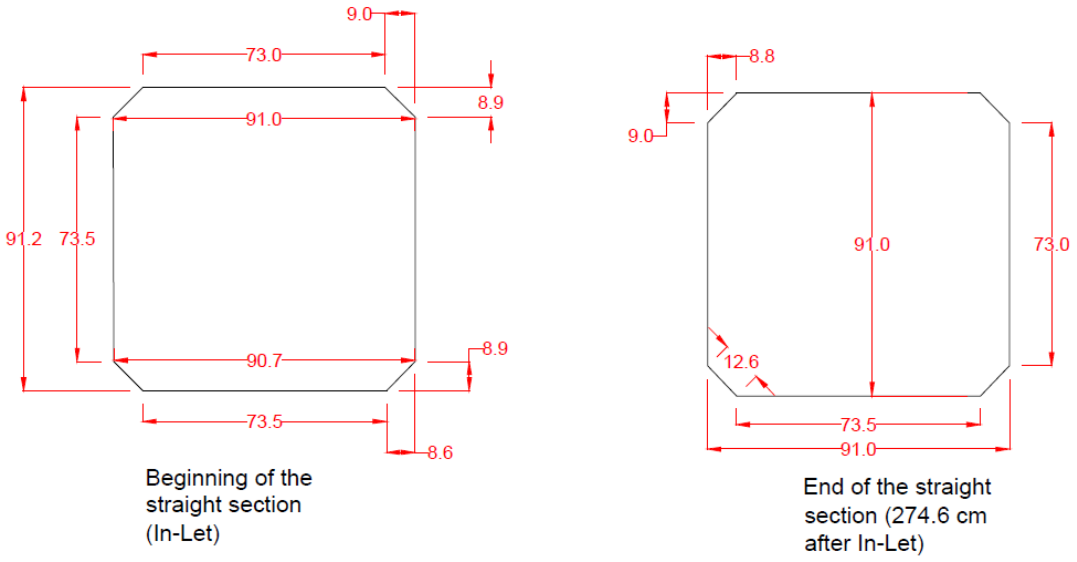

Figure 4-2: Wind tunnel cross-section at test section

4.3.2 Test Set-Up Description and Measuring Tools

The technique used here is the free vibration one using a specific setting that was designed, built, and installed. The setting consists of a rigid frame at both ends of the model, each frame being fixed to the tunnel wall. The model was fixed to a rigid arm (truss) at each end and the arm sits on four springs, two at each end, making a total of eight springs in the system (Figure 4-3 (b)). The arm length and the distance between the springs was chosen to ensure minor rotational motion (high torsional rigidity). The longitudinal motion was restrained using laminar steel plates (black bar in Figure 4-3(b)) that is connected to the frame and the arm at the same time, where it carries the longitudinal load in tension hindering the model motion in the along wind direction. All the system (frame, arm, and springs) was covered with clear plastic sheet to assure that the flow is smooth.

Two pitot tubes were placed underneath the model for the mean velocity measurement. As for the force measurement, four tension load cells were installed under the springs, two at each end of the model. Before carrying any testing, the load cells were calibrated, and a load factor was determined to convert the load in volts to forces in N, set up for torque calibration is shown Figure 4-3(a).

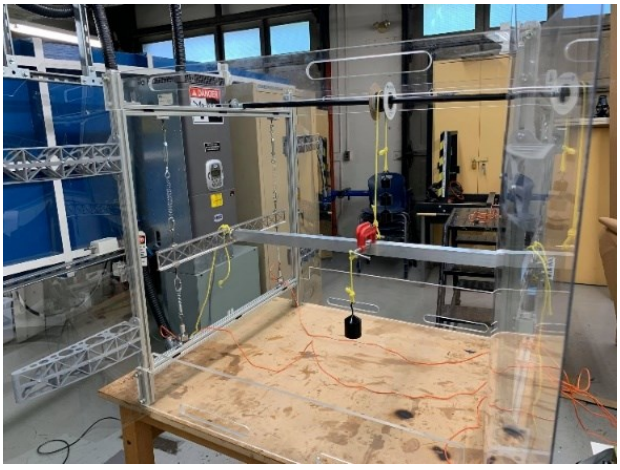

(a)

(b)

(c)

Figure 4-3: (a) Static test setup for square cylinder (b) Side view of setup for square cylinder (c) Wind Tunnel setup for four-panel truss

4.4 Testing Procedures and Validation

In this section the steps followed in the testing are explained, knowing that the procedures pursued in the wind tunnel test remained consistent along all the tests for the three models (Figure 4-4). Though the free vibrations method is not commonly used in literature for strongly bluff bodies, the technique is well known and used for streamlined bodies [101, 108-110].

The cylinder was allowed to freely vibrate in an attempt to estimate the flutter derivative H_1^*. The model was allowed to move only in the cross-stream direction, while the motion was restricted in the stream-wise and rotational directions.

(a) (b)

Figure 4-4: (a) Angle test specimen (b) four-panel truss specimen

4.4.1 Procedures

4.4.1.1 Dynamic Properties

At first the dynamic properties of the system with the model in place were determined through static load tests, using equation 4-4 the corresponding system mass (m) and stiffness (k) were determined. The static load test was done by adding a definite mass, then giving slight pushes at constant time intervals to the model while recording the vibrations. The previous steps were repeated while increasing masses and then again while unloading masses. The frequency was calculated for each added mass, and values for the square of the circular frequency were plotted

against the square of the circular frequency multiplied by the added mass. Fitting of the values is shown in Figure 4-5, where the mass and stiffness of the system were calculated from the fit.

$$\omega_n = \sqrt{\frac{k}{m}} \qquad 4\text{-}4$$

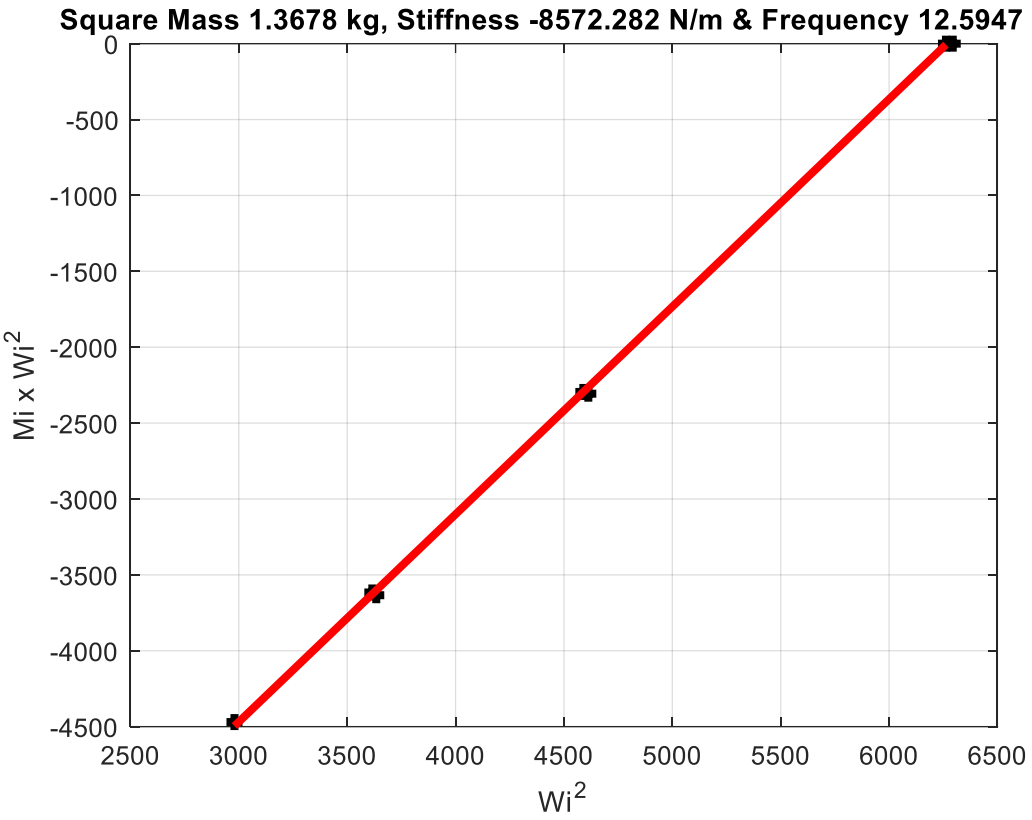

Figure 4-5 Square cylinder dynamic lift calibration

4.4.1.2 Structural Damping

Then the system structural damping (ζ) was determined through free vibration tests. The model was given an initial push then left to vibrate freely. The logarithmic decrement method, equation 4-5, was used to calculate the structural damping through curve fitting of the peaks of the time history of the vibrations.

$$\delta = \frac{2\pi\zeta_t}{\sqrt{1-\zeta_t^2}} = \frac{1}{j}\ln\left(\frac{y_i}{y_{i+1}}\right) \qquad 4\text{-}5$$

4.4.1.3 Testing Procedures

In the free vibration test the model was pulled to an initial displacement then released to vibrate over the springs. This step was repeated during a recording cycle. The data acquisition lasted for a total duration of 2 minutes at a frequency of 512 Hz. During this process the forces were recorded from load cells and then displacements were calculated (displacement = Force/stiffness). The experiments were run at a Reynolds number of $6.4\text{x}10^3$ to $115\text{x}10^3$.

4.4.2 Validation

In this part, the literature available for determining the flutter derivative for the section models under consideration was mostly for the square cross-section. Consequently, the next section will be dedicated to the validation of the square cylinder model.

4.4.2.1 Square Cross Section Model

A rigid hollow aluminum square cylinder of dimension D_s = 7.55 cm and length L_s = 77 cm was used. The square had sharp edges and a smooth surface. The mass was found to be m_s = 1.37 kg, stiffness k_s = 8572 N/m and the structural damping ratio ζ_s = 0.3%. The natural frequency F_{ns}= 12.59 Hz.

4.4.2.2 Flutter Derivative Determination

As mentioned earlier, the free vibration method was adopted to extract the aerodynamic flutter derivatives. The simulations were carried out at a reduced velocity range from 4 to 20. The time history was first filtered using a low pass filter to avoid contamination from the beating. Then total damping ζ was calculated through fitting the peaks of each signal into an exponential curve whose slope represents the damping ratio. The first few cycles of motion just after the push were the only ones fitted as this is the part of interest since after that the structure would be vibrating freely under structural damping. Figure 4-6 shows three signals of the time history of non-dimensional displacements recorded at a reduced velocity U_{red} = V/(F_n*D) = 7.8,

where V is the wind velocity inside the tunnel, F_n is the natural frequency $F_n = \omega_n/2\pi$, and D is the characteristic length. The total damping ζ was calculated for each signal in Figure 4-6, where each signal represents the system response following the push. The average of the damping ratio from the signals is considered the total system damping ζ. Figure 4-7 shows the peaks of vibration normalized by the peak amplitude for each signal versus time. For the specific case at U_{red}= 7.8 indicated in the figures the average total damping ratio was found to be 2.9% with a standard deviation of 0.2%. Another example of the fit was added as shown in Figure 4-8 and Figure 4-9. The analysis showed that the frequency did not change therefore the aerodynamic instability was negligible (H_4^*).

The aerodynamic damping (ζ_a) was calculated from the difference between the total and structural damping (ζ_s). Using the aerodynamic damping, the aerodynamic derivative H_1^* was calculated from equation 4-6 [98-101].

$$H_1^* = \frac{-4\,\zeta_a\, m}{\rho\, D^2} \qquad 4\text{-}6$$

Where, m : mass of the body per unit length, ρ: density of air, D: stream-wise dimension.

The aerodynamic derivative H_1^* was compared against wind tunnel test results by Matsumoto 2006 and Yagi 2013 showing fairly good agreement as shown in Figure 4-10 [72, 78]. Since aerodynamic damping is an average of four pushes to the structure, it was important to investigate the variation of the aerodynamic derivative H_1^*. As seen in Figure 4-10, the red and blue + signs represent H_{1max}^* and H_{1min}^* respectively, the variation ranged between 2-10% which is acceptable. In literature experiments were conducted for a square cylinder forced to vibrate in the cross-stream direction with different prescribed vibration amplitudes, Y/D = 0.0125, 0.05, 0.1 and 0.15, where Y is the forced displacement amplitude and D is the square dimension.

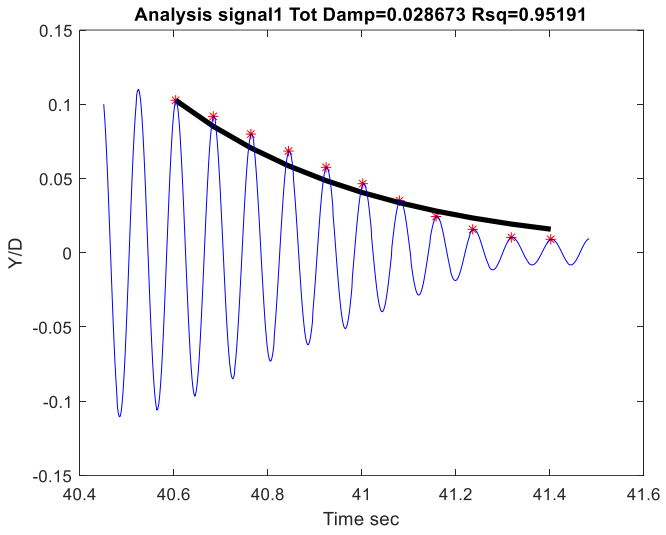

(a)

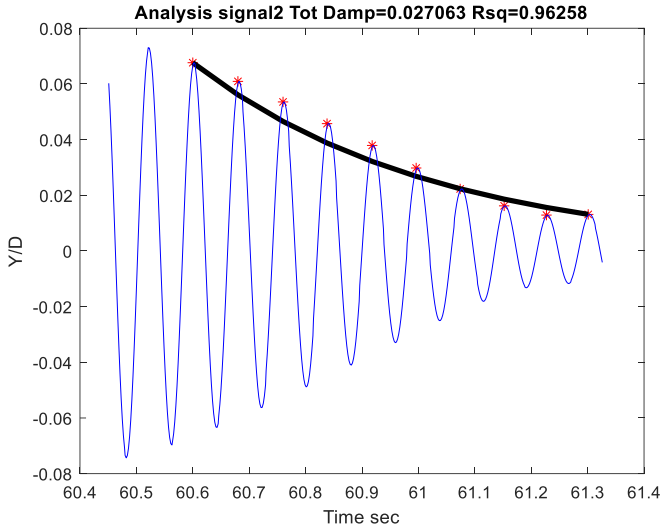

(b)

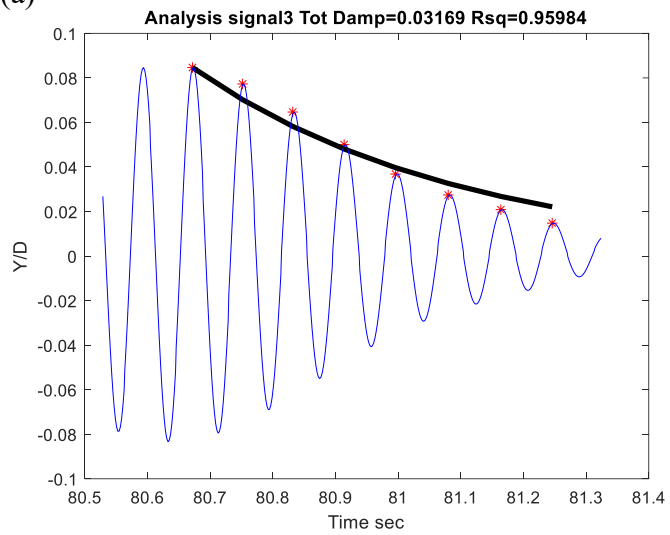

(c)

Figure 4-6: Time history of vibrations after an initial push for the square cylinder at U_{red} = 7.8 (a) Signal 1 (b) Signal 2 (c) Signal 3

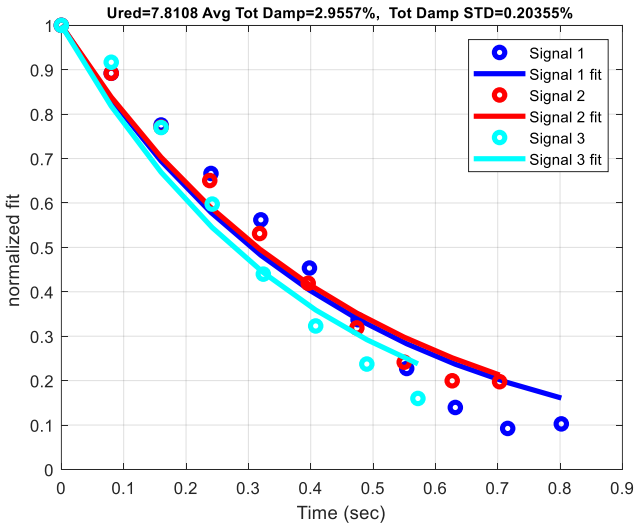

Figure 4-7: Normalized fit for the analyzed signals at U_{red} = 7.8

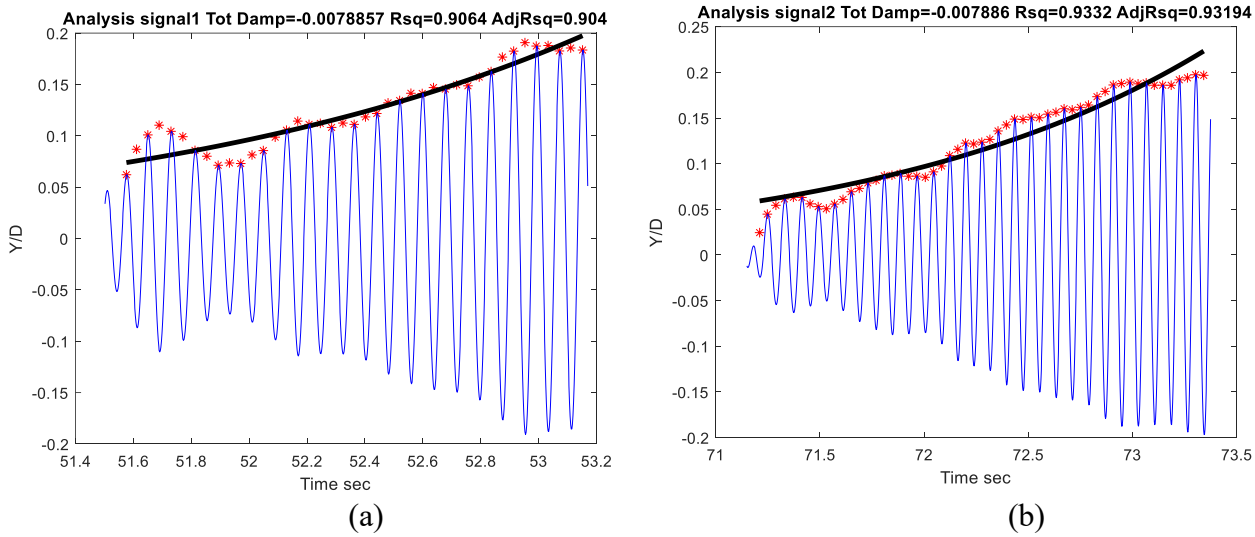

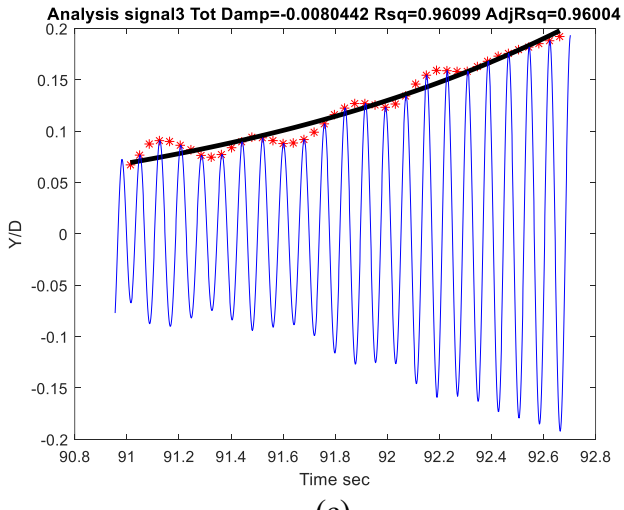

Figure 4-8: Time history of vibrations after an initial push for the square cylinder at U_{red} = 8.5 (a) Signal 1 (b) Signal 2 (c) Signal 3

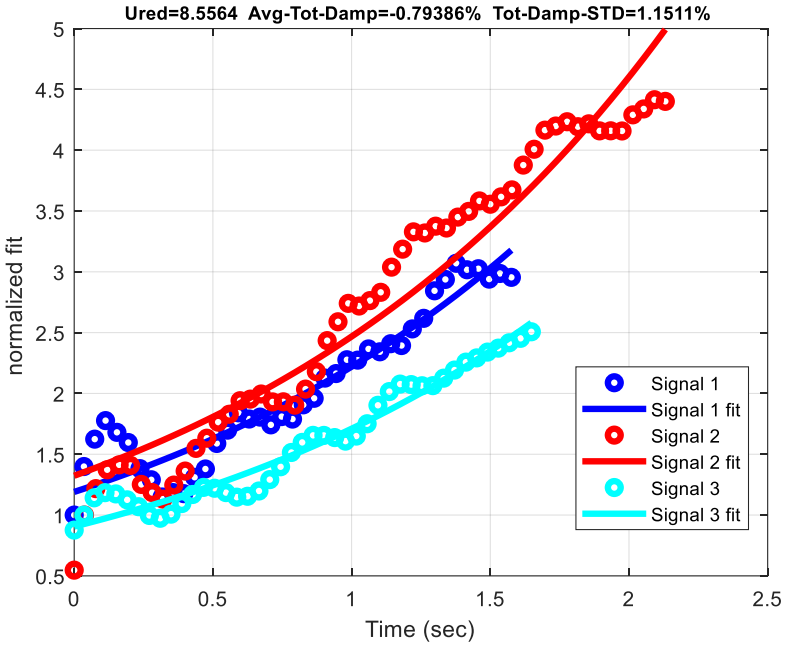

Figure 4-9: Normalized fit for the analyzed signals at U_{red} = 8.55

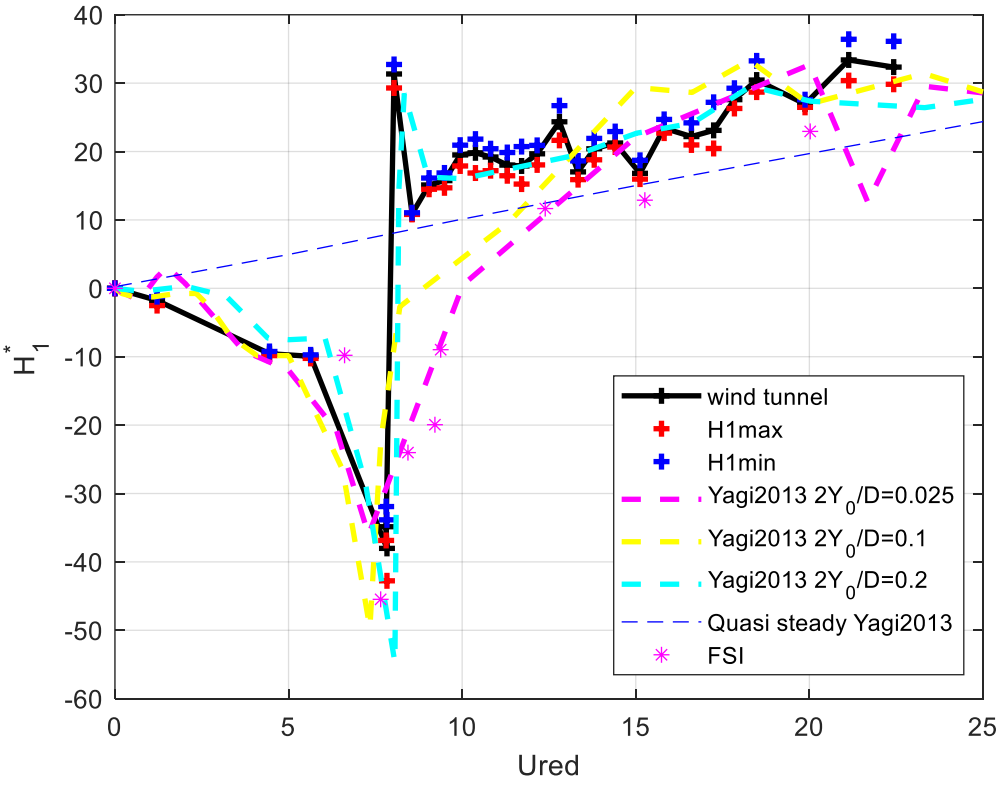

Figure 4-10: H_1^* aerodynamic derivative versus reduced velocity (U_{red})

4.5 Determining The Flutter Derivative H_1^* For the Angle Shape and Truss Panel

In this section the same method, which was proved valid, was used to find the flutter derivative for two section models that were not studied before in the literature.

4.5.1 Angle Shape

An equal legged angle shaped member made of aluminum was used with a dimension D_a = 5.5 cm and length L_a = 75 cm. The system measured mass was m_a = 1.2 kg, while the stiffness was k_a = 7906 N/m, these yield a natural frequency of F_{na} = 12.9 Hz. The measured structural damping was ζ_{sa} = 0.64%. The angle cross-section was tested at 2 angles of attack 45° and 135° measured as shown in Figure 4-11.

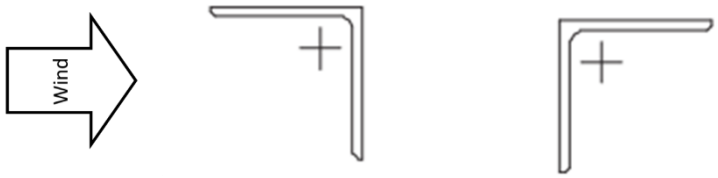

Figure 4-11: Different incident flow orientations for the Angle shape

The aerodynamic derivative H_1^* was found following the same free vibration procedures used for the square cylinder. H_1^* is plotted against the reduced velocity U_{red} in Figure 4-12, where the variations were in an acceptable margin of 2-12%.

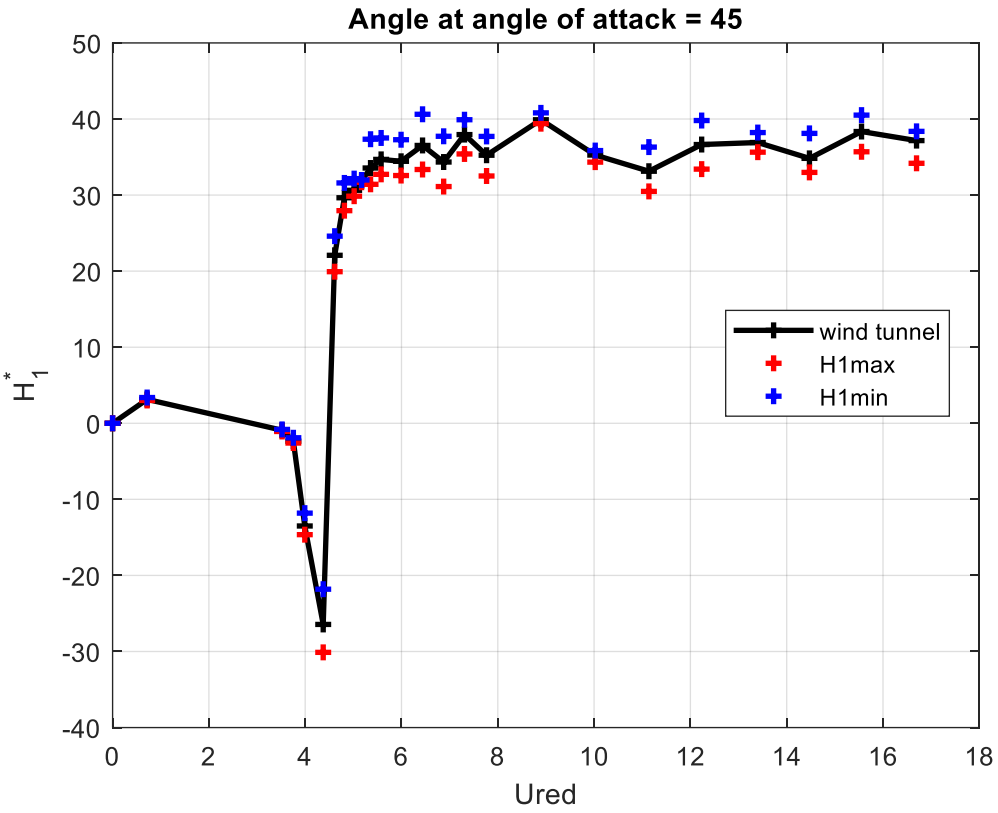

Figure 4-12: H_1^* aerodynamic derivative versus reduced velocity (U_{red})

4.5.1.1 Validation

To further validate the H_1^* derivative and due to lack of similar results in literature, the H_1^* found from the wind tunnel tests was used to back calculate the normalized rms for the amplitude of vibration and then results were compared to literature. Firstly, CFD simulations for the angle shape were carried on implementing the same method and procedures adopted in the square cylinder (chapter 3). Then the normalized rms for the amplitude of vibration was found by coupling the aerodynamic forces from computational fluid dynamics (CFD) simulations along with the aerodynamic damping ζ_{aa} from wind tunnel test for the equal angle cross-section. Both methods are explained below.

4.5.1.1.1 CFD Simulations for Angle Cross Section

The same parameters and mesh used for the square cylinder, were used for the angle cross-section cylinder. The angle cross-section member was tested under angles of attack 0-180 as

seen in Figure 4-13. The model dimensions are shown in Figure 4-14 and the mesh is shown in Figure 4-15. Figure 4-16 and Figure 4-17 represent the mean drag coefficient $C_{\mathrm{D}_{\mathrm{mean}}}$ and the rms of the lift coefficient $C_{L_{rms}}$ versus the angle of attack, respectively, where it shows reasonably good validation with the literature.

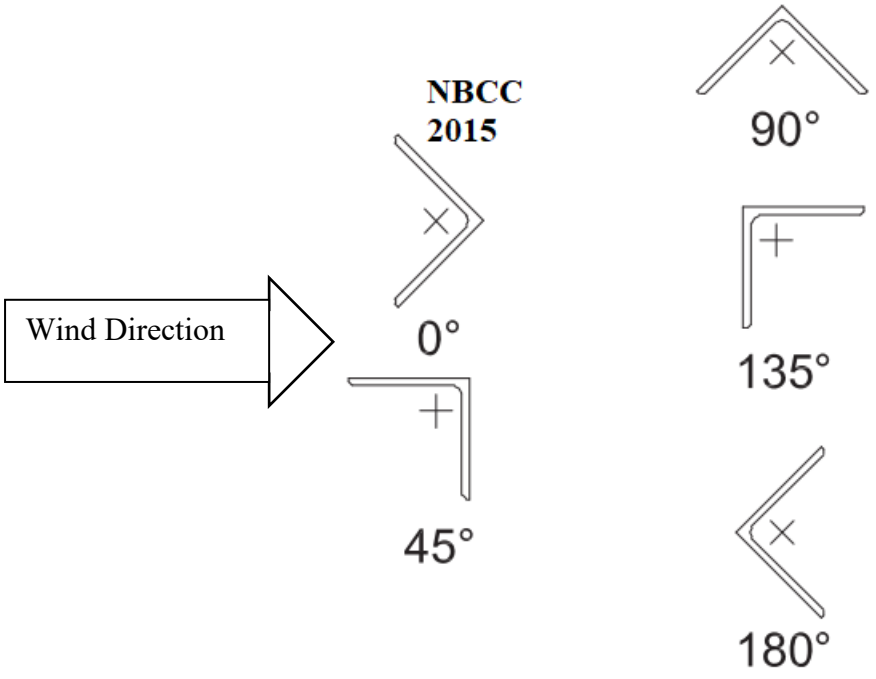

Figure 4-13 Angle orientations tested

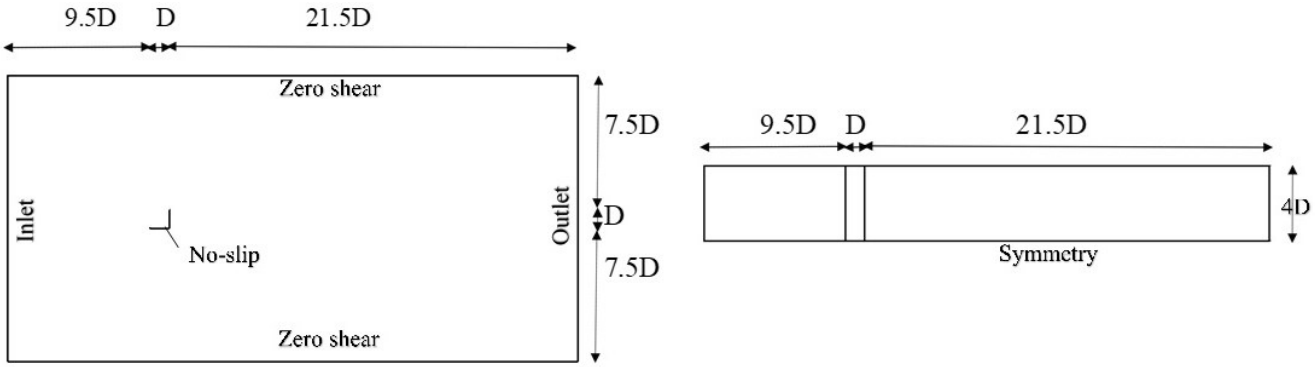

Figure 4-14 Dimensions of the CFD model

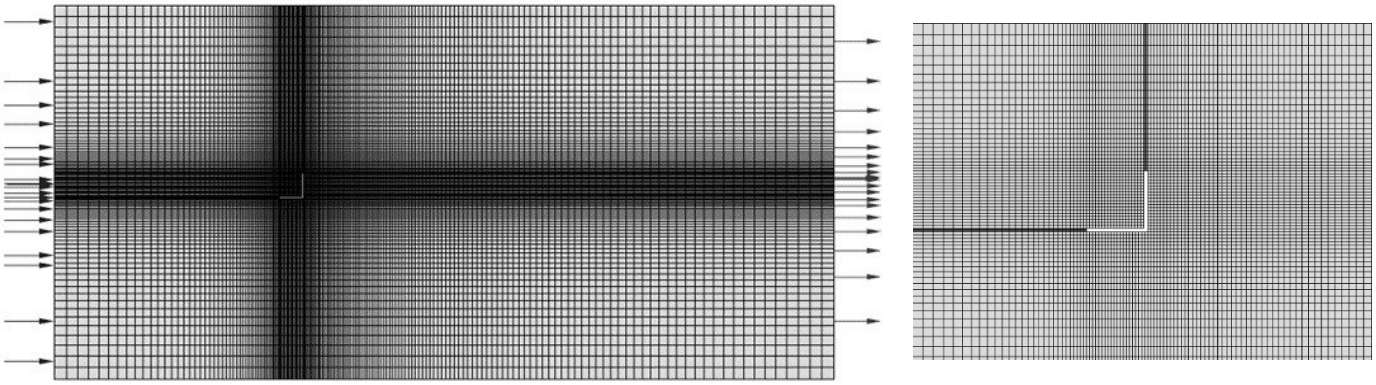

Figure 4-15 Mesh chosen and a close-up

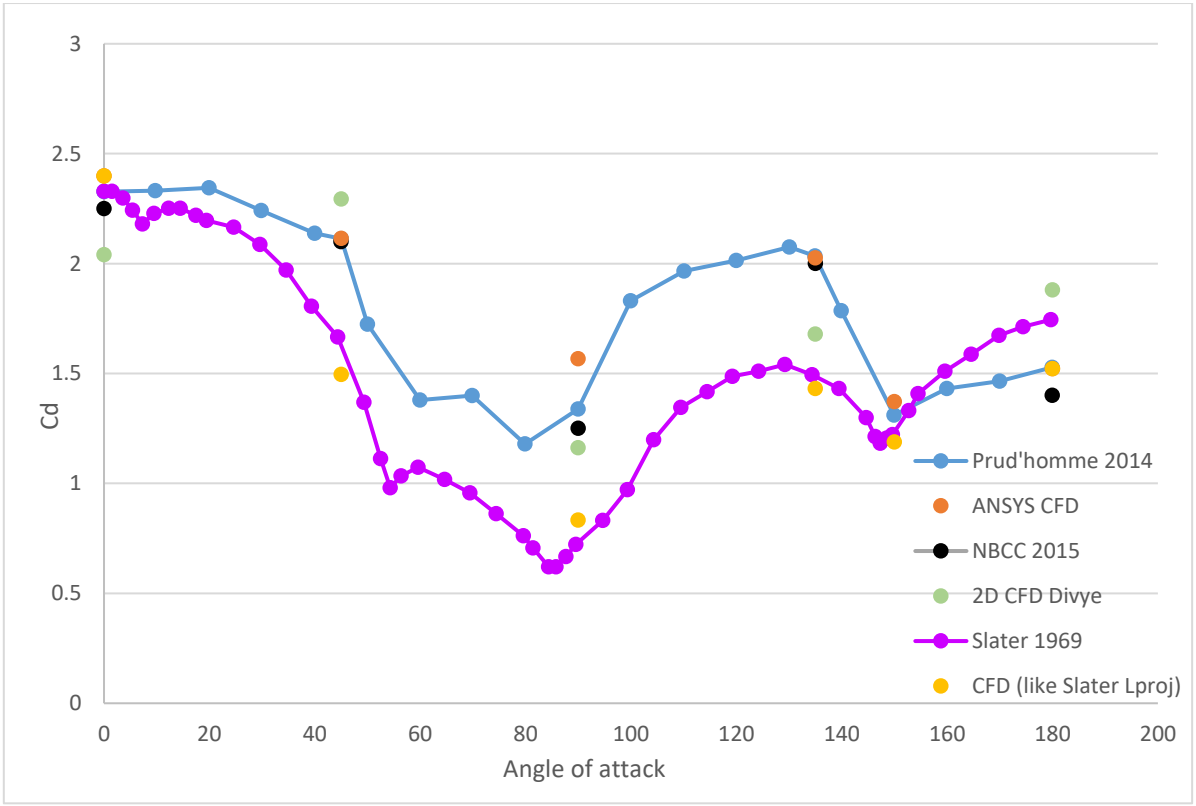

Figure 4-16 $C_{D_{mean}}$ versus angle of attack

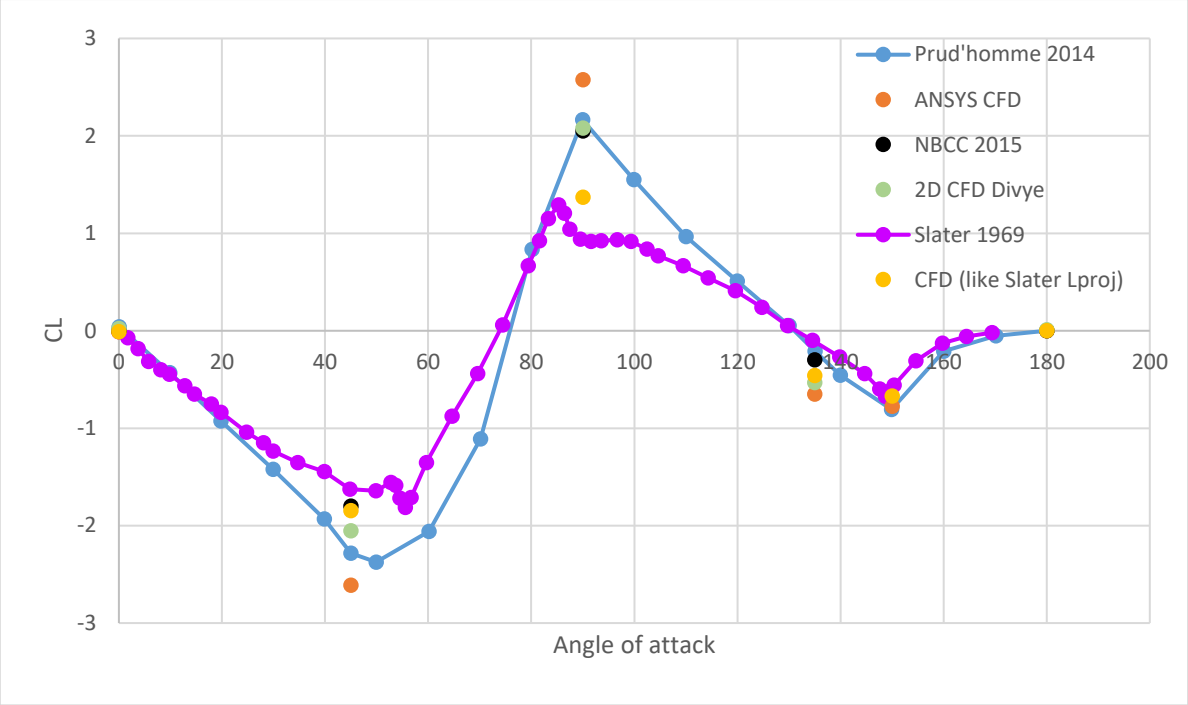

Figure 4-17 $C_{L_{rms}}$ versus angle of attack

4.5.1.1.2 Determination of RMS Vibrations

In this part, firstly the normalized spectrum for the angle shape was found with the knowledge of the aerodynamic force from the CFD simulation. Then, the aerodynamic damping ζ_{aa} was calculated using equation 4-6 utilizing the same parameters (mass, length and characteristic dimension) as in the free vibration wind tunnel test by Slater [8]. The total damping ζ is the summation of structural damping ζ_{sa} and aerodynamic damping ζ_{aa}. Following that, the data was analyzed using frequency domain and random vibration theory to determine Y_{rms} using equations 4-7, 4-8 and 4-9. Figure 4-18 shows good agreement between the method used and the measurements reported by Slater 1969.

$$Y_{bg} = \frac{P_{rms}}{K} \qquad 4\text{-}7$$

$$Y_{res} = \frac{P_{rms}}{K}\sqrt{\frac{\pi}{4\zeta}\frac{F_n S_f}{P_{rms}^2}} \qquad 4\text{-}8$$

$$Y_{rms} = \sqrt{Y_{bg}^2 + Y_{rms}^2} \quad \text{4-9}$$

Where, Y_{bg}: background component (m), P_{rms}: rms of the aerodynamic force (N), K: system stiffness (N/m), Y_{res}: resonant component (m), ζ: total damping, F_n: system natural frequency (Hz), S_f: aerodynamic force spectra N^2/Hz and Y_{rms}: rms displacement. The flow chart shows the steps that were followed to find the rms vibrations Figure 4-19.

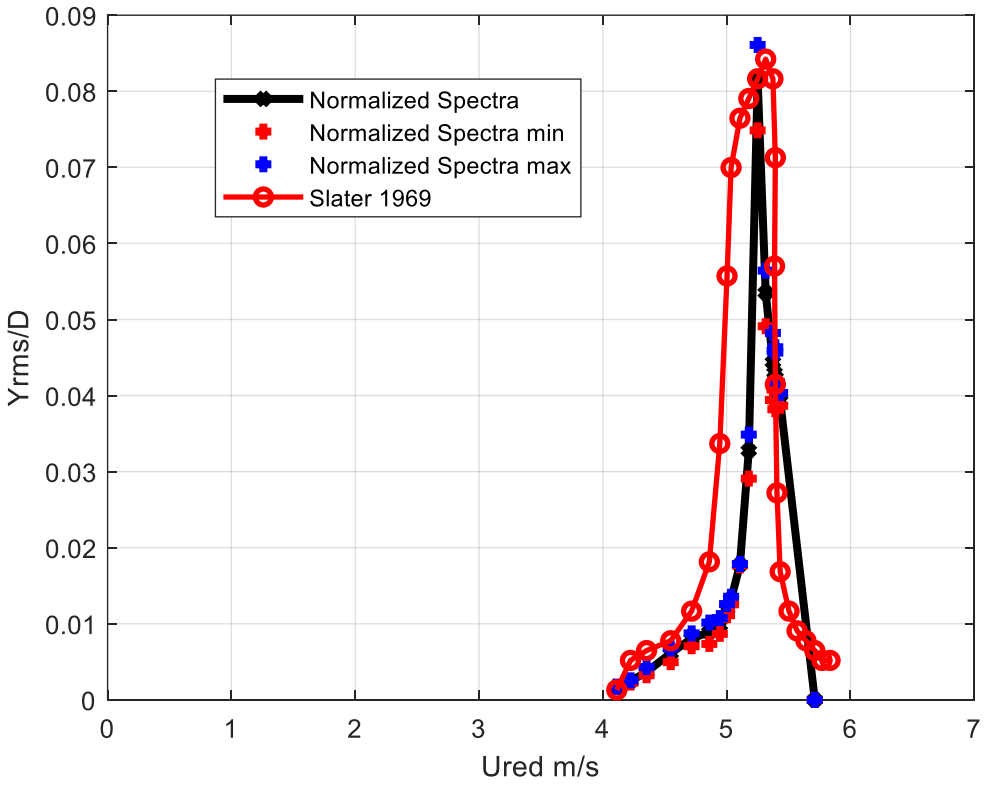

Figure 4-18: Normalized rms displacement (Y_{rms}) versus U_{red}

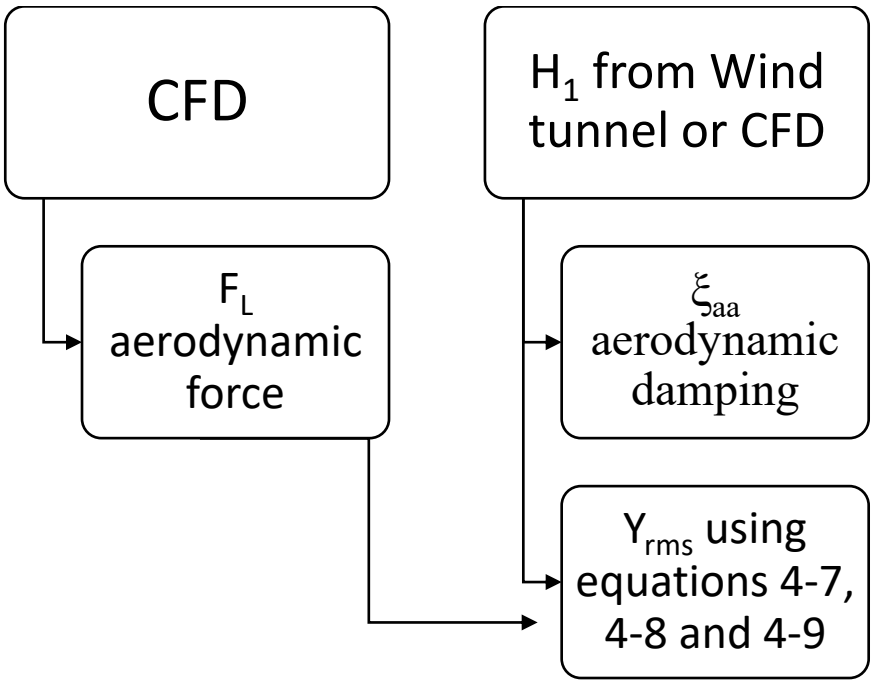

Figure 4-19: Flow chart showing the procedures followed to find Y_{rms}

The aerodynamic derivative H_1^* for the other angle of attack 135° was extracted in the same manner as for the square and the 45° angle of attack. Figure 4-20 shows the calculated H_1^* versus the reduced velocity U_{red} at an angle of attack 135° with the observed variation falling within an acceptable range of 1-11%. From these figures it is clear that the equal legged angle at angles of attack 45° and 135° is prone to vortex shedding at around a resonance velocity U_{res} = 1/St. On the other hand, while no clear galloping instability occurred in the range of velocities studied for the angle of attack 45°, galloping instability is monitored for the angle of attack 135°. The resemblance between the H_1^* aerodynamic derivative for the square and the angle at angle of attack 135° was expected as they have similar geometry in the leeward, and that is an extra validation for the angle at angle of attack 135°.

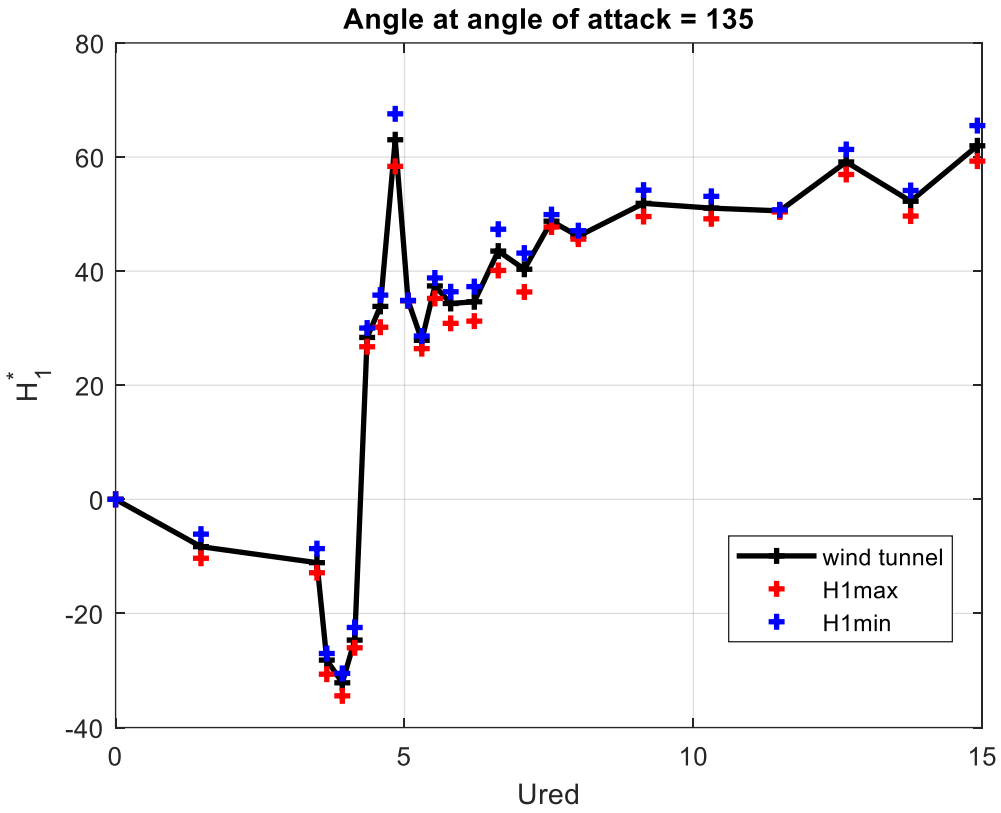

Figure 4-20: H_1^* versus U_{red} at angle of attack 135°

4.5.2 Lattice Structure

The final part of this study is to evaluate the aerodynamic derivative H_1^* on a part of a structure instead of just an element. A W Truss shape with a square cross-section was tested in the wind tunnel of Toronto Metropolitan University (Figure 4-21). The truss chords, verticals and diagonals were made of square cross-section. The truss had a span of 78 cm and total depth of 19.3 cm and comprised four equal span panels. The system measured mass was m_t = 2.14 kg, while the stiffness was k_t = 8754 N/m these yield a natural frequency of F_{nt} = 10.18 Hz. The measured structural damping was ζ_{st} = 0.6%. The model was tested for a range of reduced velocity U_{red}= 4-12, for a Reynolds number that varies from 40x10^3 to 327x10^3 calculated based on the total depth (D). The truss was tested for two different solidity ratios (SR) through changing the depth of the chords by attaching a very light angle shape rod to the upper and

lower chords, as seen in Figure 4-22(a), also through changing the width of the verticals, see Figure 4-22(b). The two tested solidity ratios are 0.23 and 0.34.

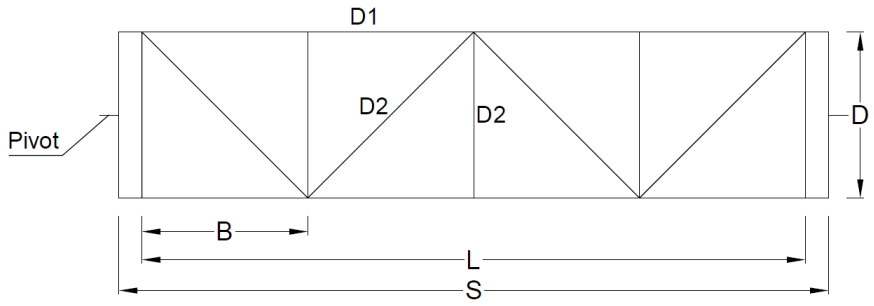

Figure 4-21: Truss with four panels

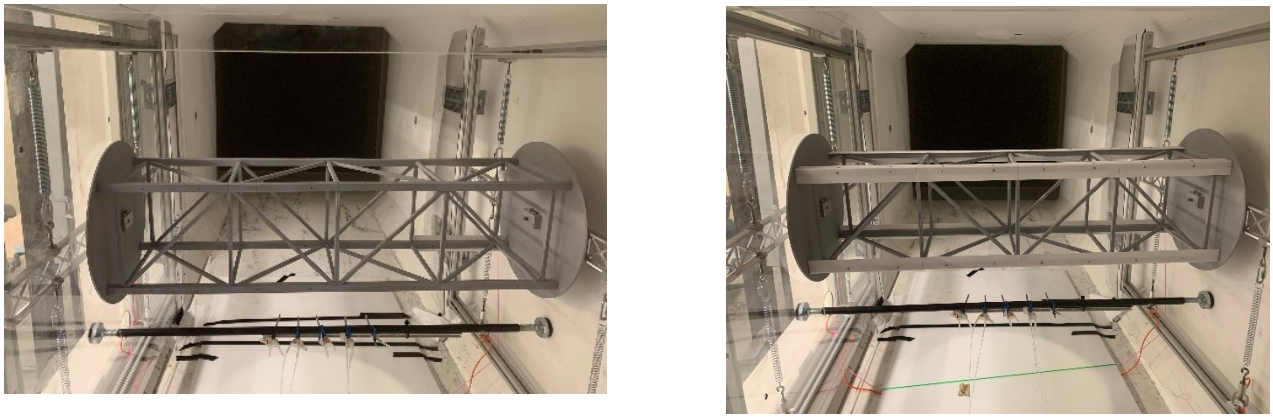

(a) (b)

Figure 4-22: Truss with different solidity ratios (SR) (a) SR = 0.23 (b) SR = 0.34

The truss was tested following the same procedures as the square and equal legged angle cross-sections. The aerodynamic derivative H_1^* versus the reduced velocities for the two solidity ratios were plotted in Figure 4-23 and Figure 4-24. The observed variations in the aerodynamic derivative H_1^* fell within an acceptable range of 2-13% for SR = 0.23 and 3-15% for SR = 0.34. From Figure 4-23 and Figure 4-24, it can be concluded that for the truss studied, vortex induced vibrations (VIV) were observed at $U_{red}\approx$ 5.5 where maximum displacement took place while, no galloping occurred up to the maximum velocity tested. Figure 4-25 shows the comparison between SR = 0.23 and SR =0.34 where, it was seen that the lower solidity case experienced higher magnitudes of the aerodynamic derivative H_1^* and hence higher positive aerodynamic

damping (Figure 4-25). This suggests that an increase in the solidity ratio could lead to higher negative aerodynamic damping, consequently causing vibrations to grow higher.

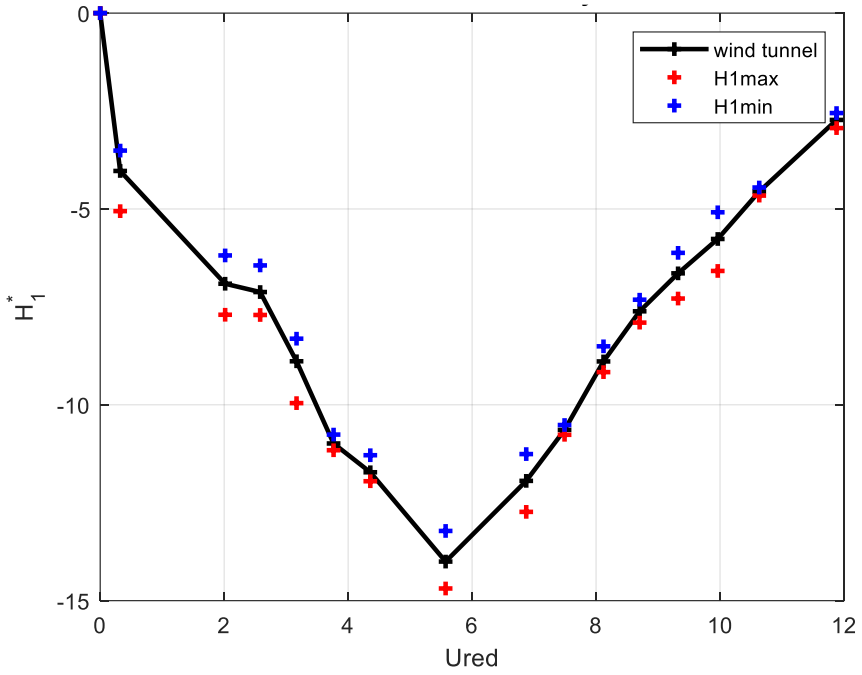

Figure 4-23: Truss with solidity ratio = 0.23

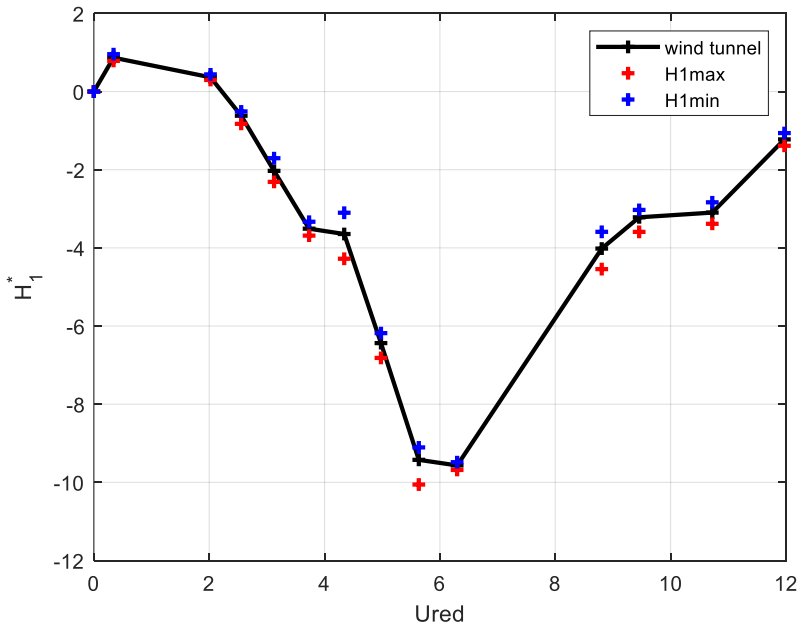

Figure 4-24: Truss with solidity ratio = 0.34

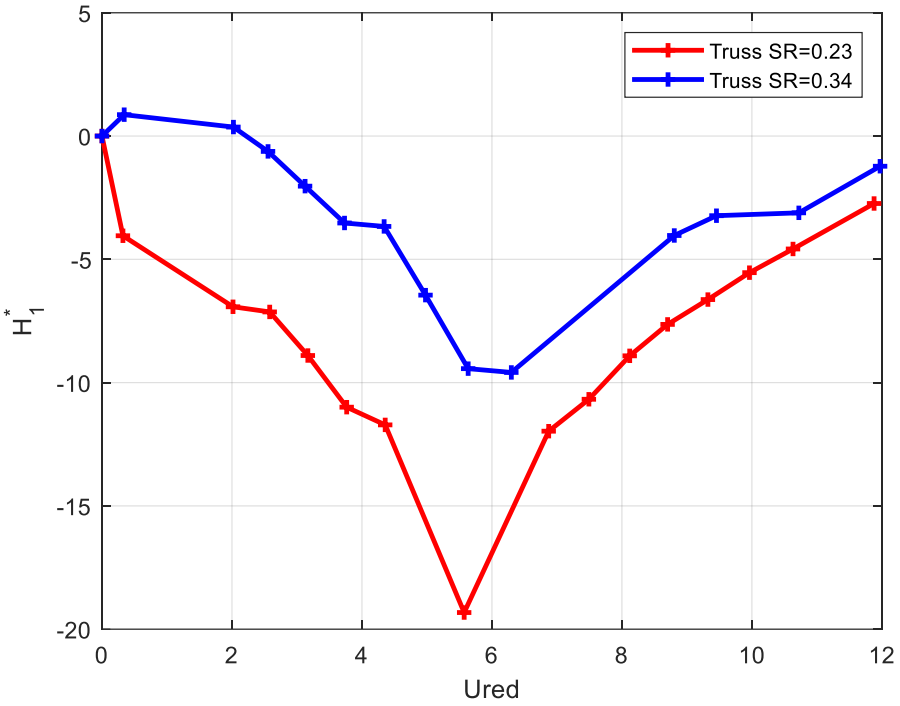

Figure 4-25: H_1^* versus U_{red} for the truss panel

4.6 Conclusion

In this study, wind tunnel tests were carried out for two structural elements (square and angle cross-sections) and a part of lattice structure in order to determine their aerodynamic derivative H_1^* through a free vibration technique. First, the aerodynamic derivative H_1^* was determined and validated for the square cylinder as it was the most commonly available in literature among other models under investigation. Then, the results for the angle shape at an angle of attack 45° was also validated through coupling the aerodynamic damping from H_1^* with aerodynamic forces obtained from computational fluid dynamic simulations. This method provides the rms vibrations at different velocities, which opens the door for studying fluid-structure interaction for the same cross-section with different structural dynamic parameters and consequently, predict the response of the freely vibrating model to wind flow. After that, H_1^* was determined for the angle shape at angle of attack 135°. Finally, a four-panel lattice structure was tested under different solidity ratios and a data base of H_1^* aerodynamic derivatives was accumulated.

The following conclusions can be deduced from analyzing the results obtained from the wind tunnel tests.

- The free vibrations method carried in the wind tunnel proved to be a reliable tool in the derivation of the aerodynamic derivative H_1^* for single degree of freedom strongly bluff bodies and systems.
- The method used to estimate the rms vibrations with the knowledge of the aerodynamic derivative H_1^* was valid, and it yielded comparable results. This allows for integrating this method in the early design stages.
- A library for H_1^* derivative was built for the W- shaped truss.

These outputs provide essential inputs to study the dynamic response of an example of lattice structure to study fluid structure interaction in exposed structures. This will be done in the subsequent chapter to demonstrate the feasibility of the proposed methodology.

4.7 Acknowledgement

The authors would like to acknowledge the support of the National Science and Engineering Research Council of Canada for its financial support.

REFERENCES

1. Yagi, T., et al., *Interferences of vortex sheddings in galloping instability of rectangular cylinders.* Kozo Kogaku Ronbunshu. A (Journal of Structural Engineering. A), 2013. **59A**: p. 552-561.
2. M. Matsumoto, T.Y., J. H. Lee, K. Hori, Y. Kawashima, *Karman vortex effect on the aerodynamic forces to rectangular cylinders*. Vol. 9. 2006.
3. Scanlan, R.H. and J. Tomo, *Air foil and bridge deck flutter derivatives.* Journal of Soil Mechanics & Foundations Div, 1971.
4. Šarkić, A., et al., *Bridge flutter derivatives based on computed, validated pressure fields.* Journal of Wind Engineering and Industrial Aerodynamics, 2012. **104-106**: p. 141-151.
5. Sarkar, P.P., N.P. Jones, and R.H. Scanlan, *Identification of aeroelastic parameters of flexible bridges.* Journal of Engineering Mechanics, 1994. **120**(8): p. 1718-1742.
6. Larsen, A. and J.H. Walther, *Discrete vortex simulation of flow around five generic bridge deck sections.* Journal of Wind Engineering and Industrial Aerodynamics, 1998. **77-78**: p. 591-602.
7. Tamura, K.S.T.I.a.Y., *Prediction of aeroelastic characteristics of rectangular cross-sections by k-w model.* Structures 2004: Building on the Past, Securing the Future, 2004.
8. Scanlan, R., *Motion-related body-force functions in two-dimensional low-speed flow.* Journal of Fluids and Structures, 2000. **14**(1): p. 49-63.
9. Xu, F. and Z. Zhang, *Free vibration numerical simulation technique for extracting flutter derivatives of bridge decks.* Journal of Wind Engineering and Industrial Aerodynamics, 2017. **170**: p. 226-237.
10. Bouris, D. and G. Bergeles, *2D LES of vortex shedding from a square cylinder.* Journal of Wind Engineering and Industrial Aerodynamics, 1999. **80**(1): p. 31-46.

11. Cao, B. and P.P. Sarkar, *Identification of rational functions using two-degree-of-freedom model by forced vibration method*. Engineering Structures, 2012. **43**: p. 21-30.

12. Matsumoto, M., Y. Kobayashi, and H. Shirato, *The influence of aerodynamic derivatives on flutter.* Journal of Wind Engineering and Industrial Aerodynamics, 1996. **60**: p. 227-239.

13. Brar, P.S., R. Raul, and R.H. Scanlan, *Numerical calculation of flutter derivatives via indicial functions.* Journal of Fluids and Structures, 1996. **10**(4): p. 337-351.

14. Matsumoto, M., *Aerodynamic damping of prisms.* Journal of Wind Engineering and Industrial Aerodynamics, 1996. **59**(2): p. 159-175.

15. Mannini, C., *Applicability of URANS and DES simulations of flow past rectangular cylinders and bridge sections*. Computation, 2015. **3**(3): p. 479.

16. Gao, G. and L. Zhu, *Measurement and verification of unsteady galloping force on a rectangular 2:1 cylinder.* Journal of Wind Engineering and Industrial Aerodynamics, 2016. **157**(Supplement C): p. 76-94.

17. Slater, J.E., *Aeroelastic instability of a structural angle section*. 1969, University of British Columbia.

18. Ghazal, T., et al., *Flow-conditioning of a subsonic wind tunnel to model boundary layer flows*. Wind and Structures, 2020. **30**(4): p. 339-366.

19. Aboshosha, H., L. Kong, and J.P.C. King, *Pensacola Bay bridge replacement, sup tied arch bridge, Pensacola/Gulf Breeze, Florida*. 2017, Alan G. Davenport Wind Engineering Group.

20. Král, R., S. Pospíšil, and J. Náprstek, *Wind tunnel experiments on unstable self-excited vibration of sectional girders.* Journal of Fluids and Structures, 2014. **44**: p. 235-250.

21. Partha P. Sarkar, L.C., Frederick L. Haan, Hiroshi Sato, Jun Murakoshi, *Comparative and sensitivity study of flutter derivatives of selected bridge deck sections, Part 1:*

Analysis of inter-laboratory experimental data. Engineering Structures, 2009. **31**(1): p. 158-169.

22. Bartoli, G. and M. Righi, *Flutter mechanism for rectangular prisms in smooth and turbulent flow.* Journal of Wind Engineering and Industrial Aerodynamics, 2006. **94**(5): p. 275-291.

BRIDGING BETWEEN CHAPTERS FOUR AND FIVE

Chapter 4 was dedicated to describing the wind tunnel test set up, procedures and validation of the square cylinder, followed by the extraction of the aerodynamic derivative H_1^* for the equal legged angle cross section member at two angles of attack 45^o and 135^o. Finally, the determination of the flutter derivative H_1^* for a four-panel truss at two different solidity ratios was achieved. The extracted derivatives are used in Chapter 5 to determine the aerodynamic damping.

The primary objective of this study is to investigate how the flexibility of a lattice structure influences the wind loads exerted on it, and this is what Chapter 5 is about. To study the problem under investigation there are three requirements. First, the aerodynamic coefficients of the lattice structure which were obtained through CFD simulations. Second, the aerodynamic derivative H_1^* of the lattice structure which was estimated in Chapter 5. Last, is the development of a procedure for the quantification of the response and consequently the actual forces acting on a square cylinder and the flexible lattice structure, which was done through time history analysis of structural dynamic model in commercial software SAP2000 V20.2.0.

Chapter 5 illustrates the proposed methodology and validates it where the feasibility of the study is demonstrated by applying it to an example of a structural element and an exposed structure. The chapter also provides conclusions on the impact of studying the fluid-structure interactions on wind flow. It first discusses the procedures followed to extract structural damping for the structural models under study. Then, it describes the steps to calculate the aerodynamic damping for the modes of vibration of the structural models under consideration using the aerodynamic damping estimated from the measurements in the wind tunnel. Finally, it holds a comparison for the response of the structural models investigated (i.e., a square

cylinder and a lattice structure) with and without taking the fluid structure interactions into consideration.

CHAPTER 5 EXPLORING WIND-STRUCTURE INTERACTIONS ON FLEXIBLY-SUPPORTED TRUSS MEMBERS AND LATTICE 3-D PANELS USING AERODYNAMIC DERIVATIVES

5.1 Abstract

This chapter demonstrates the applicability of the proposed methodology. It presents a study to determine the effect of flexibility of structural members and flexible lattice structures on loads/responses through wind tunnel experiments, computational fluid dynamics (CFD) and dynamic numerical analysis. Three models were tested, which are elements and parts of lattice structures: a cylinder with square cross-section, a member with equal legs angle cross-section and a segment of a three-dimensional lattice structure with four equal-width panels. The models were supported on springs and allowed to move in the cross-stream direction only. The value of aerodynamic damping was extracted from the displacement time histories for several wind speeds and hence the aerodynamic derivative H_1^* was calculated. Following that, a finite element model for a lattice structure composed of the studied models was created to assess whether taking the structural flexibility into account would affect the wind loading and structural response or not. This was done through comparing the responses with and without the effect of aerodynamic damping. The overall aerodynamic damping of the entire structure was determined by evaluating it for various mode shapes. This evaluation relied on the aerodynamic derivatives of the structural members that constitute the complete structure. This comparison has been experimentally studied in the literature [12, 14, 52, 55-57, 59, 60, 102, 111, 112] but for only square or rectangular cross-sections, while in this study, it will be extended to a three-dimensional lattice structure. The results show that taking the structure flexibility into consideration when determining wind loads is important as the fluid-structure

interactions have a noticeable effect on the loads/response. The square cylinder was tested at ten distinct velocities where the response was magnified at some velocities while attenuated at others. An amplifying effect on the response was seen to reach a maximum of up to 70% at the vortex induced vibrations while an increase in the range of 10-50% was observed at higher velocities. On the other hand, vibrations decreased 10-50% at velocities lower than the velocity at which vortex induced vibrations started. The lattice structure was tested at ten different velocities where vortex-induced vibrations were always suppressed. The decrease in displacement response reached a maximum of around 30-60% around reduced velocities of 4 to 7 while the least reductions in the range of 3-30% were encountered at the highest velocities tested.

5.2 Introduction

The forces on bluff bodies and structures exposed to wind are complex to determine and depend on many variables including shape of the object, wind direction, and wind velocity profile. For instance, slender exposed structures such as signage cantilevered structures, lighting poles, tall telecommunications structures (monopoles), to name a few, can undergo significant motions under wind loads, which may induce fluid structure interactions and consequently affect the wind flow and pressure around them. These motions could be buffeting, galloping or flutter due to gust or vortex shedding.

Buffeting is normally an along-wind oscillation caused by several mechanisms such as gusts, turbulence, and vortex shedding in the wake of another structure or in the wake of an exposed element in the same structure (i.e., faces of a 3-D truss). Gusts are essentially fluctuations in the wind velocity, typically measured from an average value taken on a certain duration (for example hourly mean average for most exposed civil engineering structures). Gusts generate fluctuating forces on the structure forcing it to move and typically involving dynamic response (inertia effects) in addition to elastic and aerodynamic force effects. Vortex shedding is a well-

known phenomenon which exists due to alternating pressure gradients and separation of wind flow from the structure, which pushes the structure to vibrate in the crosswind direction. It becomes critical for the structure when the shedding frequency coincides with the structure fundamental (or some higher mode) natural frequency as resonance occurs with sustained large oscillations, depending on the damping level. These vibrations take place over a limited range of wind velocities, and the resulting vibration amplitudes are self-limiting [113]. Galloping is a high-amplitude low-frequency vibration, where the amplitude continuously increases when the wind velocity is above the galloping critical velocity. Classical flutter is a motion that relies on the coupling between two modes of vibration. Structures commonly affected by flutter are suspension bridges, tall non-circular towers, and stacks where substantial bending and torsion occurs.

So, in theory, flexible structures exposed to wind will experience different aerodynamic forces than rigid structures of comparable cross-sectional properties. In practice, some exposed flexible structures under turbulent wind may undergo important vibrations due to resonance, which can lead to boosting or diminishing loads/responses. This happens because as the structure moves aerodynamic damping is generated. If it is positive, vibrations dissipate naturally without any issues. However, a negative value indicates a concern as it leads to amplification of the structure's motion, that could surpass the inherent structural damping [114]. Consequently, relatively slender structures and exposed structures like highway signage structures, luminaries, poles, or building appendages, may be vulnerable to the effects of wind in ways that are difficult to predict using standard procedures.

From an overview of the literature many studies [12-14, 55-57] have shown potential change in the wind forces acting on exposed members due to dynamic instability. Some of these studies [12, 13, 55, 57] concluded that the force coefficients increase till they reach the stationary value at lock-in and then decrease monotonically. On the contrary other studies [52, 56] showed that

the force coefficients decrease to a minimum at lock-in then increase till they reach the stationary value. Two recent numerical investigations of the flow around flexibly-supported square cylinder sections under low Reynolds numbers have concluded that the drag and lift coefficients exceed those of a stationary cylinder [59, 60], and it remains to be seen whether the trend is maintained at Reynolds numbers that are more representative of turbulent wind flow conditions in exposed structures. In another experimental study for a forced two-degrees-of-freedom streamlined bridge deck, it was shown that buffeting forces for an oscillating model might have RMS values up to 10% higher than their stationary model equivalents; this increase was typically for frequencies above f*D/U=0.1 [58]. The study also points out that as bluffness increase this difference increase i.e., when separation happens over a larger area of the body it might exhibit more considerable variations between oscillating and stationary buffeting levels. Applying this finding to the cross sections under investigation, it is found that the flow is separated over the whole cross section, which means that the buffeting forces should increase on oscillating.

As for the angle cross section, Slater (1969) found that the magnitude of the unsteady aerodynamic lift coefficient during plunging resonance was significantly higher than that of the stationary results [8]. He also added that turbulence suppresses resonant vibrations and consequently the unsteady aerodynamic coefficient decreases. Furthermore, the unsteady forces are at a maximum for input wind flow orientations in the ranges $0° < a < 45°$ and $95° < a < 145°$ (orientations based on NBC 2015 [44]). The results also indicated that galloping would happen at very low damping or only extremely high wind speeds outside the range of practical interest [8].

In this paper we are investigating the effect of flexibility of exposed slender structures on loads/responses and whether this flexibility could lead to boosting or diminishing them, in comparison with the stationary assumption. The main query is intended to determine whether

wind-structure interactions in flexible exposed structures may have a significant influence on the forces/responses on the structure itself. At first, a square cylinder and an equal legged angle cross-section member under wind flow was studied in wind tunnel. These sections were chosen because the wind flow around them is characterized by separation at the front corners, which creates a large wake that increases the possibilities of motion-induced vibrations. Additionally, a truss panel comprised of square, and angle shaped elements was studied to monitor the effect on a full structural model. The aerodynamic derivative H_1^* was derived from these wind tunnel experiments as reported in chapter four. A CFD simulation was conducted for all the structural models; details on the square could be found in [1] while the truss panel simulation is shown in this paper. At last, a finite element model of a whole structure comprised of the tested structural models was created. Dynamic analysis was performed using forces from CFD simulations, once using the structural damping only and another time adding the aerodynamic damping to the structural damping. Forces and responses of the structural model from both cases were compared and conclusions were drawn.

This chapter is divided into five sections. The first section (this section) provides an introduction on the types of vibrations encountered by a structure and a brief literature review on the effect of flexibility on aeroelastic forces. The second section describes the wind tunnel (WT) test facility along with the test setting, measuring equipment and models tested, in addition to results and validation. The third section presents the CFD simulations carried out along with validation and results. The fourth section explains the procedures followed for the dynamic analysis of the three-dimensional truss used as an example to illustrate the procedure. Conclusions drawn from the study are provided in section five.

5.3 Wind Tunnel

The current experimental work took place in the wind tunnel test facility located at Toronto Metropolitan University (TMU, formerly known as Ryerson University), Toronto. This section

provides details about the dimensions and operating system of the wind tunnel, followed by an illustration of the system that was installed to accommodate the testing requirements.

5.3.1 Wind Tunnel Facility

The TMU wind tunnel is a closed loop one that operates on a large fan, which has a range of speeds from 4 m/s up to 30 m/s. The tunnel allows for smooth flow. The test section is the narrowest part of the tunnel as shown in Figure 4-1, with a cross section of 91x91 cm. For more details refer to [107].

5.3.2 Test Set-Up and Measuring Tools

The tested specimens are in free vibration and a specific setting was designed, built, and installed as shown in Figure 5-1. More details are available in chapter four.

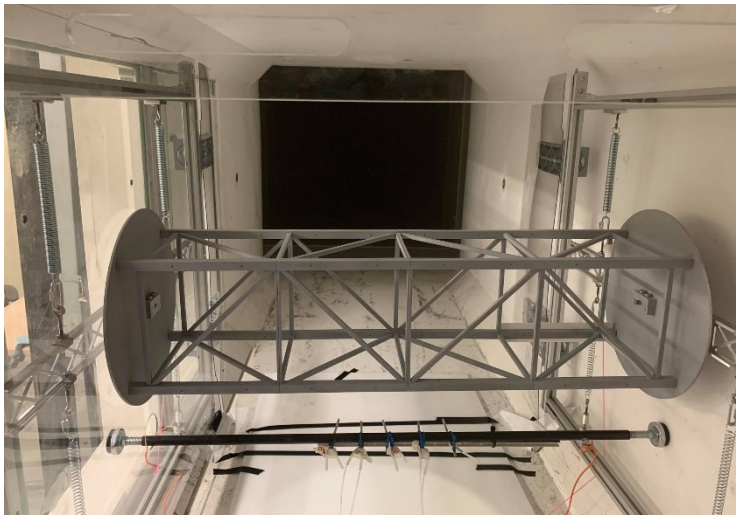

Figure 5-1 Truss specimen in TMU Wind Tunnel

5.3.3 Models Tested

Three models were tested: a rigid hollow square cylinder, a member with an equal-leg angle cross section, and a W Truss with a square cross section - see Figure 5-2. The angle cross-section was tested at two angles of attack 45° and 135° measured as shown in Figure 5-3. The truss chords, verticals and diagonals were made of square cross section Figure 5-4. The parameters of the three models are shown in Table 5-1. D is the dimension, L is the length, M

is the mass, K is the stiffness, $F_n = \omega_n/2\pi$ is the natural frequency, ζ is the structural damping, U_{red} = V/(F_n*D), where V is the wind velocity inside the tunnel and $R_e = \frac{\rho V\ D}{\mu}$ is Reynolds number, where ρ (kg/m^3) is the air density and μ (kg/m.s) is the air viscosity.

Table 5-1: Model parameters

Model	D(m)	L(m)	M(kg)	K(N/m)	F_n (Hz)	ζ	U_{red}	Re
Square	0.076	0.77	1.37	8572	12.59	0.30%	4-29	$2.2x10^4$ to $15x10^4$
Angle	0.055	0.75	1.2	7905	12.93	0.64%	4-29	$1.4x10^4$ to $8.1x10^4$
Truss	0.19	0.78	2.14	8754	10.18	0.59%	4-13	$6x10^4$ to $35x10^4$

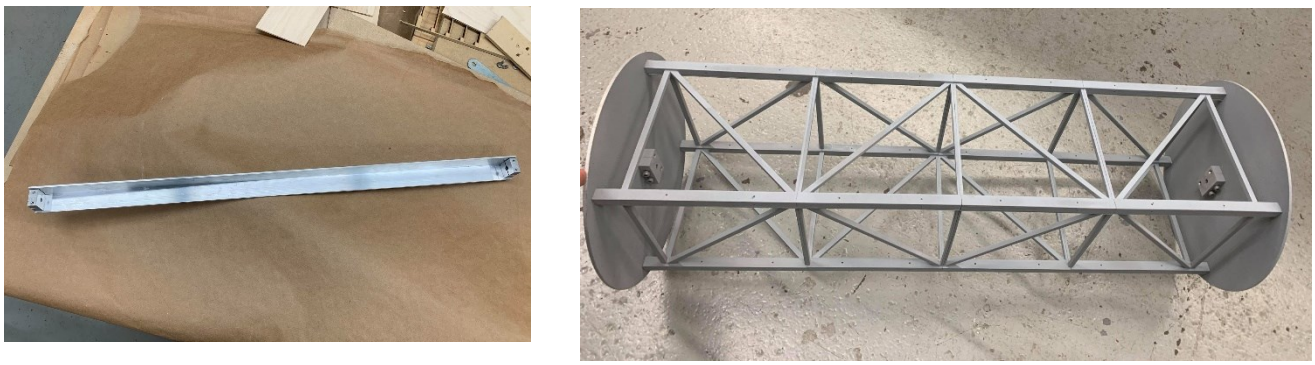

(a) (b)

Figure 5-2 (a) Angle test specimen (b) four-panel truss specimen

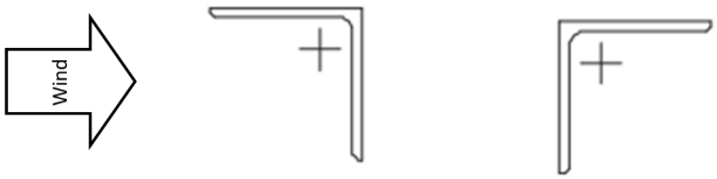

45° 135°

Figure 5-3 Different orientations for the Angle shape

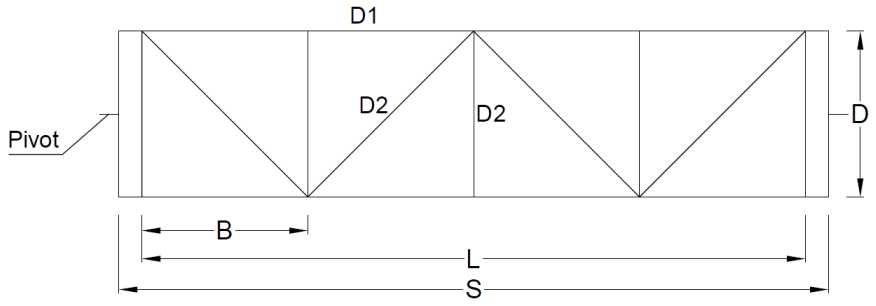

Figure 5-4 Truss with four panels

5.3.4 Testing Procedures

The procedures explained here were repeated for each model. First the dynamic properties were determined (mass, stiffness, and fundamental frequency), followed by a free-decay test to find the system structural damping (ζ). Then, the models were tested by giving an initial push then leaving it to freely vibrate in the cross-stream direction only. This step was repeated five times during a recording cycle of 1 minute at a frequency of 512 Hz. During this process the forces were measured.

5.3.5 Results and Validation

The aerodynamic derivative H_1^* for the square cylinder showed good agreement with the literature as shown in Figure 5-5. The H_1^* derivative for the angle member at different angles of attack was determined using equation 5-1 and results were plotted against U_{red} in Figure 5-6 and Figure 5-7. Figure 5-8 shows the H_1^* derivative of the four-panel square truss (Figure 5-4) at solidity ratio = 0.23.

$$H_1^* = \frac{-4\,\zeta_a\,m}{\rho\,D^2} \qquad 5\text{-}1$$

Where, m : mass of the body per unit length, ρ: density of air, D: stream-wise dimension, and ζ_a: aerodynamic damping.

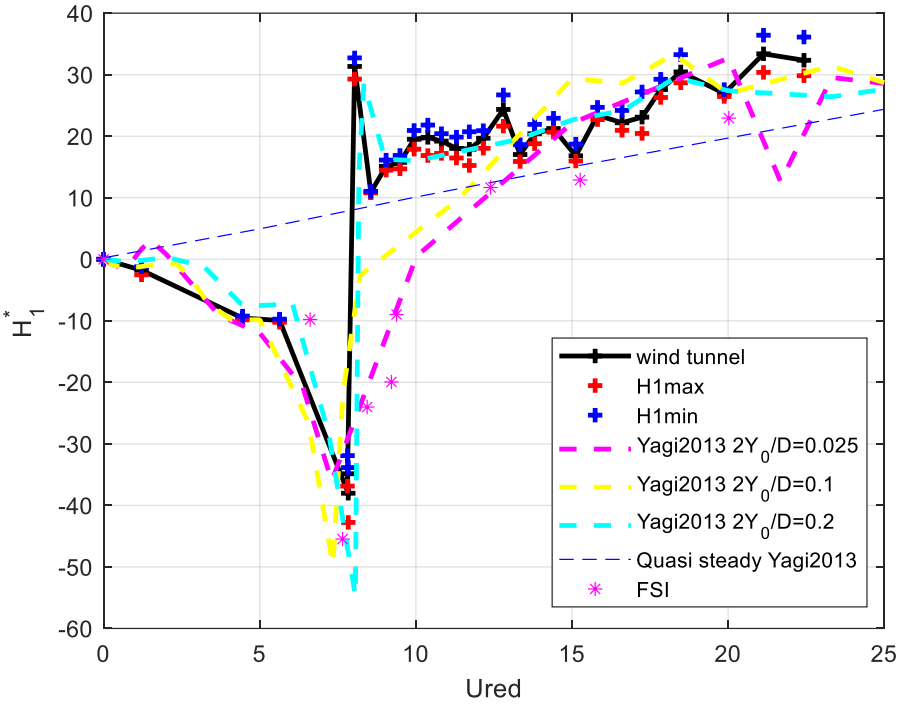

Figure 5-5 H_1^* aerodynamic derivative for square cylinder versus reduced velocity (U_{red})

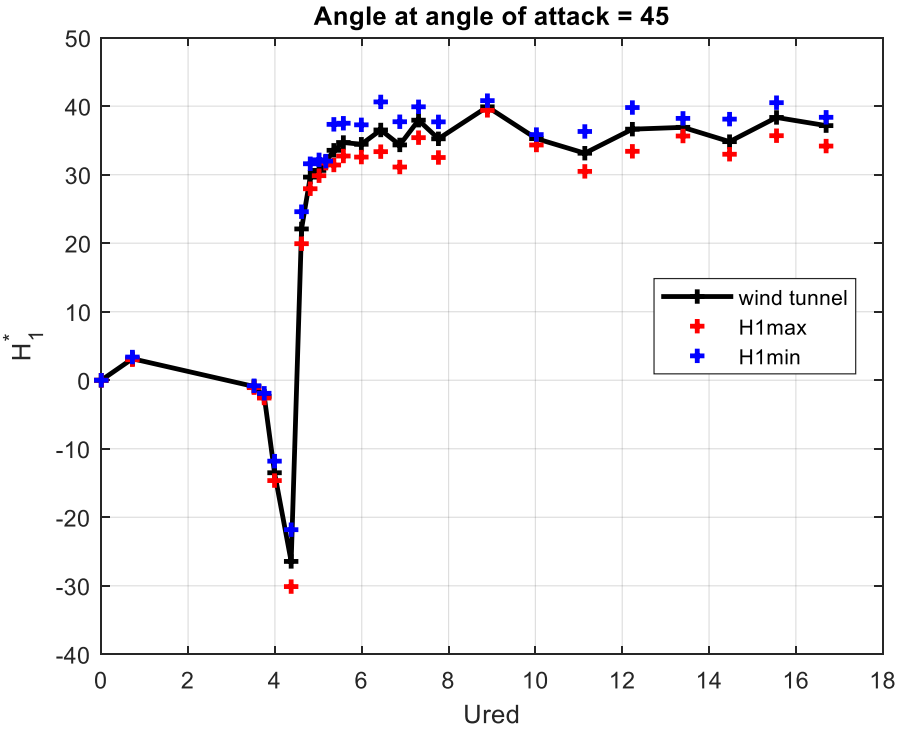

Figure 5-6 H_1^* aerodynamic derivative versus reduced velocity (U_{red}) for angle cross section at angle of attack 45°

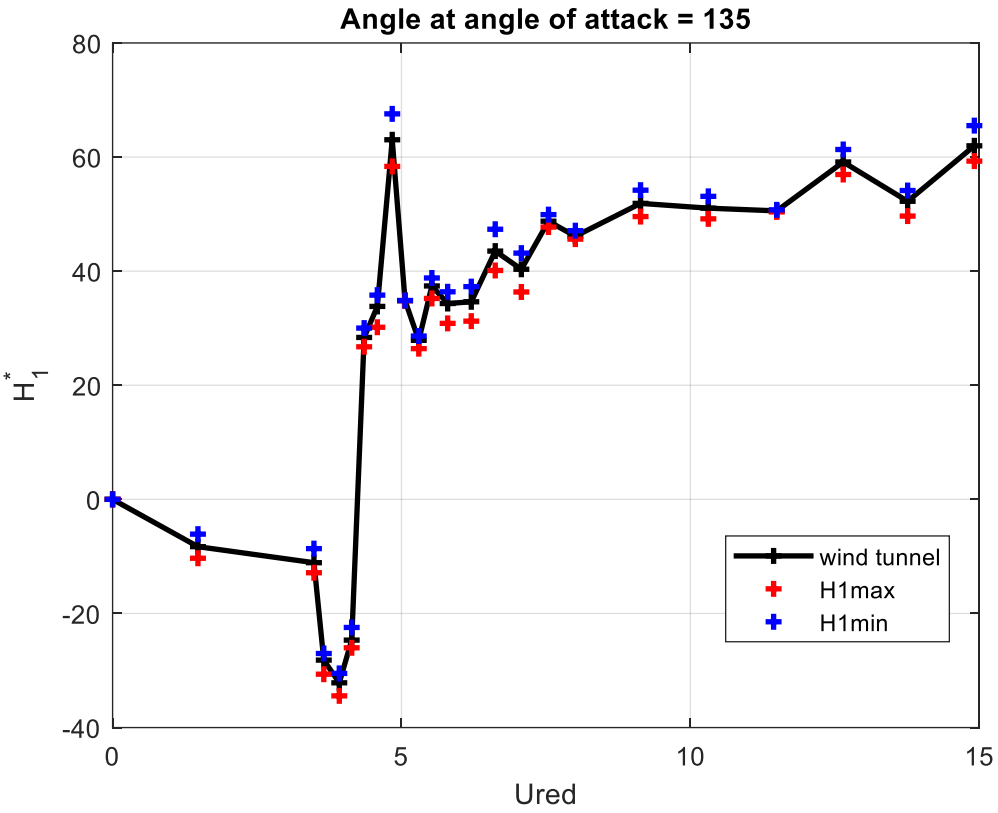

Figure 5-7 H_1^* aerodynamic derivative versus reduced velocity (U_{red}) for angle cross section at angle of attack 135°

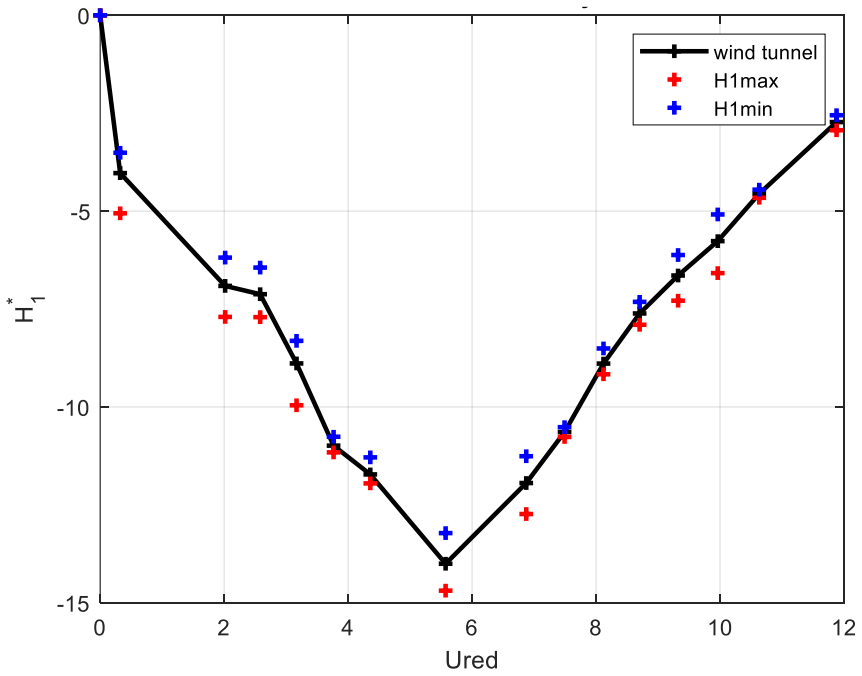

Figure 5-8: H_1^* aerodynamic derivative versus reduced velocity (U_{red}) for truss with solidity ratio = 0.23

5.4 Computational Fluid Dynamics (CFD)

In this section, CFD models for the cross sections tested in wind tunnel, were simulated using large eddy simulations (LES) to estimate the aerodynamic forces and coefficients.

5.4.1 Square Cross Section

The CFD simulation carried for the square cylinder was thoroughly studied in Chapter 3 where details were provided for the mesh, boundary conditions and simulation parameters [1]. Figure 5-9 shows the mean drag coefficient (equation 5-2) and the rms of the lift coefficient (equation 5-3) over a range of angles of attack for the stationary cylinder calculated from CFD simulations carried in a study previously done by the authors [1].

$$C_L = \frac{F_L}{\frac{1}{2}\rho v^2 BL} \tag{5-2}$$

$$C_D = \frac{F_D}{\frac{1}{2}\rho v^2 DL} \tag{5-3}$$

Where, C_D: drag coefficient, F_D: drag force, ρ: air density, v: mean velocity, D: dimension in the across wind direction, B: dimension in the along wind direction, L: length, C_L: lift coefficient and F_L: lift force.

Figure 5-10 and Figure 5-11 show the change in the mean drag coefficient and rms lift coefficient versus Reynolds number (R_e), respectively, at zero angle of attack. The coefficients were calculated from simulations that were once initialized using the results from the previous velocity (increasing velocity) and the other simulations (in red) were initialized by using the velocity at which the simulation was carried. The mean aerodynamic drag coefficient ($C_{\mathrm{D_{mean}}}$) was found to be around 2.15 for the range of Reynolds numbers studied.

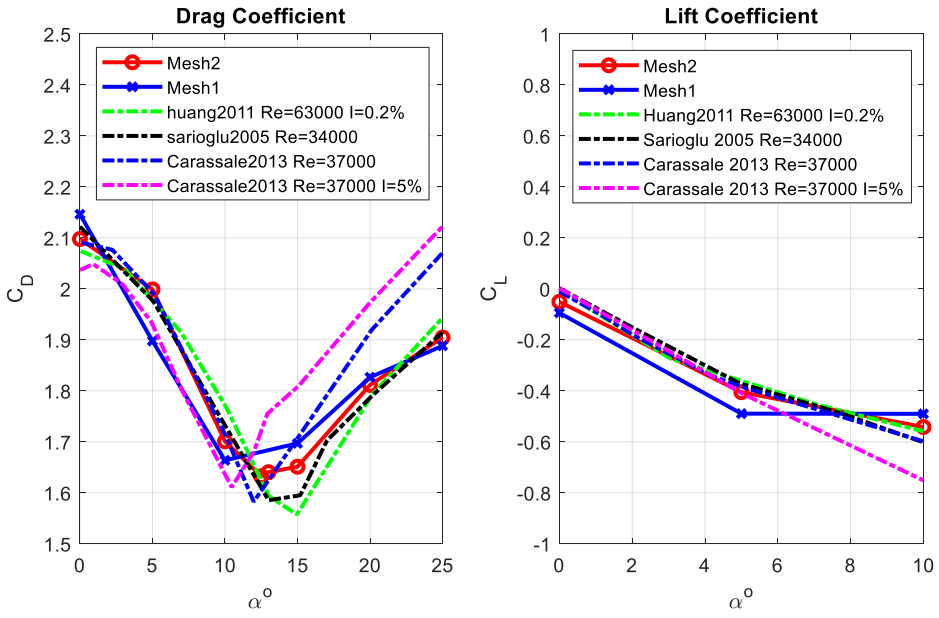

(a) (b)

Figure 5-9 (a) Drag coefficient (b) lift coefficient at different angles of attack

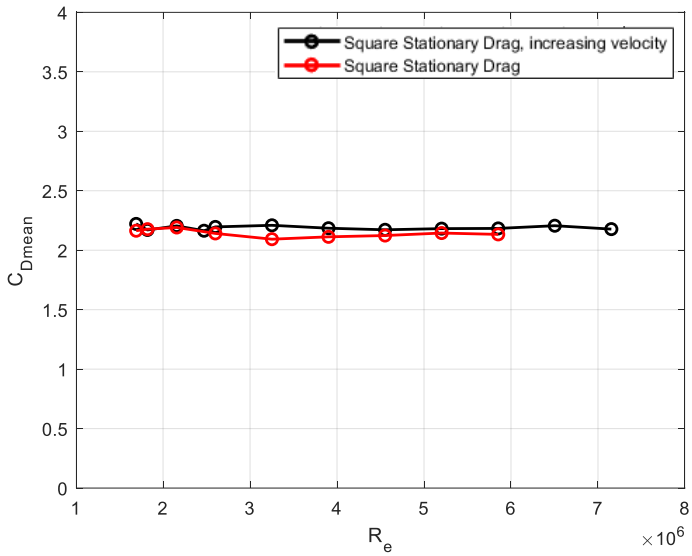

Figure 5-10 $C_{D_{mean}}$ versus R_e for a stationary square cylinder in smooth flow

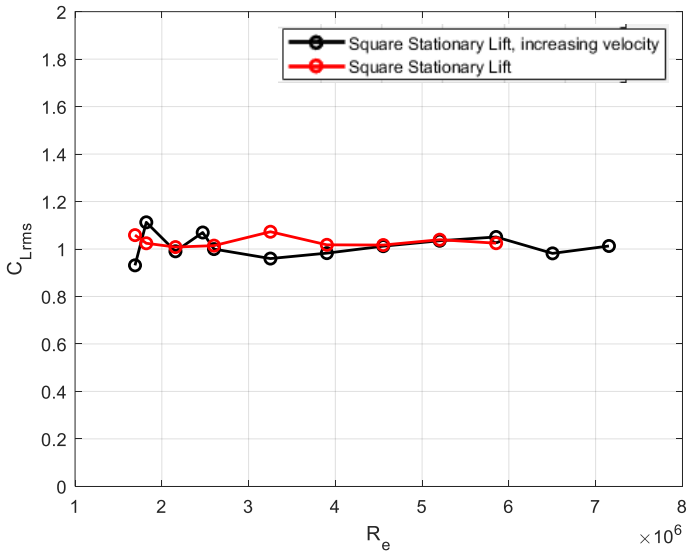

Figure 5-11 $C_{L_{rms}}$ versus R_e for a stationary square cylinder in smooth flow

5.4.2 Angle Cross Section

The same parameters and mesh used for the square cylinder, were used for the angle cross-section cylinder. The angle cross-section member was tested under angles of attack 0-180 as seen in Figure 5-12. Figure 5-13 and Figure 5-14 represent the mean drag coefficient $C_{\mathrm{D_{mean}}}$ and the rms of the lift coefficient $C_{L_{rms}}$ versus the angle of attack, respectively, where it shows reasonably good validation with the literature. The $C_{\mathrm{D_{mean}}}$ and the $C_{L_{rms}}$ over a range of Reynolds numbers for the stationary angle member at zero angle of attack calculated from computational fluid dynamic (CFD) simulations are plotted in Figure 5-15 and Figure 5-16.

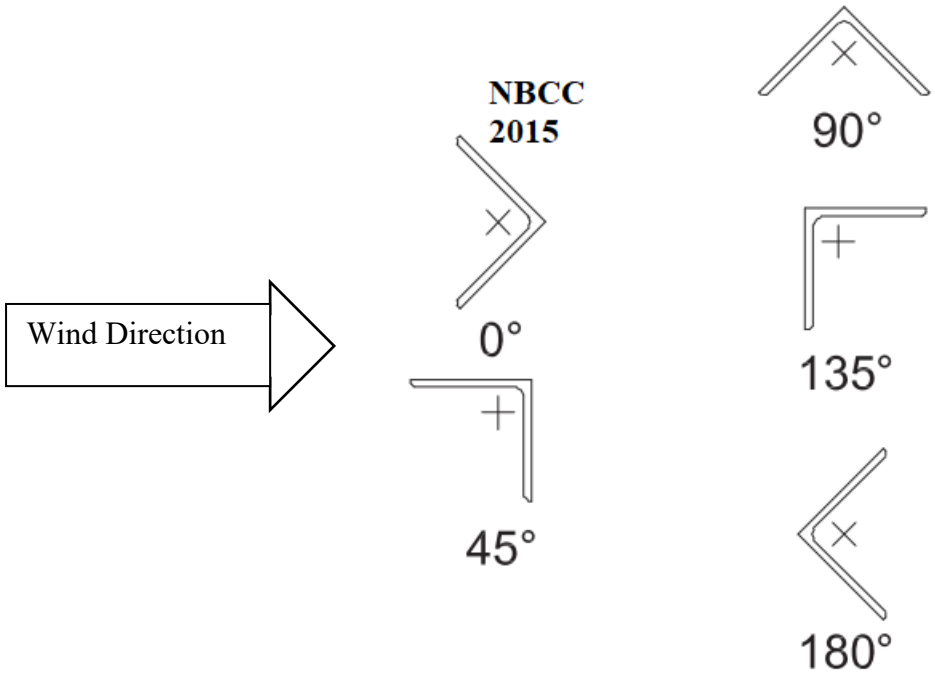

Figure 5-12 Angle orientations tested

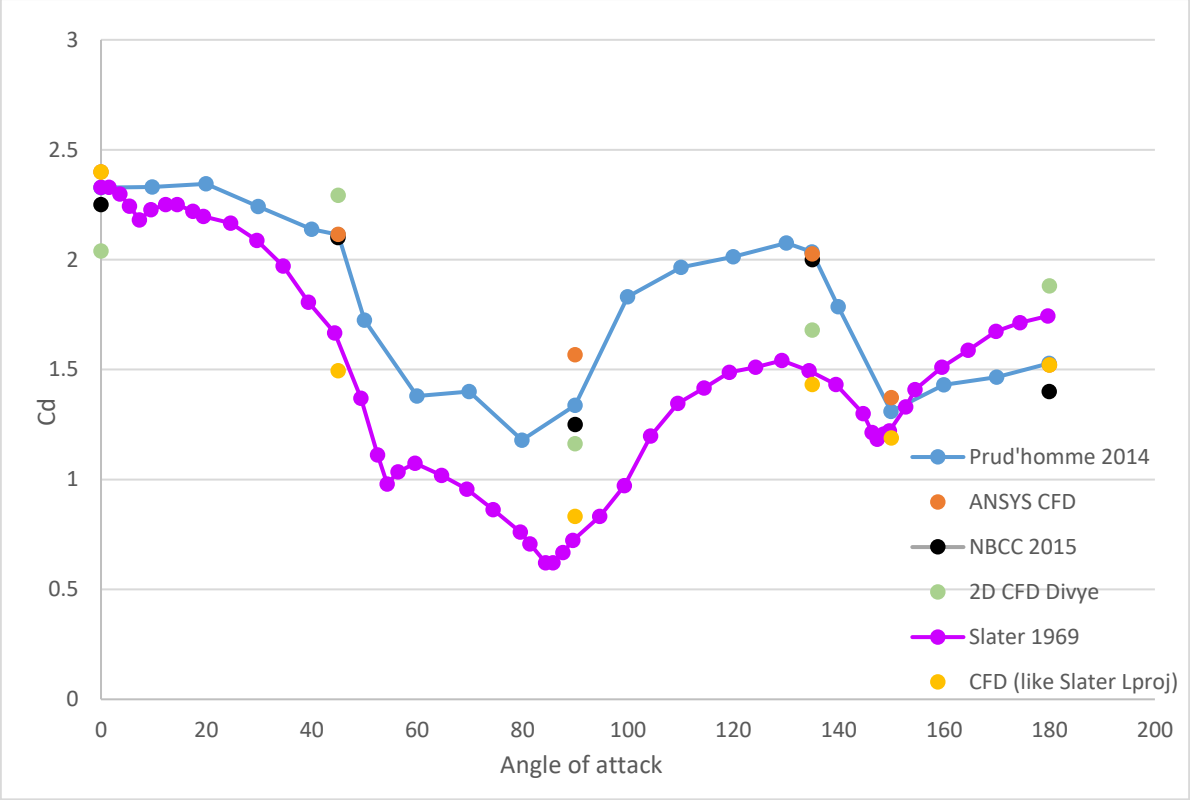

Figure 5-13 $C_{D_{mean}}$ versus angle of attack

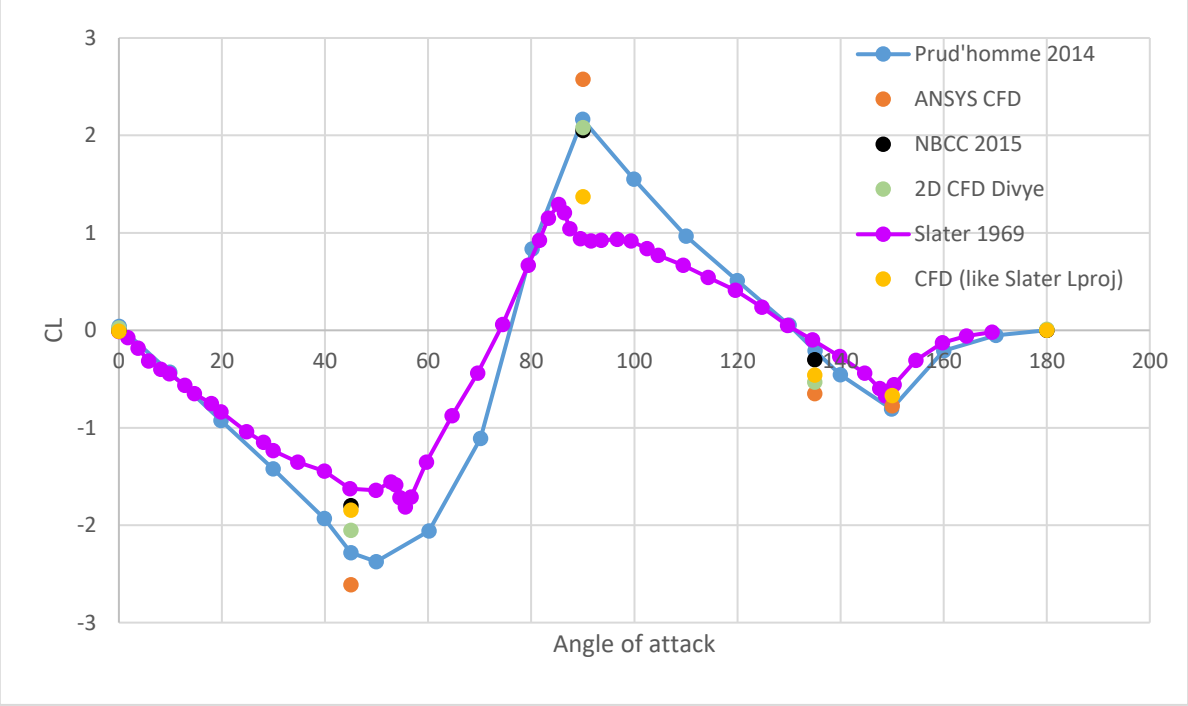

Figure 5-14 $C_{L_{rms}}$ versus angle of attack

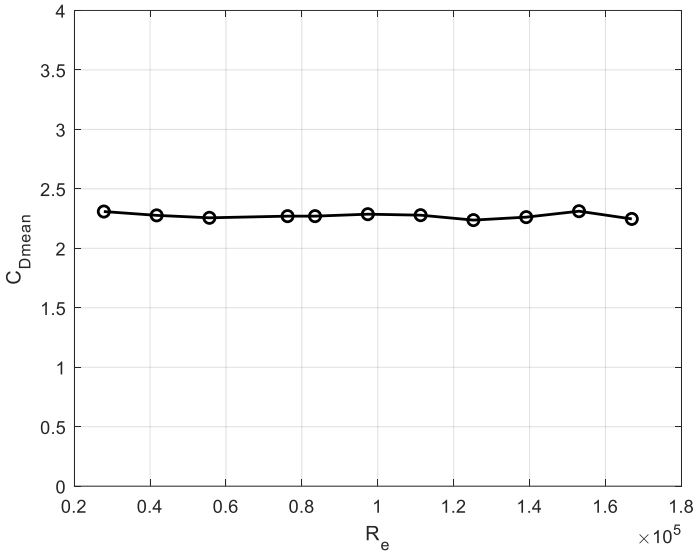

Figure 5-16 $C_{D_{mean}}$ versus Re for a stationary angle cylinder in smooth flow at zero angle of attack

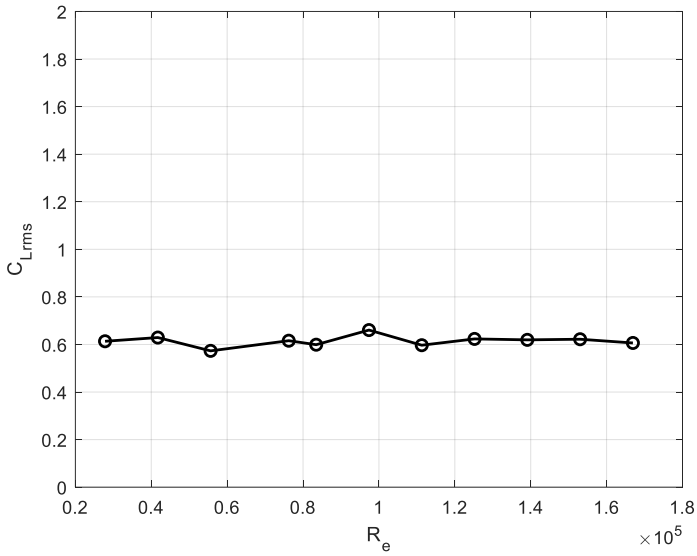

Figure 5-15 $C_{L_{rms}}$ versus Re for a stationary angle cylinder in smooth flow at zero angle of attack

5.4.3 Four-Panel Truss

A W Truss shape with equally spaced panels, a square cross-section, and square elements was simulated under wind flow using CFD simulations as well. The truss tested and the fluid domain boundary conditions are shown schematically in Figure 5-17. Figure 5-18 shows the truss elevation and cross section. The truss had a solidity ratio of 0.23 and was simulated for smooth and turbulent flows. The domain size was 1.3D inlet, 3D outlet, 3.3D cross stream and 3.7D spanwise and all dimensions were chosen following the recommendations by Nakayama [115] as shown in Figure 5-19. A mesh with polyhedral elements was adopted with a total number of 750,000 elements (see Figure 5-20). Simulations were done for 36 shedding cycles, with non-dimensional time step $tV/D = 4.2 \times 10^{-4}$ at $Re = 3.15 \times 10^5$ for validation with literature. Each simulation took 30-40 days with the available computing resources. The simulations were done for a range of Reynolds number $Re = 0.53 \times 10^5$ to 3.15×10^5 based on height D. Ten simulations were done at distinct velocities, same as which the wind tunnel test was performed.

Comparison was done at Re = 3.15×10^5, for smooth flow and at turbulent intensity = 11% and 20%, see Table 5-2.

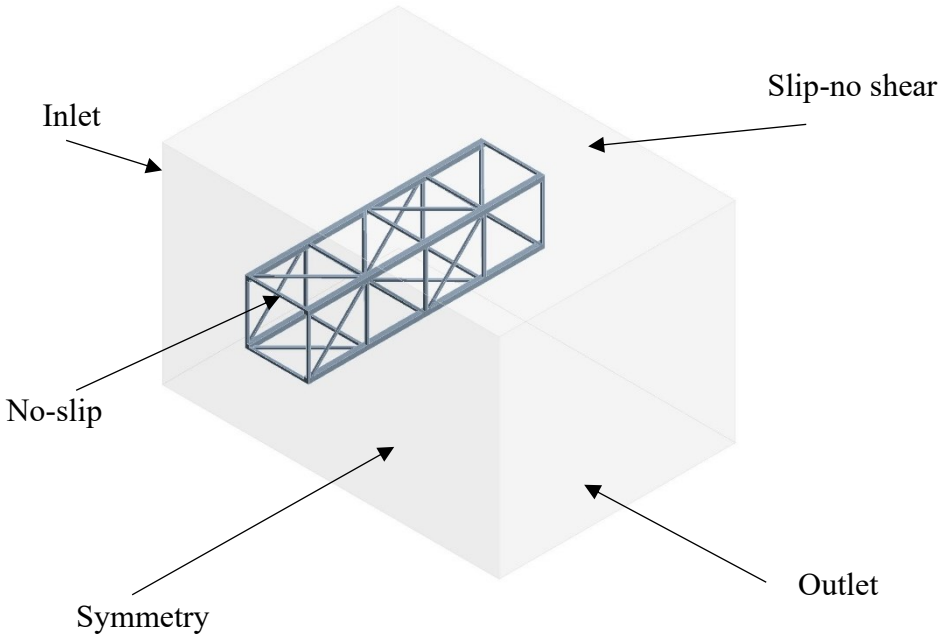

Figure 5-17 CFD boundary conditions

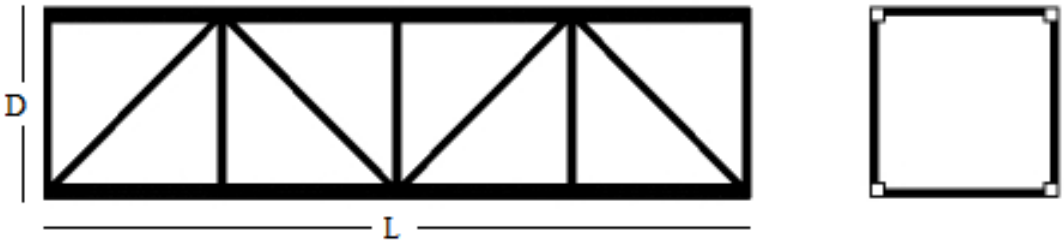

Figure 5-18 Four-panel truss simulated

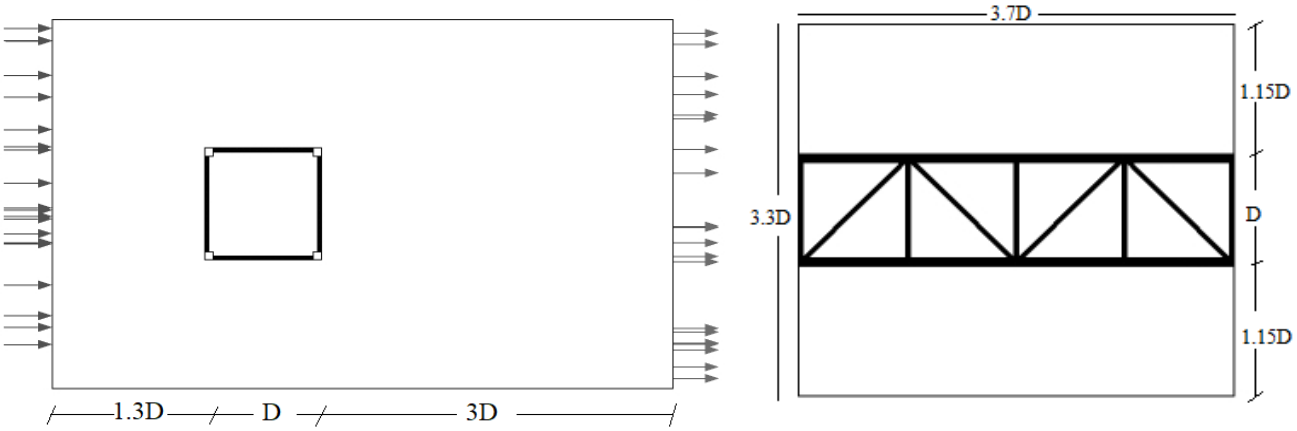

Figure 5-19 CFD domain dimensions

Table 5-2 Truss lift and drag aerodynamic coefficients for different turbulence intensities

	solidity ratio	blockage ratio (%)	I%	$C_{D_{mean}}$	C_{Lrms}
Case 1	0.23	6.97%	smooth	3	0.2
Case 2	0.23	6.97%	11%	2.95	0.67
Case 3	0.23	6.97%	20%	2.78	0.7
CSA-S37-18	0.23			2.86	
Nakayama	0.23			2.8	

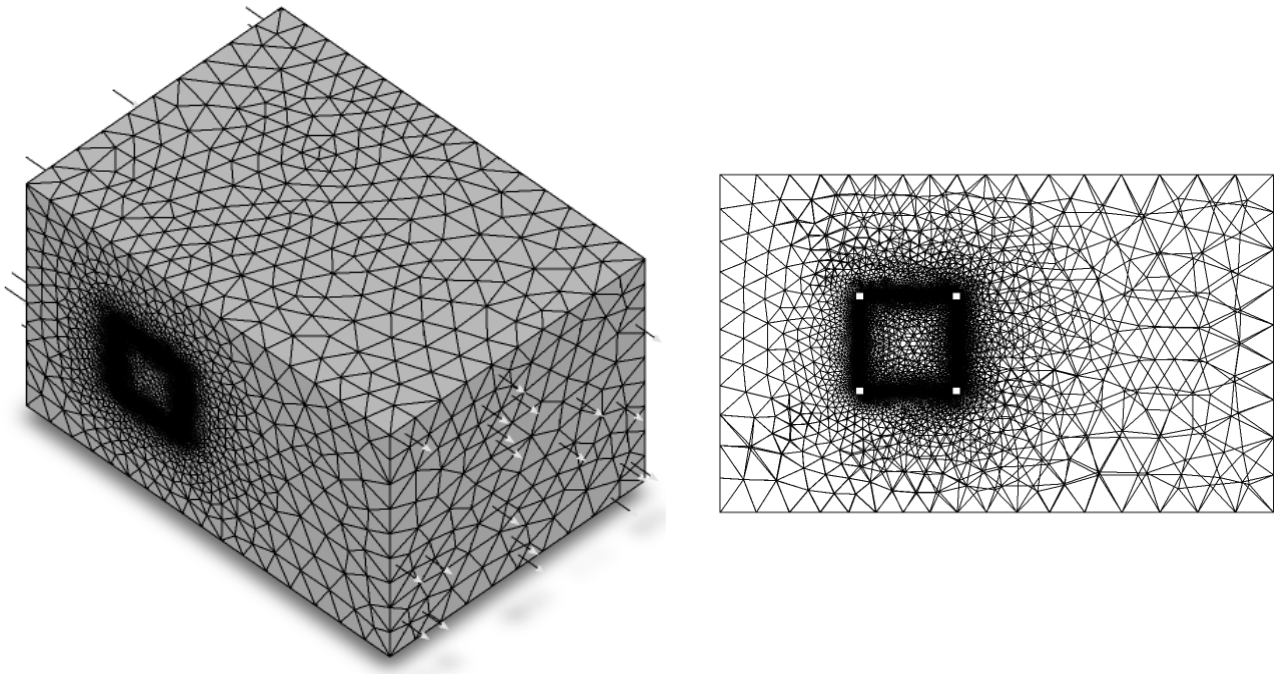

Figure 5-20 Polyhedral mesh

The drag coefficient for square lattice structure with flat members according to CSA-S37-18 is calculated from equation 5-4, where R_s = 0.23 (solidity ratio) and multiplied by K_d in equation 5-5, where K_1 = 0.55, K_2 = 0.23. Therefore, C_{df} = 2.86, which is comparable to results for the smooth simulation as shown in Table 5-2. Additionally, the drag coefficient was in good agreement with the results of the CFD simulation by A. Nakayama et al. where a value of C_d = 2.5 was reported for a smooth flow at R_e = 4x10^5 and filling ratio of 0.23 [115]. It was reported by A. Nakayama et al. that according to the Architectural Institute of Japan C_d = 2.8.

$$C_{df} = 4(R_s)^2 - 5.9(R_s) + 4 \qquad 5\text{-}4$$

$$K_d = 1 + K_1 K_2 \sin^2 2\theta \qquad 5\text{-}5$$

Truss simulations were also done at different velocities i.e., different Reynolds numbers and results are shown in Figure 5-21. It was clear that the drag and lift coefficients remains almost the same throughout the range of Reynolds numbers tested.

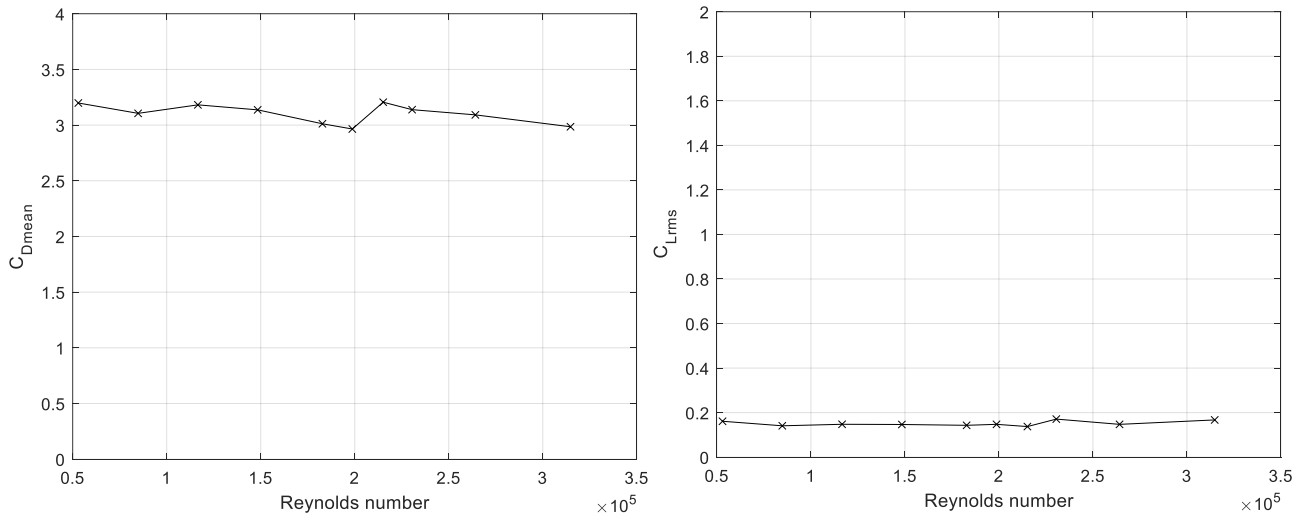

Figure 5-21 $C_{D_{mean}}$ and $C_{L_{rms}}$ versus Re for a stationary four panel truss in smooth flow

5.5 Dynamic Analysis

The wind tunnel test provided data on the aerodynamic damping values for different structural members. This section will examine the effect of adding aerodynamic damping on the response of different structural elements and a full structure using structural dynamic analysis in SAP2000 V20.2. With the knowledge of the lift forces from CFD simulations [1], linear modal time history analysis was performed to obtain the vibrational responses for a square and truss structure as shown in the following sections.

5.5.1 Square Cylinder

The square cylinder was modeled as a single-degree-of-freedom system. Time history analysis was done using the time history of the aerodynamic forces obtained from the CFD stationary simulations. Displacements were calculated with and without the effect of aerodynamic damping. Figure 5-22 shows an example of the time history of aerodynamic force at U_{red} = 9. Figure 5-23 (a) and (b) shows an example of the time history of displacement at U_{red} = 9 with structural damping only and with structural and aerodynamic damping, respectively.

The flow chart in Figure 5-24 shows the steps followed to find the displacement taking the aerodynamic damping into account. Firstly, H_1^* for the square cylinder (or cross section under investigation) was used to find the aerodynamic damping with the knowledge of mass and characteristic dimension. Next, modal analysis of the cross section was carried out to determine the fundamental frequency. After that, the aerodynamic lift force time history from stationary CFD simulations was used to perform dynamic linear modal analysis with the structural damping as the modal damping. The last step was repeated using the aerodynamic damping and the structural damping as the modal damping. The procedures were repeated for each velocity. Comparison of results is shown in Figure 5-25.

The displacements showed agreement with the literature [103], and it was quite clear that the displacements were amplified at two locations. The first location was at vortex-induced vibrations (VIV), where the inclusion of aerodynamic damping resulted in vibrations surpassing those observed when considering only structural damping. This behaviour was observed across the entire range of VIV. The same happened at high reduced velocities, U_{red} > 20 for the case under consideration. The increase in displacement was mainly because at these reduced velocities the aerodynamic was negative, decreasing the total damping and therefore increasing the vibrations. On the other hand, the decrease in displacement was because at these reduced velocities the aerodynamic damping was positive and therefore adding to the total damping which eventually suppresses the vibrations.

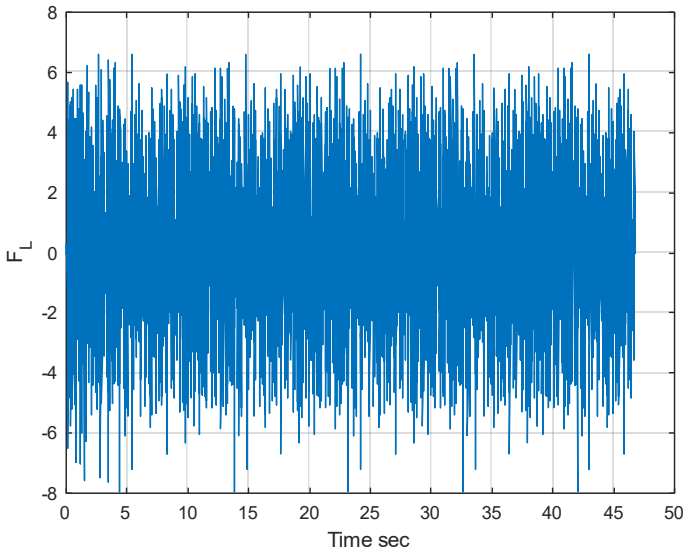

Figure 5-22 Time history of Lift force for the square cylinder at U_{red} = 9

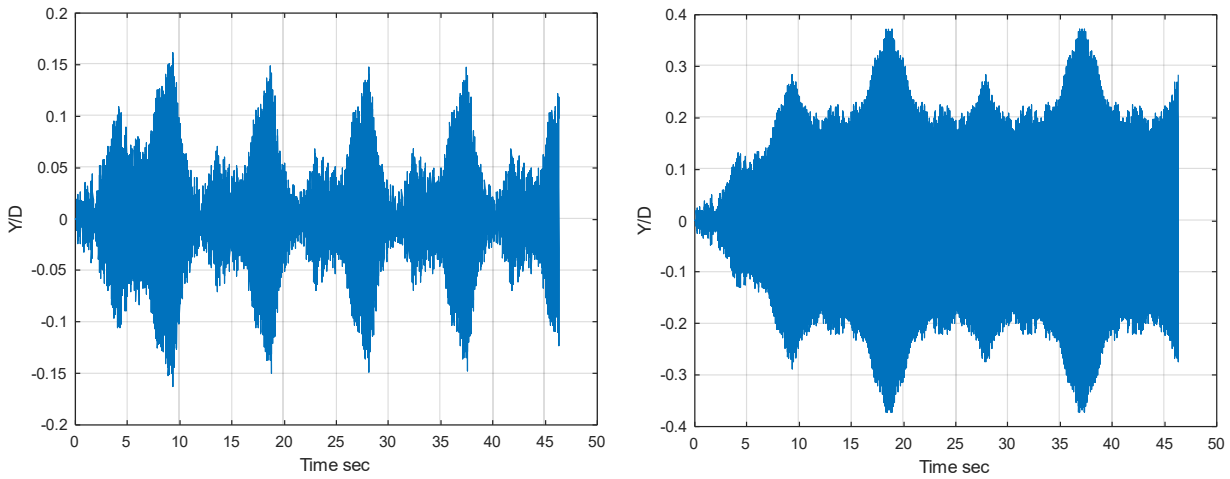

(a) (b)

Figure 5-23 Time history of vibrations for the SDOF square cylinder (a) with structural damping only (b) with structural and aerodynamic damping

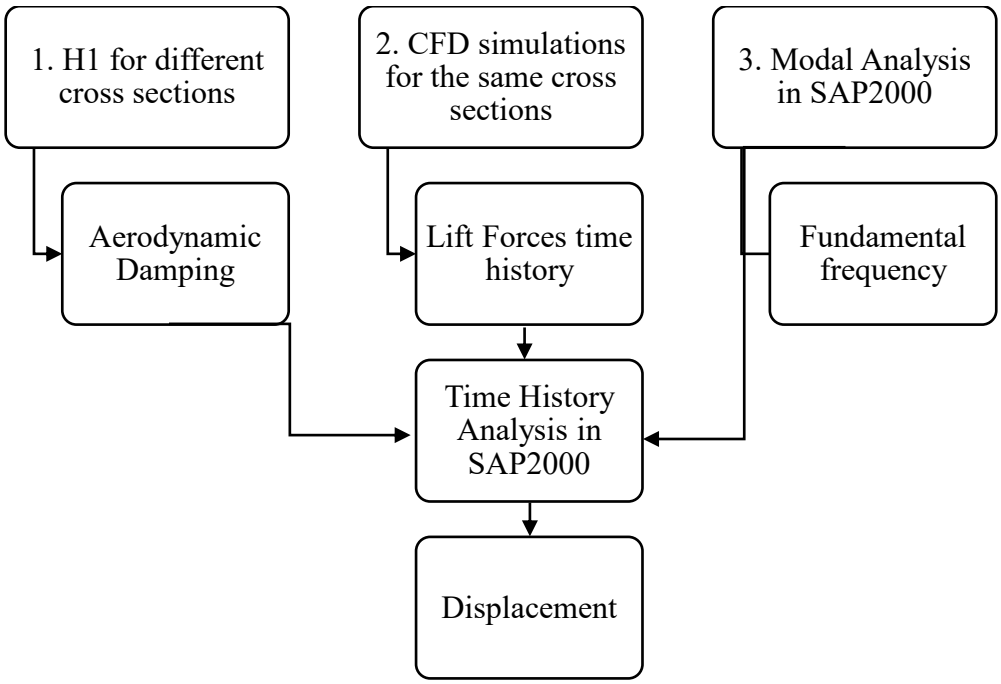

Figure 5-24 Flow chart for calculation of displacement for the square cylinder

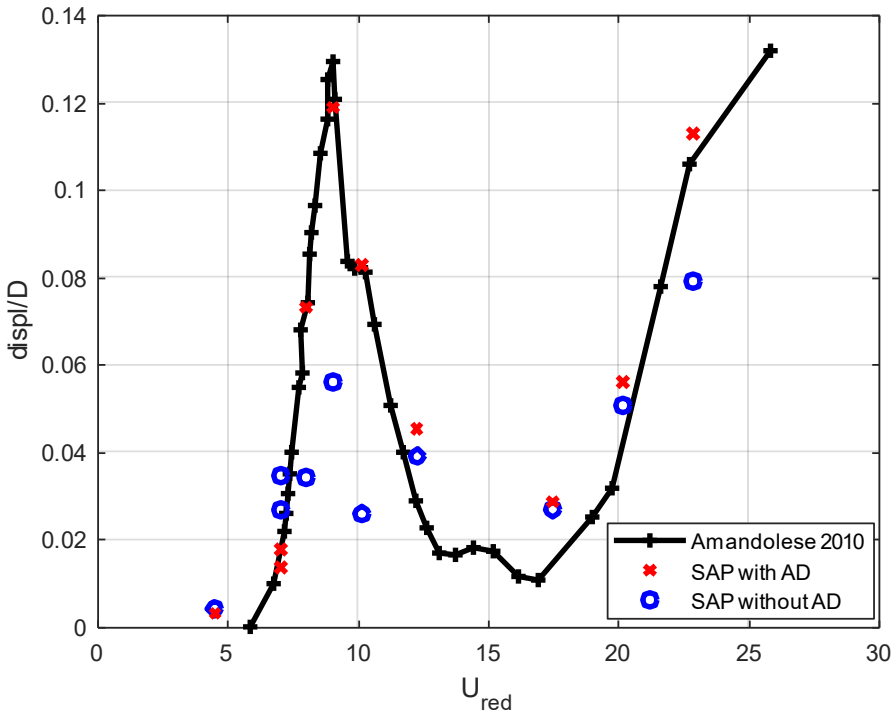

Figure 5-25 U_{red} vs Displacement for square cylinder with and without aerodynamic damping

5.5.2 Truss

In this section, a structural dynamics analysis was done for the lattice structure shown in

Figure 5-27, composed of the four-truss panel tested earlier in the wind tunnel. This was done through three steps as explained below and shown in chart, Figure 5-28. The first step is to determine the time history of the aerodynamic forces through running stationary CFD simulations, which was explained in section 5.4.3. The second step is to find the frequency of vibrations and the overall structural damping for the whole structure, for all the modes, as explained below in section 5.5.2.1 and 5.5.2.2 respectively. The third step is the calculation of the aerodynamic damping using the aerodynamic derivative as explained below in section 5.5.2.3.

5.5.2.1 Modal Analysis

Modal analysis of the structure was done to determine its natural modes of vibrations and their frequencies as shown in Figure 5-26 and Table 5-3. It is seen that the first two modes correspond to the fundamental sway mode (flexural) along the principal geometric directions and their frequencies are very close (0,785 Hz and 0,790 Hz), which indicates that they are both likely excited by any wind direction. This is expected given the symmetry/anti-symmetry of the topology of the truss. The third mode is well separated (at 1,34 Hz) and is torsional. Modes 4 and 5 are again closely spaced (2.88 Hz and 2.94 Hz) and correspond to the second flexural mode.

5.5.2.2 Structural Damping

The structural damping for the first and second modes (the fundamental sway modes) was assumed to be = 1% for the purpose of the study. In practice, welded trusses used in telecommunication structures have structural damping in the order of 1-2% while bolted trusses experience the higher range of 2-3%. The Rayleigh method was used to calculate the structural damping for the higher modes according to equation 5-8. In this case the first and second modes are prescribed to have the same damping ratio (ξ), and the constants a_0 and a_1 were calculated from equations 5-6 and 5-7. Subsequently, the structural damping ratio (ξ_{st}^n) for any higher modes of circular frequency (ω_n) could be estimated using equation 5-8, which were found to be 1.15%, 1.96% and 2.0% for the 3rd, 4th and 5th modes respectively.

$$a_0 = 2\xi \frac{\omega_1 \omega_2}{\omega_1 + \omega_2} \quad 5\text{-}6$$

$$a_1 = 2\xi \frac{1}{\omega_1 + \omega_2} \quad 5\text{-}7$$

$$\xi_{st}^n = \frac{a_0}{2\omega_n} + \frac{a_1 \omega_n}{2} \quad 5\text{-}8$$

5.5.2.3 Aerodynamic damping determination

The aerodynamic damping was determined using equations 5-10 to 5-13. A log law velocity profile for an open terrain was used, as shown in equation 5-9 where, V_{ref} is the velocity at the top level of the structure, h is the height at which the calculation was carried and V^h is the velocity at that height, h_{ref} is the total height of the structure and α is 0.16 for an open terrain [116]. First, the structure was divided into 'l' number of levels, where the reduced velocity changed at each level and consequently H_1^*. Each level had a lumped mass (m_f) and a lateral stiffness (k_f). Consequently, for each mode the aerodynamic modal damping coefficient ($C_{ad}^{n,l}$) was calculated at each level 'l' using equation 5-10 where, ω_n is the circular frequency of the mode and D (2m) is the characteristic length of the lattice structure under study [98]. Following that, the modal damping coefficient for each mode was calculated using equation 5-11 where, $\varphi_{n,y}$ is the mode shape in the crosswind direction (y). Since the damping matrix is diagonal equation 5-11 could be rewritten as equation 5-12 and the aerodynamic modal damping ξ_{ad}^n was determined from equation 5-13, where M_n is the modal mass. The modal aerodynamic damping ξ_{ad}^n was calculated for the first five modes of vibrations at each considered reduced velocity. Figure 5-26 shows the first five modes of vibrations used in the study. Table 5-3 reports the vibration frequencies along with the modal damping at U_{red} = 5.6. The forces distribution in the cross-wind direction and the 3D model are shown in Figure 5-27 clearly identifying the response indicators that will be examined.

$$V^h = V_{ref}\left(\frac{h}{h_{ref}}\right)^{\alpha} \qquad 5\text{-}9$$

$$C_{ad}^{n,l} = \frac{-H_1^* \rho D^2 \omega_n}{2} \quad 5\text{-}10$$

$$C_{ad}^{n} = \sum_{i=1}^{i=l} \varphi_{n,y}^{T} \begin{bmatrix} C_{ad}^{n,1} & 0 & 0 \\ 0 & C_{ad}^{n,i} & 0 \\ 0 & 0 & C_{ad}^{n,l} \end{bmatrix} \varphi_{n,y} \quad 5\text{-}11$$

$$C_{ad}^{n} = \sum_{i=1}^{i=l} \varphi_{n,y,i}^{2} \, C_{ad}^{n,i} \quad 5\text{-}12$$

$$\xi_{ad}^{n} = \frac{C_{ad}^{n}}{2M_n \omega_n} \quad 5\text{-}13$$

Mode 1	Mode 2
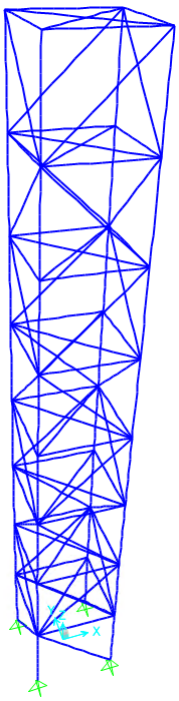	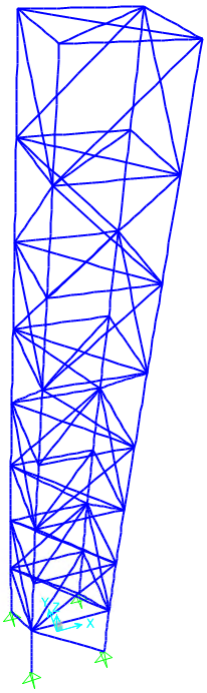
Mode 3	Mode 4
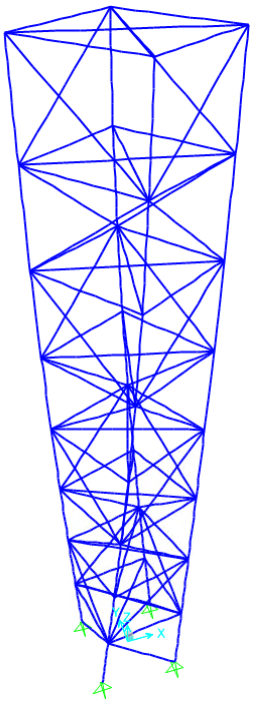	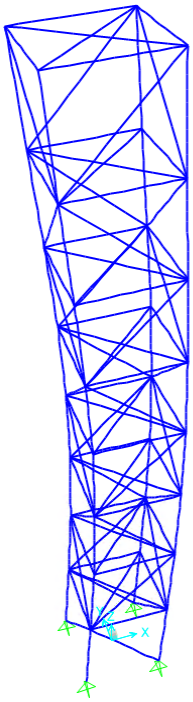

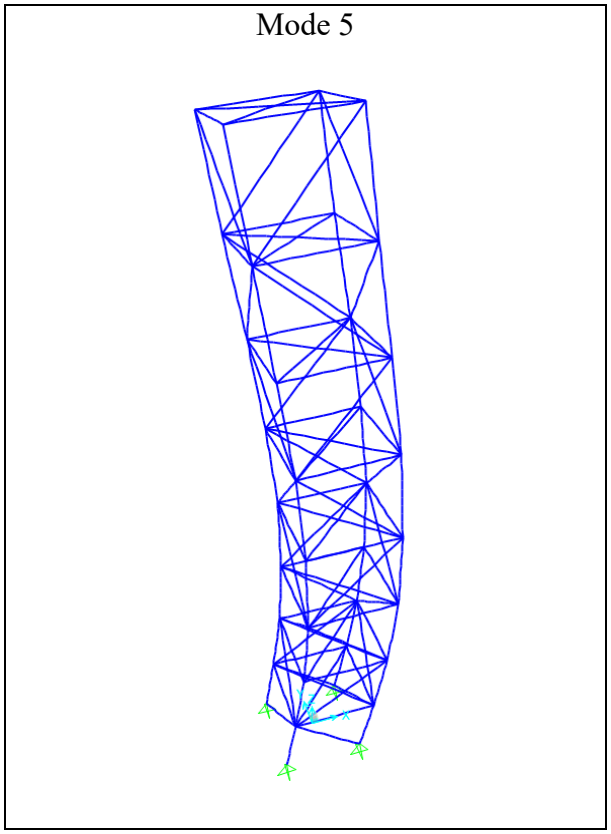

Figure 5-26 Modes of vibration

Table 5-3 Modes of vibrations and their characteristics

Mode	Frequency (Hz)	Modal mass[3], M_n	Modal Damping (ξ_{ad}^n) at U_{red} = 5.6	Structural Damping (ξ_{st}^n)
1	0.785	1	3.36%	1%
2	0.79	1	3.36%	1%
3	1.34	1	1.15%	1.15%
4	2.88	1	4.39%	1.96%
5	2.94	1	4.43%	2%

[3] Due to mode shape normalization, modal mass (Mn) is set to 1 and all modes shapes are adjusted in SAP to reflect that.

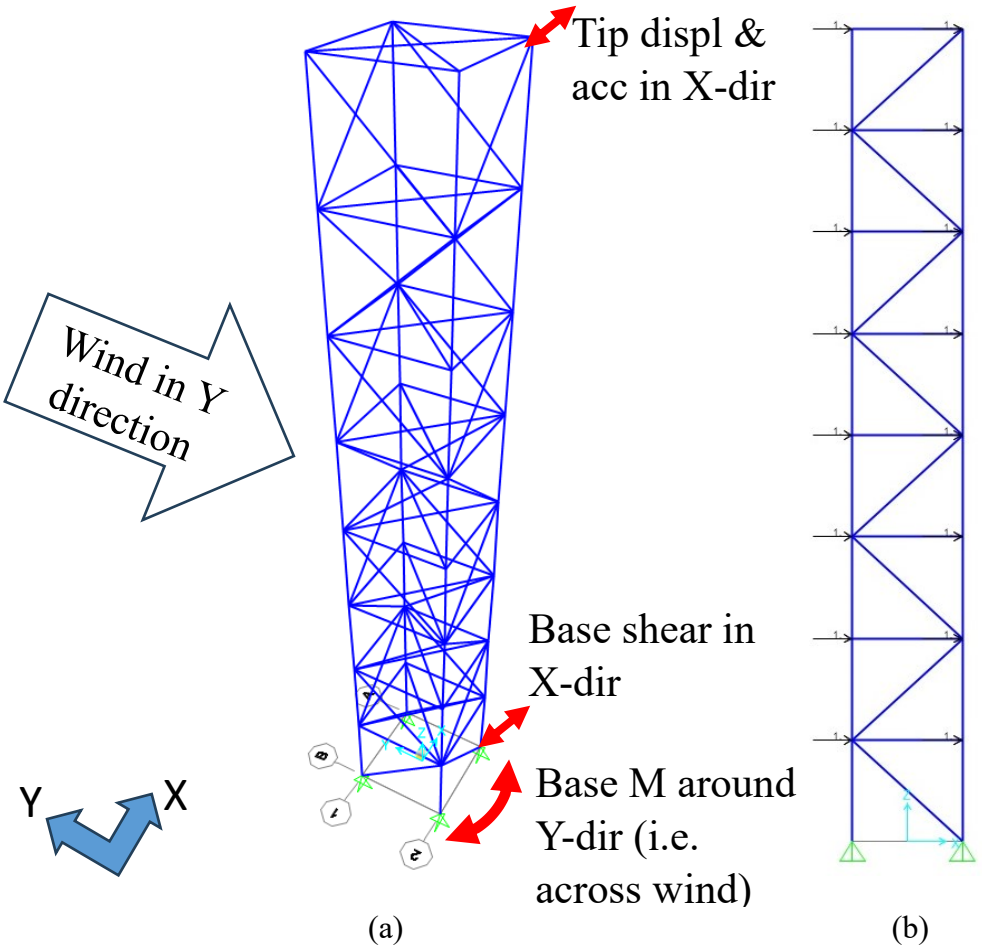

Figure 5-27 lattice structure modeled (a) 3D (b) Side view showing the cross-wind force distribution

5.5.2.4 Results

The time history of the lift forces from the CFD simulation was used to run a time history analysis using modal superposition for the first five modes of vibration in SAP2000 v25.2.0 at 10 different reduced velocities. Two series of analysis were conducted: one with structural damping only and the other one with both structural and aerodynamic damping. Steps followed are organized in the flow chart of Figure 5-28. As indicated in Figure 5-27 results are for crosswind forces (applied in X direction), as interest is in the behaviour resulting from H_1^*.

An example of the time history of the lift force obtained from CFD simulations at U_{red} = 5.6 is shown in Figure 5-29. The time history of the response at the top of the model at U_{red} = 5.6, including displacement and acceleration in the applied force direction (X cross-wind) as well

as base shear along X and base overturning moment around Y are shown in Figure 5-30 and Figure 5-31 for the case of using only structural damping (curves in red) and on using the sum of the structural and AD damping (curves in blue), respectively.

Comparisons of the peak responses are shown in Figure 5-32. On taking the aerodynamic damping into consideration all the responses for the lattice structure were reduced, for the range of studied velocities, which is in contrast with the simulated response of the square cylinder considered alone. The least reduction was in the base overturning moment Y and the maximum was in the displacement X and base shear in X. It is seen that the reductions observed for U_{red} = 5.6 are not as important as those obtained in the range of 6 to 8 where the lift forces are most affected by the aerodynamic damping. The response reduction ranged from 40% to 70% for the displacement in the force direction, as shown in Table 5-4. Additionally, the least reduction in all the response indicators was encountered at the maximum velocity studied. This reduction in response is obtained because, for the range of reduced velocities studied, the aerodynamic damping was always positive, therefore adding to the structural damping and hence decreasing the vibrations. It could be concluded that for the solidity ratio studied (SR = 0.23) accounting for the flexibility of the structure added to its stability and lessened the vibrations. In this particular case, the results are for a smooth flow at turbulence intensity I = 2%. These conclusions comply with the finding by Scruton, that as long as the solidity is not excessively high, lattice structures exhibit positive damping when subjected to wind [7].

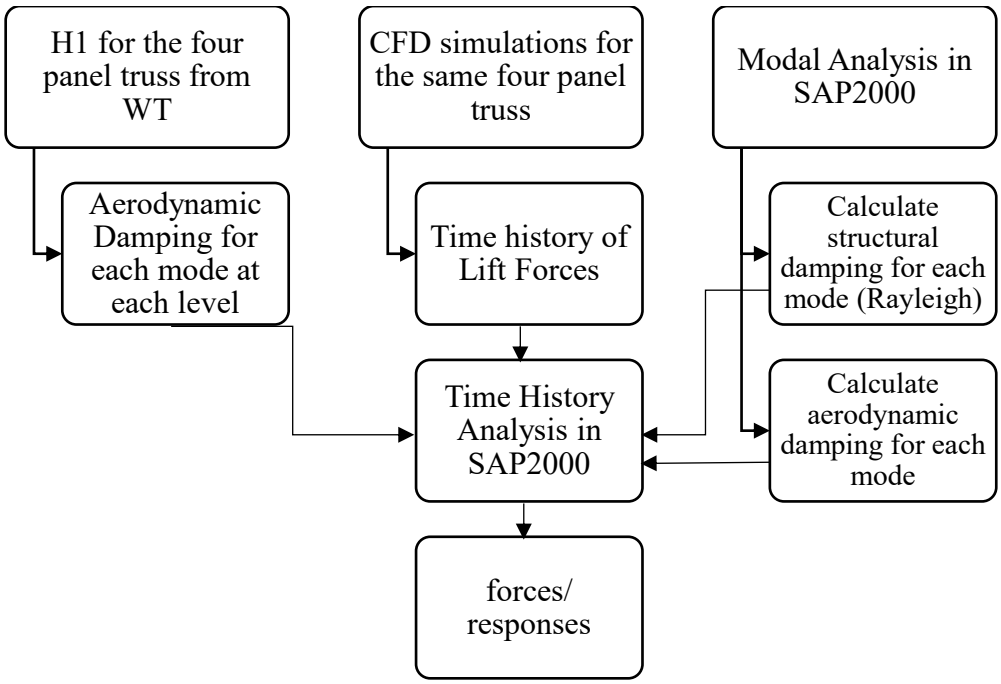

Figure 5-28 Flow chart for calculation of displacement for the lattice structure

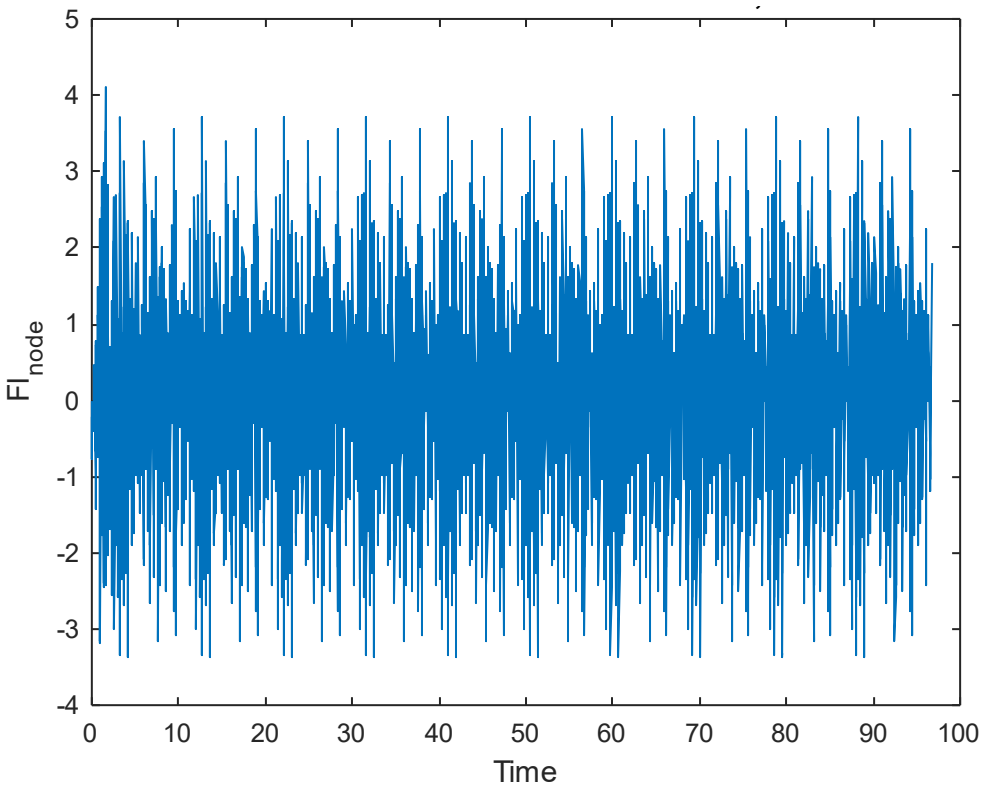

Figure 5-29 Time history of Lift force at one node at the top of the truss at U_{red} = 5.6.

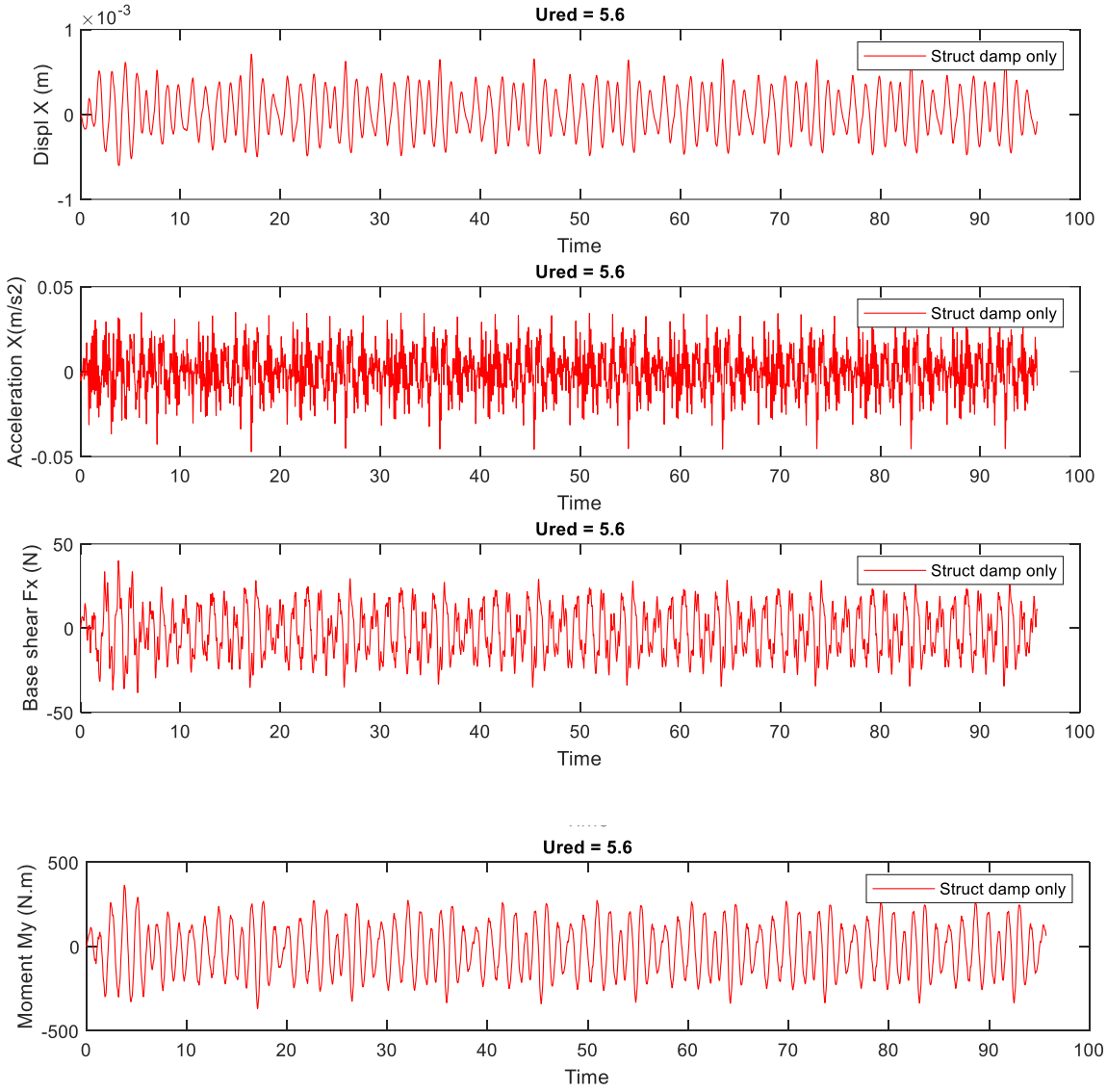

Figure 5-30 Time history of response at top of the lattice structure and base reactions with structural damping only at U_{red} = 5.6.

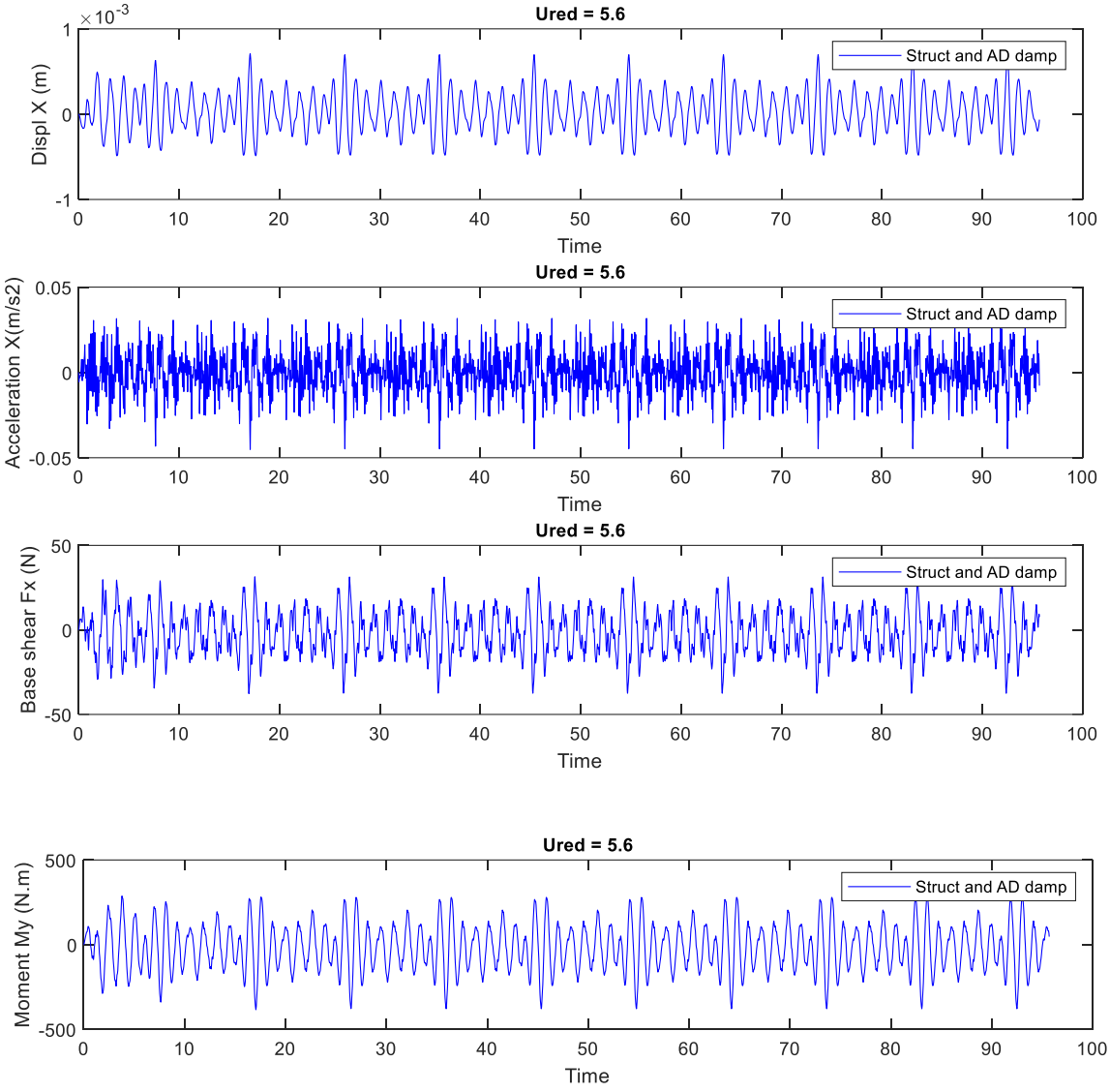

Figure 5-31 Time history of response at top of the lattice structure and base reactions with structural and aerodynamic damping at U_{red} = 5.6.

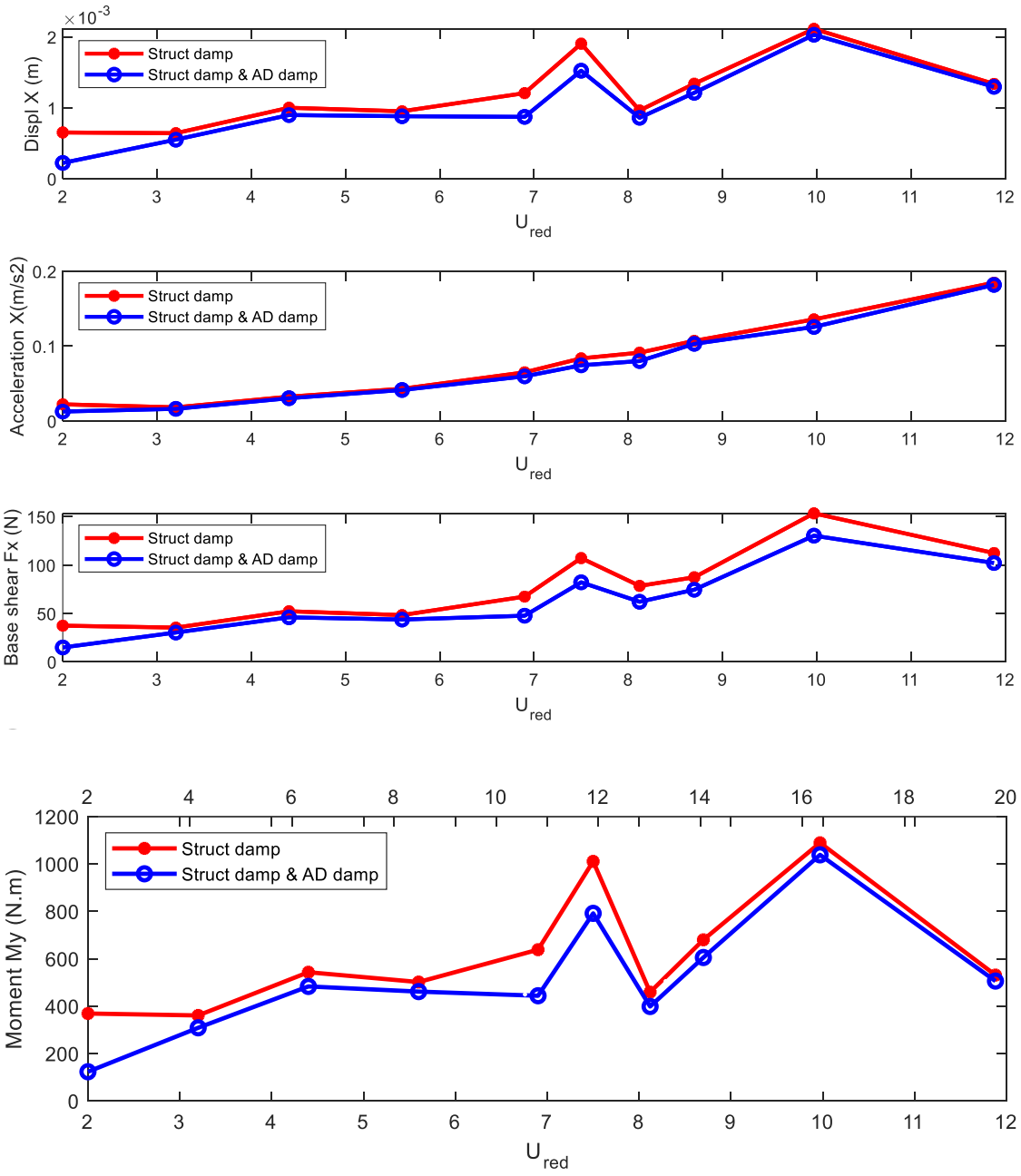

Figure 5-32 Comparison of the peak response at top of the lattice structure and the base reaction.

Table 5-4 Percent of reduction in Peak Response on adding AD damping

Ured	3.2	4.4	5.6	6.9	7.5	8.1	8.7	10	11.9
Displ X	45.6	66.1	38.0	79.2	67.7	71.5	65.7	49.1	37.7
Acc X	46.6	64.6	49.0	56.1	52.2	61.2	57.3	54.8	29.9
Base shear X	48.8	66.0	51.2	64.7	61.3	62.1	59.1	54.7	30.2
Base Moment Y	3.7	1.8	2.3	2.7	0.4	1.0	1.8	1.6	0.7

5.6 Conclusion

This study showcased the practicality of the suggested approach, which aims at determining whether the flexibility of structures has potentially a significant influence on the wind loads acting on them due to fluid-structure interactions. The study was conducted in three stages. First, wind tunnel experiments carried out at Toronto Metropolitan University were described and the results were presented. It was concluded that the aerodynamic derivative H_1^* could be reproduced with good accuracy for the square cylinder with the method used. Subsequently, using the same set-up and procedures the aerodynamic derivative H_1^* was determined for two structural models that were not studied or openly reported before, namely a member with an equal legged angle cross section and a four-panel truss with different solidity ratios. Secondly, computational fluid dynamics simulations were done and validated for both models. Thirdly, both outputs (aerodynamic forces and H_1^*) were used to study the square cylinder as a single-degree-of-freedom system and a lattice structure through a time history structural dynamics analysis in SAP2000 V25.2.0. Cross-wind displacement, acceleration, base shear forces and moments are presented in Figure 5-30, Figure 5-31 and Figure 5-32. The following conclusions can be drawn from the results obtained from the developed simulations.

- Regarding the studied square cylinder, the responses increased at the vortex-induced vibrations range of velocities and at reduced velocities higher than 20, with a percentage that varies between 15-70% at the former to between 10-40% at the latter.
- In contrast, for the lattice structure studied at solidity ratio 0.23, the responses/forces were reduced in comparison with the case where the flexibility was not taken into consideration with a percentage that varies as shown in Table 5-4.

It was found from the simulations that the interaction of the flexible structure with wind has considerable effects on the response which implies a change in forces. While several factors govern the magnifying or diminishing of the forces, the most important are the damping forces. Once the negative aerodynamic damping exceeds the structural damping the amplitude of oscillations grows until usual inherent nonlinearities in the system restrain the motion which subjects the structure to fatigue, or oscillations grow until structural collapse. The lattice structure tested was provided as a single complete example to demonstrate the feasibility of the proposed methodology.

Further work would be required to;

- Validate the methodology with complete FSI simulation of the lattice structure which was not possible with the current computational resources.
- Investigate different solidity ratios and flexibilities to draw better generalized conclusions as higher solidity ratios might be prone to increase in the exciting forces similar to what was experienced with the square cylinder.
- Explore the effect of turbulence on fluid structure interactions.

5.7 Acknowledgement

The authors would like to acknowledge the support of the National Science and Engineering Research Council of Canada for its financial support.

REFERENCES

1. Bearman, P.W. and E.D. Obasaju, *An experimental study of pressure fluctuations on fixed and oscillating square-section cylinders.* Journal of Fluid Mechanics, 1982. **119**: p. 297-321.
2. Ermshaus, R., E. Naudascher, and E. Obasaju, *Vortex-induced streamwise oscillation of prisms in a uniform stream of different incidence*, in *Bericht des Sonderforschungsbereichs 210*. 1986, Universität Karlsruhe Karlsruhe, Germany.
3. Naudascher, E., *Flow-induced streamwise vibrations of structures.* Journal of Fluids and Structures, 1987. **1**(3): p. 265-298.
4. P. W. Bearman, I.S.G., D. J. Maull, G. V. Parkinson, *Experiments on flow-induced vibration of a square-section cylinder.* Journal of Fluids and Structures, 1987. **1**(1): p. 19-34.
5. Bearman, P.W. and S.C. Luo, *Investigation of the aerodynamic instability of a square-section cylinder by forced oscillation.* Journal of Fluids and Structures, 1988. **2**(2): p. 161-176.
6. Okajima, A. and K. Kitajima, *Numerical study on aeroelastic instability of cylinders with a circular and rectangular cross-section.* Journal of Wind Engineering and Industrial Aerodynamics, 1993. **46-47**: p. 541-550.
7. He, T., D. Zhou, and Y. Bao, *Combined interface boundary condition method for fluid–rigid body interaction.* Computer Methods in Applied Mechanics and Engineering, 2012. **223-224**: p. 81-102.
8. Hemon, P., *Large galloping oscillations of a square section cylinder in wind tunnel.* Flow-Induced Vibrations, FIV2012, Dublin, Ireland, July, 2012: p. 3-6.

9. Sen, S. and S. Mittal, *Effect of mass ratio on free vibrations of a square cylinder at low Reynolds numbers.* Journal of Fluids and Structures, 2015. **54**(Supplement C): p. 661-678.

10. Carassale, L., A. Freda, and L. Banfi, *Motion-excited forces acting on a square prism: a qualitative analysis*. 2015.

11. Sourav, K. and S. Sen, *Transition of VIV-only motion of a square cylinder to combined VIV and galloping at low Reynolds numbers.* Ocean Engineering, 2019. **187**: p. 106208.

12. Parkinson, G., *Phenomena and modelling of flow-induced vibrations of bluff bodies.* Progress in Aerospace Sciences, 1989. **26**(2): p. 169-224.

13. Davenport, A.G., *The treatment of wind loading on tall buildings*, in *tall buildings*, A. Coull and B.S. Smith, Editors. 1967, Pergamon. p. 3-45.

14. Obasaju, E.D., R. Ermshaus, and E. Naudascher, *Vortex-induced streamwise oscillations of a square-section cylinder in a uniform stream.* Journal of Fluid Mechanics, 1990. **213**: p. 171-189.

15. Haan, F.L. and A. Kareem, *Anatomy of Turbulence Effects on the Aerodynamics of an Oscillating Prism.* Journal of Engineering Mechanics, 2009. **135**(9): p. 987-999.

16. Slater, J.E., *Aeroelastic instability of a structural angle section*. 1969, University of British Columbia.

17. Canada, N.B.C.o., *User's guide o f NBCC 2015 commentary I*. 2015.

18. Gobran, Y., G. McClure, and H. Aboshosha, *Determination of aerodynamic derivative for one degree of freedom square cylinder using large eddy simulation.* Results in Engineering, 2022. **16**: p. 100620.

19. Ghazal, T., et al., *Flow-conditioning of a subsonic wind tunnel to model boundary layer flows.* Wind and Structures, 2020. **30**(4): p. 339-366.

20. Nakayama, A., D. Okamoto, and H. Takeda, *Large-eddy simulation of flows past complex truss structures.* Journal of Wind Engineering and Industrial Aerodynamics, 2010. **98**(3): p. 133-144.

21. Amandolese, X. and P. Hémon, *Vortex induced vibration of a square cylinder in wind tunnel.* Comptes Rendus Mécanique, 2010. **338**(1): p. 12-17.

22. Scruton, C., *On the Wind-excited Oscillations of Stacks, Towers and Masts*. 1963.

CHAPTER 6 RESEARCH SUMMARY

This thesis demonstrated the applicability of the proposed methodology to assess the impact of structural flexibility of strongly bluff bodies on the wind load experienced by the structure. There are several methods to achieve this goal which are wind tunnel testing, computational fluid dynamics, structural analysis and analytical methods. In this study the approach was to use a combination of the three methods. The solution was divided into three steps: i) the determination of the aerodynamic coefficients, ii) the estimation of the aerodynamic damping and finally iii) the assessment of the response by dynamic structural analysis.

Chapter three discussed the determination of the aerodynamic coefficients through computational fluid dynamics (CFD) simulations using commercial software ANSYS FLUENT. In this chapter, extremely bluff bodies were of concern. Since the dynamics of the flow around bluff body is complex, involving impingement, separation, free shear layers, reattachment, circulation, and vortices. Fine grid discretization is essential to analyze such flow fields accurately using CFD. Computational Fluid Dynamics (CFD) has become widely used in engineering applications, including environmental engineering, hydraulics, and aeronautics, enabling the study of wind engineering problems like flow-fields around buildings and structures.

CFD involves solving the governing equations of fluid dynamics (mass, momentum, and energy) to analyze fluid flow around a body. In the case of incompressible flows (Mach number below 0.3, our case), the equation of state (temperature) is neglected. Although CFD is a valuable tool, its effectiveness is enhanced when combined with experiments, particularly in structural engineering applications. Wind-tunnel testing plays a critical role in validating CFD models, while CFD can secure comprehensive flow field data for all significant parameters and boundaries. Computational wind engineering (CWE) offers the advantage of complete control

over boundary conditions and facilitates efficient parametric studies to assess various design configurations. The accuracy and reliability of CWE simulations are essential, requiring verification and validation studies. To ensure accuracy, computational models should be verified and validated against wind tunnel tests and existing numerical simulations in the literature. Such validation is crucial for improving the reliability of CFD predictions in wind engineering studies.

Chapter three focused on developing a CFD model that was thoroughly validated and suitable for use as a foundation for subsequent models. It discussed selecting the right parameters such as the turbulence model, grid, boundary conditions, time step…. etc. Turbulence models are critical in CFD, and the large eddy simulation (LES) model is often preferred for simulating wind flows around bluff bodies. As, LES resolves large-scale eddies and models small-scale ones using an eddy viscosity model which was the Smagorinsky-Lilly sub-grid scale model in the case studied. Assigning proper boundary conditions is crucial for reliable results, including inflow, outflow, transverse, top, and bottom conditions, as well as solid/fluid boundaries which were set based on the problem at hand. The domain size was determined based on best practice guidelines. In addition, Solution errors in CFD models arise from numerical modeling errors and computational errors, which can be minimized through grid independence studies and higher-order approximations. Eventually, a structured mesh was used, and a grid study was performed where two meshes were tested. The simulations were run at a Reynolds number of 34000, and statistics were used to validate the aerodynamic forces, showing good agreement with experimental and numerical results for drag, lift, and moment coefficients at different angles of attack. The model's capability to correctly calculate transverse force coefficients was confirmed, demonstrating its potential for use in fluid-structure interaction models. The Strouhal number and velocity profiles also matched well with experimental values, indicating

the accuracy of the computations. Overall, the CFD model provided satisfactory results and showed promise for further applications in wind engineering studies.

The next section in chapter three explored the use of Computational Fluid Dynamics (CFD) simulations to assess the aerodynamic derivatives (ADs) and Wind Structure Interaction (WSI) response of free vibrating bluff bodies. The ADs are essential for assessing motion-induced forces on flexible structures. The motion-induced forces are determined from Scanlan equations based on the body vibration and predetermined aerodynamic derivatives. Forced or free vibration wind tunnel tests or CFD simulations are used to obtain these aerodynamic derivatives. The study focuses on evaluating the ADs for the bluff bodies through the free vibration method, as it is considered more suitable for the cross-sections under consideration.

The focus was on a three-dimensional simulation of a rigid square cylinder that is elastically supported and allowed to move only in the transverse direction under wind loading, while restricting its motion in the stream-wise and rotational directions. The flutter derivatives are estimated through a free vibration method, where the square cylinder is pushed to a displacement, and then fluid simulations are run with the cylinder stationary. Subsequently, the cylinder is released to vibrate freely, and the aerodynamic damping is calculated at different reduced velocities. The aerodynamic derivative H_1^* is then determined from the aerodynamic damping.

The fluid-structure interaction was simulated using the weak coupling method, where the CFD model and the structural dynamics model were interchangeably solved at each time step. The fluid-structure interaction is governed by Navier-Stokes equations in Arbitrary Lagrangian Eulerian (ALE) fluid approximation, and the mesh deformation was achieved through the displacement-based Lagrangian approach. The square cylinder motion was simulated as a single degree of freedom motion which was governed by the Newmark method, providing

accurate and stable results for single-degree-of-freedom systems. The results of the numerical estimation of H_1^* aerodynamic derivative, were compared with wind tunnel test results, and a good agreement was observed. The approach was further validated against different Scruton numbers, mass ratios, and Reynolds numbers, showing consistent agreement with experimental data. The study concluded that the approach is valid.

In the last section of the third chapter, the use of aerodynamic derivatives (ADs) to determine the response of freely vibrating bluff bodies, specifically a square cylinder, was explored. The aerodynamic derivative H_1^* obtained from previous simulations was used to calculate the aerodynamic damping with the knowledge of its mass, characteristic length, and span. Afterwards, the Newmark method was used to determine the amplitude of vibration for the elastically supported single degree of freedom square cylinder, using total damping. Where the total damping is the summation of aerodynamic and structural damping.

Overall, the third chapter demonstrated the capability of the CFD model to accurately estimate flutter derivatives in fluid-structure interaction problems involving square cylinders vibrating in the cross-stream direction only. The third chapter also addressed the complexity of forces on bluff bodies exposed to wind and highlighted the importance of identifying aerodynamic derivatives for assessing motion-induced forces on flexible structures and the applicability of utilising the flutter derivatives to estimate vibration amplitudes for square cross-section bodies i.e., extremely bluff bodies. Furthermore, the latter method was utilized to offer supplementary validation for the extracted aerodynamic derivative. This validation involved a comparison of vibration amplitudes with those obtained from free vibration experiments conducted on both the square cylinder and equal-legged angle cross-section member. Since wind tunnel experiments are essential for the validation of CFD simulations and given the fact that there are rare sources in the literature to validate the extracted aerodynamic derivatives for the angle shape and the four-panel truss. In addition to the time consuming CFD simulations that would

be encountered on handling a more complex structure (i.e., the four-panel truss). The necessity for wind tunnel experiments arose.

Subsequently chapter four describes wind tunnel experiments held to determine aerodynamic derivatives (ADs) using the free vibrations technique. The experimental work was conducted in the wind tunnel facility at Toronto Metropolitan University (former Ryerson University, Toronto). The wind tunnel is a closed-loop system with a large fan that can operate at speeds ranging from 4 m/s to 30 m/s. The test section has a cross-section of 91x91 cm. The testing setup for free vibrations was conducted for the first time in this wind tunnel facility by the authors. Therefore, the setup was designed to fit the facility. It consisted of a rigid frame that was fixed to the tunnel wall. The model was supported on two arms that were supported on springs which were connected to load cells. The arm length was designed to be long enough to minimize the motion in the rotational direction and a longitudinal bar was added to restrict the motion in the streamwise direction.

Three models were tested representing elements and parts of lattice structures: a cylinder with square cross-sections, a member with equal-legged angle cross section, and a four-panel lattice structure (W Truss). The first model (cylinder with square cross section) has been studied before, but using the forced vibration method, and was repeated for validation. The other two models (member with equal leg angled cross sections and lattice structure) are rarely covered in literature.

The models were assumed to be rigid where they were supported on springs to observe potential fluid-structure interactions. The models were allowed to move only in the cross-stream direction. The dynamic properties of the system with the model were determined through static tests, and the structural damping was assessed through free vibration tests. The testing procedure involved pulling the model to an initial displacement and releasing it to freely

vibrate, this was repeated for each reduced velocity tested. The forces and displacements were measured during the vibrations through load cells attached to the springs. For each model, the aerodynamic damping was calculated from the vibrations time history and consequently the aerodynamic derivative H_1^* was found at each reduced velocity. The square cylinder was tested at zero angle of attack while, the angle cross-section was tested at two angles of attack (45 and 135 degrees). Whereas, the four-panel truss was tested at two different solidity ratios, creating a library for H_1^* derivative that could be used later to assess the response of the structural model.

In chapter five the main objective of the study was achieved, and the steps followed were summed up. Additionally, the chapter also includes an introduction to various types of vibrations experienced by structures and a literature review on the effect of flexibility on aeroelastic forces. The subsequent sections detail the wind tunnel experiments, CFD simulations, and dynamic analysis procedures, along with the corresponding results and validation.

It mainly presents a wide-ranging study on the effect of structural flexibility on wind loading through wind tunnel experiments, computational fluid dynamics (CFD), and dynamic numerical analysis. Previous studies have shown potential changes in wind forces due to dynamic instability, but this study extends the investigation to lattice structures. This study demonstrates the importance of accounting for structural flexibility in wind loading analysis. It provides valuable insights into the behavior of flexible structures under wind load, contributing to better design and understanding of fluid-structure interaction.

Three models were tested in wind tunnel to extract the aerodynamic damping as explained in chapter four and they were also simulated in CFD to extract the aerodynamic coefficients, similar to what was explained in chapter three which was the base for other models studied in

this chapter. The models were a square cylinder, an equal legged angle cross-section member, and a lattice structure composed of these elements.

The fifth chapter starts with summarizing the wind tunnel tests performed in chapter three. Then, wind flow around an equal-legged angle cross-section was simulated by CFD simulations using ANSYS FLUENT, following the same guidelines as those used to simulate the square cross-section cylinder. The angle was tested at various angles of attack and at different velocities i.e., different Reynolds numbers. Mean drag coefficient as well as R.M.S of the lift coefficient were obtained. The coefficients showed very good agreement with the literature. Additionally, the mean drag coefficient and R.M.S lift coefficient for a range of Reynolds numbers for the stationary angle member were found to be constant, aligning well with the literature.

The four-panel W Truss with square cross section and square elements was simulated at a solidity ratio of 0.23 for smooth and turbulent flows. The drag coefficient for the square lattice structure compared well with the calculated one according to NBC and with results from other studies. Additionally, the CFD simulations were run at a range of velocities i.e., Reynolds numbers and the lift force coefficient was boosted for turbulent flow.

Overall, the CFD simulations provided data on the aerodynamic forces and coefficients for the tested cross sections, complementing the wind tunnel experimental results and contributing to a comprehensive understanding of fluid-structure interaction and wind loading.

In the dynamic analysis section, the output from CFD simulations (aerodynamic coefficients) and wind tunnel experiments (aerodynamic damping) were used to find the response of the models under study. The aerodynamic damping values obtained from wind tunnel experiments were used in structural dynamic analysis to study the effect of adding aerodynamic damping on the response of different structural elements and a full lattice structure. That was done

through a finite element model of the square cylinder and a lattice structure composed of the four-panel lattice structure tested earlier. A time history analysis, using the aerodynamic coefficients, for the structural dynamics model was done to assess the structural response and thus the impact of flexibility on wind loading.

To validate the method the square cylinder was first simulated as a single degree of freedom system, using mass, stiffness, and structural damping similar to the those used by Amandolese 2010. Aerodynamic damping was calculated with the knowledge of the aerodynamic derivative H_1^*. Then, time history forces were estimated from CFD. The response R.M.S vibrations matched well with the ones reported in the literature therefore the concept used was valid and could be extended to more structural models. Also, the displacements were calculated with and without the effect of aerodynamic damping and results showed that displacements were amplified at vortex-induced vibrations (VIV) range of velocities and at high reduced velocities ($U_{red} > 20$) when considering aerodynamic damping.

A lattice structure composed of the four-panel truss was used in this study. First modal analysis of the lattice structure was performed to determine its natural modes of vibration and their frequencies, only the first five modes of vibrations were considered. The overall aerodynamic damping was calculated for the whole structure with the knowledge of the aerodynamic damping of its individual parts. The structural damping was assumed to be 1% for the 1st fundamental sway mode and equivalent structural damping for higher modes was calculated using Rayleigh damping method. Finally, time history analysis was run for the structure one time with adding only the structural damping and another time with both the structural and aerodynamic damping. Comparing the results showed that the aerodynamic damping suppressed vibrations for the range of reduced velocities studied, contributing to the stability, and decreasing vibrations of the structure.

In conclusion, results indicate that considering structural flexibility is crucial, as fluid-structure interactions have significant effects on the response. In the cases presented here the square cylinder amplified the response, while the lattice structure diminished it.

CHAPTER 7 SUMMARY OF CONCLUSIONS

The conclusions drawn from the study are as follows:

1. The methodology originally used to study aerodynamic wind forces on streamlined structures was adapted to be used for flexible strongly bluff bodies, namely the square cylinder and lattice structure. This adapted approach was employed to investigate the impact of aeroelasticity on these exposed structures.

2. The flexibility of structures does have an impact on wind loads acting on them and such wind-structure interactions can be significant. In the cases studied here:for the square cylinder, the response was boosted at vortex induced vibrations (VIV) and high reduced velocities, while for the lattice structure at solidity ratio 0.23, the motion and internal forces were reduced compared to when flexibility was not considered.

3. The free vibrations setup in the wind tunnel proved to be effective in deriving the aerodynamic derivative H_1^* for single-degree-of-freedom strongly bluff bodies and systems.

4. For the lattice structure studied, a library of H_1^* derivative was built for the W-shaped truss in a range of reduced wind velocities. The response of the lattice structure with a solidity ratio of 0.23, was notably diminished when compared to scenarios where flexibility was not factored in, with a reduction ranging from 30% to 60%.

5. For the square cylinder, the response was increased during the vortex-induced vibrations velocity range and at reduced velocities surpassing 20. The percentage of increase ranged from 15% to 70% in the former case and from 10% to 40% in the latter case.

6. Numerical 3D large eddy simulation (LES) turbulent modelling is reliable for estimating aerodynamic derivatives for single-degree-of-freedom systems.

7. The free vibration method for identifying aerodynamic derivatives for strongly bluff bodies is viable and yields comparable results to literature, making it useful in early design stages.

8. The Scanlan model aerodynamic derivatives method can predict the amplitude of vibration at the same Scruton number at which the derivatives were initially identified.

9. The study demonstrates the potential of using aerodynamic derivatives to predict the response of freely vibrating strongly bluff bodies to wind flow, providing valuable insights for structural design.

10. The method used to estimate the R.M.S vibrations with the knowledge of H_1^* was valid and provided comparable results to literature, making it suitable for early design stages.

Overall, the study revealed that the interaction of flexible structures with wind can significantly affect their internal forces. To draw more comprehensive and generalized conclusions for space trusses, further investigations are necessary, exploring various solidity ratios and flexibilities. Higher solidity ratios may lead to an increase in exciting forces, similar to what was observed with the square cylinder, if the vortex shedding frequencies are excited. Therefore, additional research is needed to gain a deeper understanding of these effects.

REFERENCES

1. Gobran, Y., G. McClure, and H. Aboshosha, *Determination of aerodynamic derivative for one degree of freedom square cylinder using large eddy simulation.* Results in Engineering, 2022. **16**: p. 100620.
2. Šarkić Glumac, A., R. Höffer, and S. Brčić, *Identification of flutter derivatives by forced vibration tests.* Građevinar, 2017. **69**(04.): p. 267-280.
3. Washizu, K., Ohya, A., Otsuki, Y., Fujii, K., *Aeroelastic instability of rectangular cylinders in a torsional mode due to a transverse wind.* Journal of Sound and Vibration, 1980. **72**(4): p. 507-521.
4. Nakamura, Y., *Recent research into bluff-body flutter.* Journal of Wind Engineering and Industrial Aerodynamics, 1990. **33**(1): p. 1-10.
5. Su, N., S. Peng, and N. Hong, *Universal simplified spectral models and closed form solutions to the wind-induced responses for high-rise structures.* Results in Engineering, 2021. **10**: p. 100230.
6. Scanlan, R.H. and J. Tomo, *Air foil and bridge deck flutter derivatives.* Journal of Soil Mechanics & Foundations Div, 1971.
7. Scruton, C., *On the wind-excited oscillations of stacks, towers and masts*. 1963.
8. Slater, J.E., *Aeroelastic instability of a structural angle section*. 1969, University of British Columbia.
9. Gao, G. and L. Zhu, *Measurement and verification of unsteady galloping force on a rectangular 2:1 cylinder.* Journal of Wind Engineering and Industrial Aerodynamics, 2016. **157**(Supplement C): p. 76-94.
10. S. Murakami*, A.M., *On turbulent vortex shedding flow past 2D square cylinder predicted by CFD.* Journal of Wind Engineering and Industrial Aerodynamics, 1995: p. 191-211.
11. Scanlan, R.H. and E. Simiu, *Winds Effects on Structures: Fundamentals and Applications to Design*. 1996, John Wiley & Sons Incorporated.
12. Bearman, P.W. and E.D. Obasaju, *An experimental study of pressure fluctuations on fixed and oscillating square-section cylinders.* Journal of Fluid Mechanics, 1982. **119**: p. 297-321.
13. Obasaju, E.D., R. Ermshaus, and E. Naudascher, *Vortex-induced streamwise oscillations of a square-section cylinder in a uniform stream.* Journal of Fluid Mechanics, 1990. **213**: p. 171-189.
14. Naudascher, E., *Flow-induced streamwise vibrations of structures.* Journal of Fluids and Structures, 1987. **1**(3): p. 265-298.
15. Murakami, S., *Current status and future trends in computational wind engineering.* Journal of Wind Engineering and Industrial Aerodynamics, 1997. **67**: p. 3-34.
16. Ricci, M.P., L., de Miranda, S., Ubertini, F., *Flow field around a 5:1 rectangular cylinder using LES: Influence of inflow turbulence conditions, spanwise domain size and their interaction.* Computers & Fluids, 2017. **149**: p. 181-193.
17. Blocken, B., *50 years of Computational Wind Engineering: Past, present and future.* Journal of Wind Engineering and Industrial Aerodynamics, 2014. **129**: p. 69-102.
18. Zhai Zhiqiang John, Z.Z., Zhang Wei, Chen Qingyan Yan, *Evaluation of various turbulence models in predicting airflow and turbulence in enclosed environments by CFD: Part 1—summary of prevalent turbulence models.* HVAC&R Research, 2007. **13**(6): p. 853-870.
19. Rodi, W., *Comparison of LES and RANS calculations of the flow around bluff bodies.* Journal of Wind Engineering and Industrial Aerodynamics, 1997. **69**: p. 55-75.

20. SMAGORINSKY, J., *General circulation experiments with the primitive equations: I. The basic experiment.* Monthly Weather Review, 1963. **91**(3): p. 99-164.
21. Murakami, S., *Overview of turbulence models applied in CWE–1997.* Journal of Wind Engineering and Industrial Aerodynamics, 1998. **74**: p. 1-24.
22. Germano, M., et al., *A dynamic subgrid-scale eddy viscosity model.* Physics of Fluids A: Fluid Dynamics, 1991. **3**(7): p. 1760-1765.
23. Lilly, D.K., *A proposed modification of the Germano subgrid-scale closure method.* Physics of Fluids A: Fluid Dynamics, 1992. **4**(3): p. 633-635.
24. *ANSYS Fluent V18.1*. ANSYS, Inc.
25. Kim, S.-E., *Large eddy simulation using an unstructured mesh based finite-volume solver*. 2004.
26. John, V., *Large eddy simulation of turbulent incompressible flows: analytical and numerical results for a class of LES models*. Vol. 34. 2003: Springer Science & Business Media.
27. Tamura, T., K. Nozawa, and K. Kondo, *AIJ guide for numerical prediction of wind loads on buildings.* Journal of Wind Engineering and Industrial Aerodynamics, 2008. **96**(10-11): p. 1974-1984.
28. Shah, K.B. and J.H. Ferziger, *A fluid mechanicians view of wind engineering: Large eddy simulation of flow past a cubic obstacle.* Journal of Wind Engineering and Industrial Aerodynamics, 1997. **67-68**: p. 211-224.
29. Rodi, W., *Large eddy simulation of the flow past bluff bodies.* 2002.
30. Xie, Z. and I.P. Castro, *LES and RANS for Turbulent Flow over Arrays of Wall-Mounted Obstacles.* Flow, Turbulence and Combustion, 2006. **76**(3): p. 291-312.
31. Parente, A., R. Longo, and M. Ferrarotti, *cfd boundary conditions, turbulence models and dispersion study for flows around obstacles*, in *VKI letcure series*. 2017.
32. de Miranda, S., et al., *On the identification of flutter derivatives of bridge decks via RANS turbulence models: Benchmarking on rectangular prisms.* Engineering Structures, 2014. **76**: p. 359-370.
33. Montorfano, A., F. Piscaglia, and G. Ferrari, *Inlet boundary conditions for incompressible LES: A comparative study.* Mathematical and Computer Modelling, 2013. **57**(7): p. 1640-1647.
34. Georgiadis, N.J., D.P. Rizzetta, and C. Fureby, *Large-eddy simulation: current capabilities, recommended practices, and future research.* AIAA journal, 2010. **48**(8): p. 1772-1784.
35. Franke, J., *Best practice guideline for the CFD simulation of flows in the urban environment*. 2007: Meteorological Inst.
36. Murakami, S., *Computational wind engineering.* Journal of Wind Engineering and Industrial Aerodynamics, 1990. **36**: p. 517-538.
37. Francisco Toja-Silva, C.P., Oscar Lopez-Garcia, Jorge Navarro, Ignacio Cruz, *Roof region dependent wind potential assessment with different RANS turbulence models.* Journal of Wind Engineering and Industrial Aerodynamics, 2015. **142**: p. 258-271.
38. Dhunny, A.Z., M.R. Lollchund, and S.D.D.V. Rughooputh, *Wind energy evaluation for a highly complex terrain using computational fluid dynamics (CFD).* Renewable Energy, 2017. **101**: p. 1-9.
39. Lixia Qu, C.N., Lars Davidson, Shia-Hui Peng, Fujun Wang, *Quantitative numerical analysis of flow past a circular cylinder at Reynolds number between 50 and 200.* Journal of Fluids and Structures, 2013. **39**: p. 347-370.
40. K. Lam, Y.F.L., L. Zou, Y. Liu, *Numerical study of flow patterns and force characteristics for square and rectangular cylinders with wavy surfaces.* Journal of Fluids and Structures, 2012. **28**: p. 359-377.

41. *National building code of Canada*. 2015, Associate Committee on the National Building Code, National Research Council.
42. *Antennas, towers, and antennasupporting structures CSA S37-18*. 2018, National Standard of Canada.
43. *Antennas, towers, and antenna supporting structures, CSA S37-13*. 2013: Rexdale, Canada.
44. Canada, N.B.C.o., *User's guide o f NBCC 2015 commentary I*. 2015.
45. Gomes, M., *Wind effects on buildings. Experimental evaluation of pressure coefficients for L-and U-shaped buildings*. 2003, M. Sc. Thesis, Instituto Superior Técnico (IST), Technical University of Lisbon, 2003 (in Portuguese).
46. Gomes, M.G., A. Moret Rodrigues, and P. Mendes, *Experimental and numerical study of wind pressures on irregular-plan shapes.* Journal of Wind Engineering and Industrial Aerodynamics, 2005. **93**(10): p. 741-756.
47. M. Glória Gomes, A.M.R., Pedro Mendes, *Wind effects on and around l- and u-shaped buildings.* 2000.
48. Amin, J. and A. Ahuja, *Experimental study of wind-induced pressures on buildings of various geometries.* International Journal of Engineering, Science and Technology, 2011. **3**(5).
49. Prud'homme, S., et al., *Wind forces on single and shielded angle members in lattice structures.* Journal of Wind Engineering and Industrial Aerodynamics, 2014. **124**: p. 20-28.
50. Novak, M. and A.G. Davenport, *Aeroelastic instability of prisms in turbulent flow.* Journal of the Engineering Mechanics Division, 1970. **96**(1): p. 17-39.
51. Novak, M. and H. Tanaka, *Effect of turbulence on galloping instability.* Journal of the Engineering Mechanics Division, 1974. **100**(1): p. 27-47.
52. Carassale, L., A. Freda, and L. Banfi, *Motion-excited forces acting on a square prism: a qualitative analysis*. 2015.
53. R. M. C So, X.Q.W., W. C. Xie, J. Zhu, *Free-stream turbulence effects on vortex-induced vibration and flow-induced force of an elastic cylinder.* Journal of Fluids and Structures, 2008. **24**(4): p. 481-495.
54. Hemon P., S.F., *On the aeroelastic behaviour of rectangular cylinders in cross-flow.* Journal of Fluids and Structures, 2002. **16**(7): p. 855-889.
55. P. W. Bearman, I.S.G., D. J. Maull, G. V. Parkinson, *Experiments on flow-induced vibration of a square-section cylinder.* Journal of Fluids and Structures, 1987. **1**(1): p. 19-34.
56. Bearman, P.W. and S.C. Luo, *Investigation of the aerodynamic instability of a square-section cylinder by forced oscillation.* Journal of Fluids and Structures, 1988. **2**(2): p. 161-176.
57. Okajima, A. and K. Kitajima, *Numerical study on aeroelastic instability of cylinders with a circular and rectangular cross-section.* Journal of Wind Engineering and Industrial Aerodynamics, 1993. **46-47**: p. 541-550.
58. Haan, F.L. and A. Kareem, *Anatomy of turbulence effects on the aerodynamics of an oscillating prism.* Journal of Engineering Mechanics, 2009. **135**(9): p. 987-999.
59. Sen, S. and S. Mittal, *Effect of mass ratio on free vibrations of a square cylinder at low Reynolds numbers.* Journal of Fluids and Structures, 2015. **54**(Supplement C): p. 661-678.
60. He, T., D. Zhou, and Y. Bao, *Combined interface boundary condition method for fluid–rigid body interaction.* Computer Methods in Applied Mechanics and Engineering, 2012. **223-224**: p. 81-102.

61. Sundaram, P., T.K. Sengupta, and S. Sengupta, *Is Tollmien-Schlichting wave necessary for transition of zero pressure gradient boundary layer flow?* Physics of Fluids, 2019. **31**(3): p. 031701.
62. Sengupta, A., P. Sundaram, and T.K. Sengupta, *Nonmodal nonlinear route of transition to two-dimensional turbulence.* Physical Review Research, 2020. **2**(1): p. 012033.
63. Šarkić, A., et al., *Bridge flutter derivatives based on computed, validated pressure fields.* Journal of Wind Engineering and Industrial Aerodynamics, 2012. **104-106**: p. 141-151.
64. Sarkar, P.P., N.P. Jones, and R.H. Scanlan, *Identification of aeroelastic parameters of flexible bridges.* Journal of Engineering Mechanics, 1994. **120**(8): p. 1718-1742.
65. Nayak, S., *Uncertain quantification of field variables involved in transient convection diffusion problems for imprecisely defined parameters.* International Communications in Heat and Mass Transfer, 2020. **119**: p. 104894.
66. Larsen, A. and J.H. Walther, *Discrete vortex simulation of flow around five generic bridge deck sections.* Journal of Wind Engineering and Industrial Aerodynamics, 1998. **77-78**: p. 591-602.
67. Tamura, K.S.T.I.a.Y., *Prediction of aeroelastic characteristics of rectangular cross-sections by k-w model.* Structures 2004: Building on the Past, Securing the Future, 2004.
68. Scanlan, R., *Motion-related body-force functions in two-dimensional low-speed flow.* Journal of Fluids and Structures, 2000. **14**(1): p. 49-63.
69. Xu, F. and Z. Zhang, *Free vibration numerical simulation technique for extracting flutter derivatives of bridge decks.* Journal of Wind Engineering and Industrial Aerodynamics, 2017. **170**: p. 226-237.
70. Bouris, D. and G. Bergeles, *2D LES of vortex shedding from a square cylinder.* Journal of Wind Engineering and Industrial Aerodynamics, 1999. **80**(1): p. 31-46.
71. Cao, B. and P.P. Sarkar, *Identification of Rational Functions using two-degree-of-freedom model by forced vibration method.* Engineering Structures, 2012. **43**: p. 21-30.
72. M. Matsumoto, T.Y., J. H. Lee, K. Hori, Y. Kawashima, *Karman vortex effect on the aerodynamic forces to rectangular cylinders*. Vol. 9. 2006.
73. Matsumoto, M., Y. Kobayashi, and H. Shirato, *The influence of aerodynamic derivatives on flutter.* Journal of Wind Engineering and Industrial Aerodynamics, 1996. **60**: p. 227-239.
74. Brar, P.S., R. Raul, and R.H. Scanlan, *Numerical calculation of flutter derivatives via indicial functions.* Journal of Fluids and Structures, 1996. **10**(4): p. 337-351.
75. Matsumoto, M., *Aerodynamic damping of prisms.* Journal of Wind Engineering and Industrial Aerodynamics, 1996. **59**(2): p. 159-175.
76. Mannini, C., *Applicability of URANS and DES simulations of flow past rectangular cylinders and bridge sections.* Computation, 2015. **3**(3): p. 479.
77. Nayak, S. and S. Chakraverty, *Non-probabilistic approach to investigate uncertain conjugate heat transfer in an imprecisely defined plate.* International Journal of Heat and Mass Transfer, 2013. **67**: p. 445-454.
78. Yagi, T., et al., *Interferences of vortex sheddings in galloping instability of rectangular cylinders.* Kozo Kogaku Ronbunshu. A (Journal of Structural Engineering. A), 2013. **59A**: p. 552-561.
79. Liu, Y.Z., et al., *A new modeling approach for forced transversely oscillating square-section cylinders.* Journal of Fluids and Structures, 2018. **81**: p. 492-513.
80. Sarwar, M.W., et al., *Prediction of aerodynamic characteristics of a box girder bridge section using the LES turbulence model.* Journal of Wind Engineering and Industrial Aerodynamics, 2008. **96**(10): p. 1895-1911.

81. Jörg Franke, A.H., HA Schlunzen, Bertrand Carissimo. *The Best Practise Guideline for the CFD simulation of flows in the urban environment: an outcome of COST 732*. in *The Fifth International Symposium on Computational Wind Engineering. Chapel Hill, North Carolina, USA*. 2010.
82. Fluent, A., *15.0 Documentation.* Ansys Inc, 2009.
83. Meneveau, C., T.S. Lund, and W.H. Cabot, *A lagrangian dynamic subgrid-scale model of turbulence.* Journal of fluid mechanics, 1996. **319**: p. 353-385.
84. Ricci, M., L. Patruno, and S. de Miranda, *Wind loads and structural response: Benchmarking LES on a low-rise building.* Engineering Structures, 2017. **144**: p. 26-42.
85. Kawai, S. and J. Larsson, *Wall-modeling in large eddy simulation: Length scales, grid resolution, and accuracy.* Physics of Fluids, 2012. **24**(1): p. 015105.
86. Courant, R., *On the partial difference equations of mathematical physics.* Mathematische Annalen, 1928. **100**: p. 32-74.
87. Courant, R., K. Friedrichs, and H. Lewy, *On the partial difference equations of mathematical physics.* IBM journal of Research and Development, 1967. **11**(2): p. 215-234.
88. M. Minguez, C.B., R. Pasquetti, E. Serre, *Experimental and high-order LES analysis of the flow in near-wall region of a square cylinder.* International Journal of Heat and Fluid Flow, 2011. **32**(3): p. 558-566.
89. Carassale, L., A. Freda, and M. Marrè-Brunenghi, *Effects of free-stream turbulence and corner shape on the galloping instability of square cylinders.* Journal of Wind Engineering and Industrial Aerodynamics, 2013. **123**: p. 274-280.
90. Sarioglu, M., Y.E. Akansu, and T. Yavuz, *Control of the flow around square cylinders at incidence by using a rod.* AIAA journal, 2005. **43**(7): p. 1419-1426.
91. Huang, R.F. and B.H. Lin, *Effects of flow patterns on aerodynamic forces of a square cylinder at incidence.* Journal of Mechanics, 2011. **27**(3): p. 347-355.
92. Trias, F.X., A. Gorobets, and A. Oliva, *Turbulent flow around a square cylinder at Reynolds number 22,000: A DNS study.* Computers & Fluids, 2015. **123**: p. 87-98.
93. Chopra, A.K., *Dynamics of structures: Theory and applications to earthquake engineering 4th edition*. 2012, University of California at Berkeley.
94. Soltys, R., M. Tomko, and S. Kmet, *Analysis of wind-induced vibrations of an anchor cable using a simplified fluid–structure interaction method.* Applied Mathematics and Computation, 2015. **267**: p. 223-236.
95. Wang, X.S., *Fundamentals of fluid-solid interactions: analytical and computational approaches*. Vol. 8. 2008: Elsevier.
96. Donea, J., et al., *Arbitrary Lagrangian-Eulerian Methods, volume 1 of Encyclopedia of Computational Mechanics, chapter 14.* John Wiley & Sons Ltd, 2004. **3**: p. 1-25.
97. Blom, F.J., *Considerations on the spring analogy.* International journal for numerical methods in fluids, 2000. **32**(6): p. 647-668.
98. Bartoli, G., et al., *Toward an improvement in the identification of bridge deck flutter derivatives.* Journal of Engineering Mechanics, 2009. **135**(8): p. 771-785.
99. Mara, T.G. and J.P.C. King, *A study of wind effects for the Manning Crevice bridge, Idaho county, Id, section model study*, in *The Boundary Layer Wind Tunnel Laboratory*. 2015, The University of Western Ontario, Faculty of Engineering: London, Ontario, Canada.
100. Kong, L., H. Aboshosha, and J.P.C. King, *A study of wind effects for the Maitland pedestrian bridge over i-4, Orlando, Florida, section model study*, in *The Boundary Layer Wind Tunnel Laboratory*. 2016, The University of Western Ontario, Faculty of Engineering: London, Ontario, Canada.

101. Aboshosha, H., L. Kong, and J.P.C. King, *A study of wind effects for the Pensacola Bay bridge replacement, sup tied arch bridge, Pensacola/gulf breeze, Florida, section model study*, in *The Boundary Layer Wind Tunnel Laboratory*, A.G.D.W.E. Group, Editor. 2017, The University of Western Ontario, Faculty of Engineering: London, Ontario, Canada.
102. Hemon, P., *Large galloping oscillations of a square section cylinder in wind tunnel.* Flow-Induced Vibrations, FIV2012, Dublin, Ireland, July, 2012: p. 3-6.
103. Amandolese, X. and P. Hémon, *Vortex induced vibration of a square cylinder in wind tunnel.* Comptes Rendus Mécanique, 2010. **338**(1): p. 12-17.
104. Nayak, S. and S. Chakraverty, *Interval finite element method with MATLAB*. 2018: Academic Press.
105. Shehryar, M., *Transient instability mechanisms by frequency coalescence in fluid structure systems*. 2010, École Polytechnique.
106. Marra, A.M., C. Mannini, and G. Bartoli, *Measurements and improved model of vortex-induced vibration for an elongated rectangular cylinder.* Journal of Wind Engineering and Industrial Aerodynamics, 2015. **147**(Supplement C): p. 358-367.
107. Ghazal, T., et al., *Flow-conditioning of a subsonic wind tunnel to model boundary layer flows.* Wind and Structures, 2020. **30**(4): p. 339-366.
108. Král, R., S. Pospíšil, and J. Náprstek, *Wind tunnel experiments on unstable self-excited vibration of sectional girders.* Journal of Fluids and Structures, 2014. **44**: p. 235-250.
109. Partha P. Sarkar, L.C., Frederick L. Haan, Hiroshi Sato, Jun Murakoshi, *Comparative and sensitivity study of flutter derivatives of selected bridge deck sections, Part 1: Analysis of inter-laboratory experimental data.* Engineering Structures, 2009. **31**(1): p. 158-169.
110. Bartoli, G. and M. Righi, *Flutter mechanism for rectangular prisms in smooth and turbulent flow.* Journal of Wind Engineering and Industrial Aerodynamics, 2006. **94**(5): p. 275-291.
111. Ermshaus, R., E. Naudascher, and E. Obasaju, *Vortex-induced streamwise oscillation of prisms in a uniform stream of different incidence*, in *Bericht des Sonderforschungsbereichs 210*. 1986, Universität Karlsruhe Karlsruhe, Germany.
112. Sourav, K. and S. Sen, *Transition of VIV-only motion of a square cylinder to combined VIV and galloping at low Reynolds numbers.* Ocean Engineering, 2019. **187**: p. 106208.
113. Parkinson, G., *Phenomena and modelling of flow-induced vibrations of bluff bodies.* Progress in Aerospace Sciences, 1989. **26**(2): p. 169-224.
114. Davenport, A.G., *The treatment of wind loading on tall buildings*, in *Tall Buildings*, A. Coull and B.S. Smith, Editors. 1967, Pergamon. p. 3-45.
115. Nakayama, A., D. Okamoto, and H. Takeda, *Large-eddy simulation of flows past complex truss structures.* Journal of Wind Engineering and Industrial Aerodynamics, 2010. **98**(3): p. 133-144.
116. Juretić, F. and H. Kozmar, *Computational modeling of the neutrally stratified atmospheric boundary layer flow using the standard k–ε turbulence model.* Journal of Wind Engineering and Industrial Aerodynamics, 2013. **115**: p. 112-120.

APPENDIX A. WIND FORCE CALCULATION ON EXPOSED STRUCTURE USER'S GUIDE NBCC 2015 COMMENTARY

The total wind force acting on the exposed structure is decomposed into two Cartesian components as follows:

Normal force $$F_n = KC_{n\infty}qC_gC_eA$$

Tangential force $$F_t = KC_{t\infty}qC_gC_eA$$

$$q = 0.00064645V^2$$

Where,

K: is the reduction factor for members of finite slenderness. Depends on L/h and determined from Table A-1

$C_{n\infty}$ and $C_{t\infty}$: are force coefficients for an infinitely long member, determined from Table A-1.

q: velocity pressure in KPa, determined from equation 1-3, derived using an air density of 1.2929 kg/m^3 corresponding to 0 °C.

V: is the velocity of gust wind in m/sec at 30 (10m) feet above ground (the reference height) and is determined from a wind map in the NBCC.

Cg: the gust factor taken as 2.5 for small structural components (i.e. pole structures).

Ce: the exposure factor shall be taken as $(\frac{H}{10})^{0.2}$ where, 0.9 ≤ Ce ≤ 2.0 for open terrain, and $0.7(\frac{H}{12})^{0.3}$ where, 0.7 ≤ Ce ≤ 2.0 for rough terrain. Where, H is the height above the ground (taken at mid height of studied member).

A: is the cross-sectional area of the surface exposed to wind, given by the product h x l where, l is the length of the member and h is the height of the cross section.

l = Length of member

$A = h \cdot l$ = Area

For wind normal to axis of member: Normal force $F_n = k \cdot C_{n\infty} \cdot q \cdot C_g \cdot C_e \cdot A$

Tangential force $F_t = k \cdot C_{t\infty} \cdot q \cdot C_g \cdot C_e \cdot A$

$C_{n\infty}$ and $C_{t\infty}$: Force coefficients for an infinitely long member

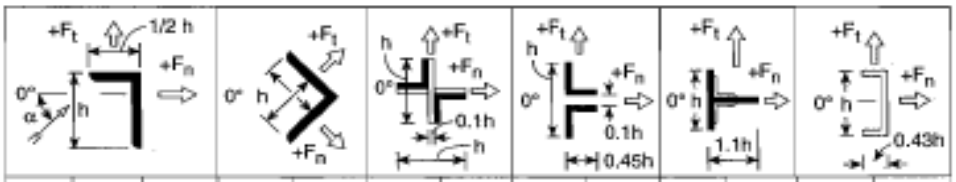

α	$C_{f\infty}$	$C_{t\infty}$	$C_{n\infty}$	$C_{t\infty}$	$C_{f\infty}$	$C_{t\infty}$	$C_{n\infty}$	$C_{t\infty}$	$C_{f\infty}$	$C_{t\infty}$	$C_{f\infty}$	$C_{t\infty}$
0°	+1.9	+0.95	+1.8	+1.8	+1.75	+0.1	+1.6	0	+2.0	0	+2.05	0
45°	+1.8	+0.8	+2.1	+1.8	+0.85	+0.85	+1.5	−0.1	+1.2	+0.9	+1.85	+0.6
90°	+2.0	+1.7	−1.9	−1.0	−0.1	+1.75	−0.95	+0.7	−1.6	+2.15	0	+0.6
135°	−1.8	−0.1	−2.0	+0.3	−0.75	+0.75	−0.5	+1.05	−1.1	+2.4	−1.6	+0.4
180°	−2.0	+0.1	−1.4	−1.4	−1.75	−0.1	−1.5	0	−1.7	±2.1	−1.8	0

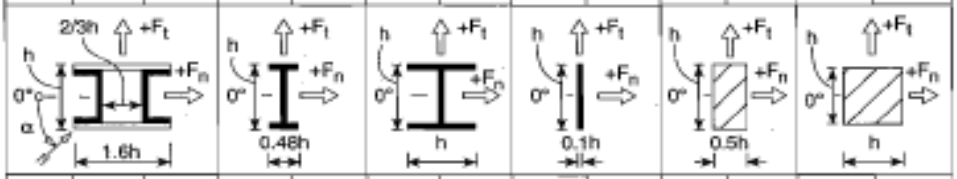

α	$C_{n\infty}$	$C_{t\infty}$	$C_{n\infty}$	$C_{t\infty}$	$C_{n\infty}$	$C_{t\infty}$	$C_{n\infty}$	$C_{t\infty}$	$C_{n\infty}$	$C_{t\infty}$	$C_{n\infty}$	$C_{t\infty}$
0°	+1.4	0	+2.05	0	+1.6	0	+2.0	0	+2.1	0	+2.0	0
45°	+1.2	+1.6	+1.95	+0.6	+1.5	+1.5	+1.8	+0.1	+1.4	+0.7	+1.55	+1.55
90°	0	+2.2	±0.5	+0.9	0	+1.9	0	+0.1	0	+0.75	0	+2.0

For slenderness, h_α is to be used:

k : Reduction factor for members of finite slenderness (in general use full length not panel length)

l/h_α	5	10	20	35	50	100	∞
k	0.60	0.65	0.75	0.85	0.90	0.95	1.0

Table A-1 Structural members, single and assembled sections from NBCC 2015

A_s = Section area

$A = h_t \cdot L$

A_s / A = Solidity ratio

For wind normal to surface A: Normal force $F_n = k \cdot C_{n\infty} \cdot q \cdot C_g \cdot C_e \cdot A_s$

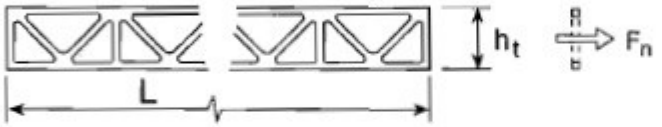

$C_{n\infty}$: Force coeff. for an infinitely long truss, $0 \leq A_s/A \leq 1$

A_s/A	0	0.1	0.15	0.2	0.3 to 0.8	0.95	1.0
$C_{n\infty}$	2.0	1.9	1.8	1.7	1.6	1.8	2.0

k : Reduction factor for trusses of finite length and slenderness

L/h_t \ A_s/A	0.25	0.5	0.9	0.95	1.0
5	0.96	0.91	0.87	0.77	0.60
20	0.98	0.97	0.94	0.89	0.75
50	0.99	0.98	0.97	0.95	0.90
∞	1.0	1.0	1.0	1.0	1.0

EG00938B

Table A-2 Plane trusses made from sharp edged sections

APPENDIX B

Example of the fit for the FSI simulations.

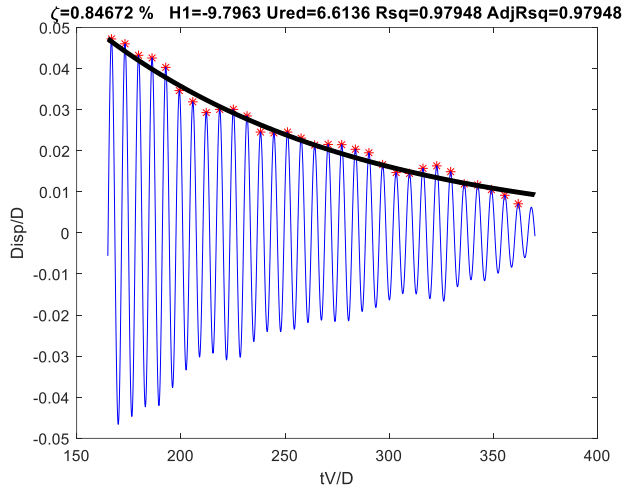

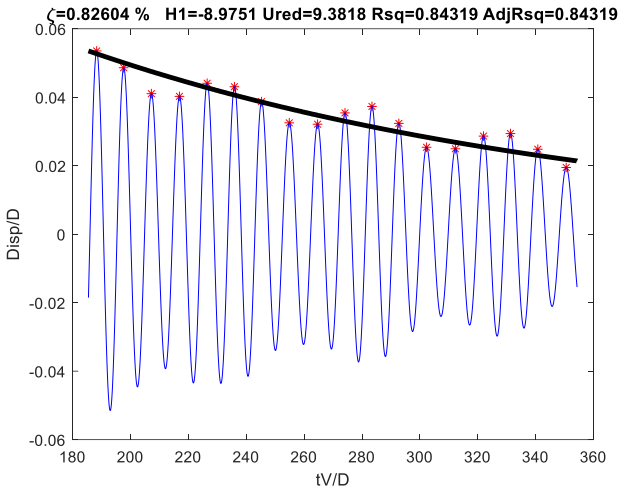

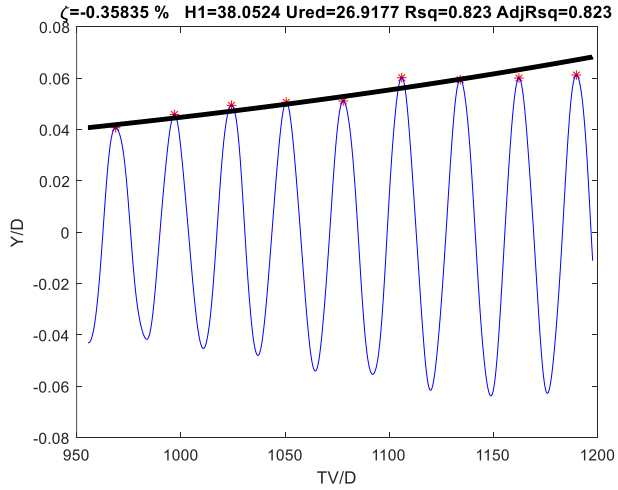

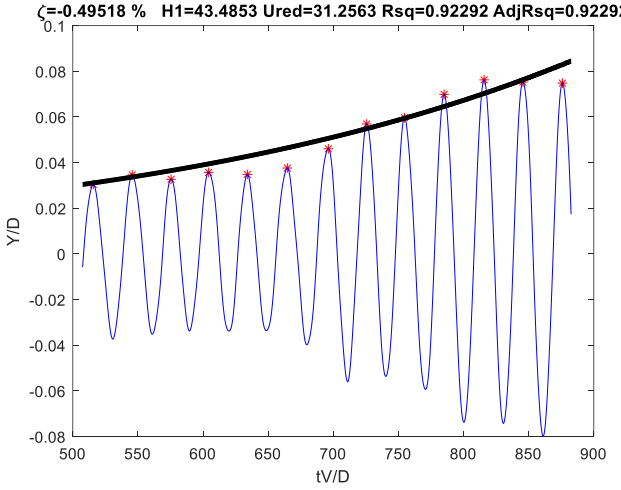

APPENDIX C

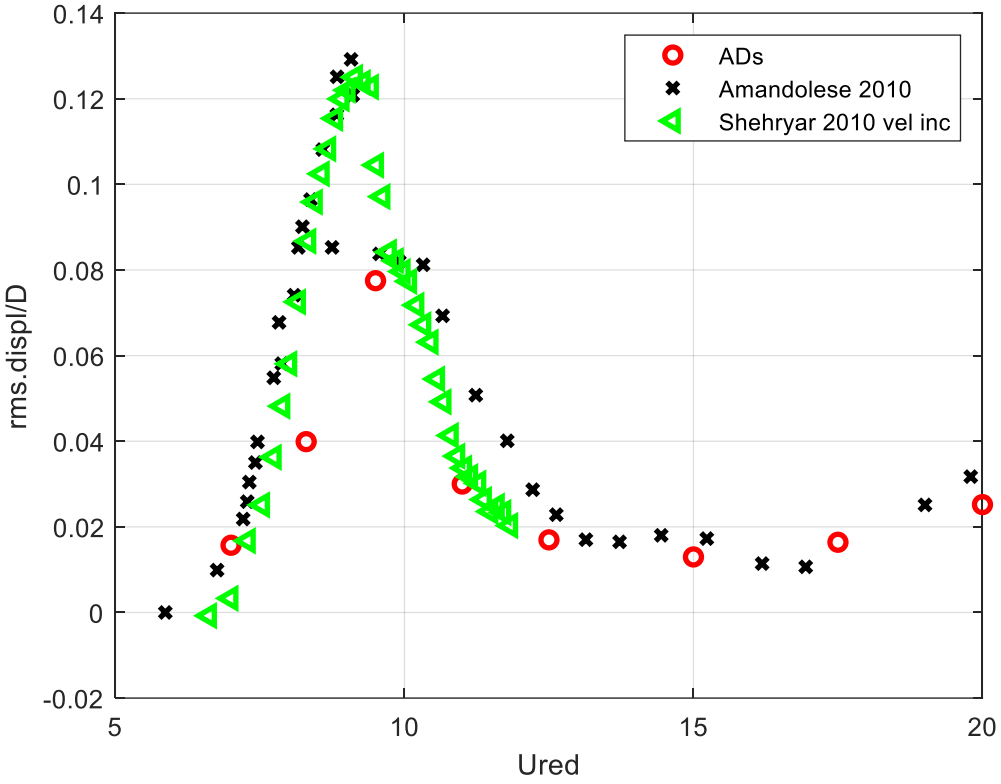
ADs
Amandolese 2010
Shehryar 2010 vel inc
rms.displ/D
Ured
0.14
0.12
0.1
0.08
0.06
0.04
0.02
0
-0.02
5
10
15
20

APPENDIX D

The aerodynamic stiffness, H4, was either not considered in the literature on determining H1 derivative [78,99-101] or proved to play a minor role when considering FSI [14; as similar results were deducted when considering only H1].

Additionally, the aerodynamic stiffness H4 was ignored since there was no use for it in the following work in the thesis. Equation 3-21 was not used in the force calculations in chapter five of this thesis and only the aerodynamic damping was used along with the structural damping in the dynamic analysis of the structure under investigation. References for the equation used to calculate the aerodynamic derivative (equation 3-23) are [98-101]